Department of Physics and Astronomy
Heidelberg University

Bachelor Thesis in Physics
submitted by

Laura Bees

born in Aalen (Germany)

2024

Feasibility study of a double arm spectrometer for the energy loss measurement of charged particles

corrected version

This Bachelor Thesis has been carried out by Laura Bees at the
Physikalisches Institute in Heidelberg
under the supervision of
Prof. André Schöning

Abstract

Precise energy measurements of tracking detectors rely on exact knowledge of the lost energy in the detector material. The aim of the double arm spectrometer is to precisely measure the energy loss of low energy electrons in silicon sensors. Thereby, the sensors can be calibrated with the use of the spectrometer and the resolution of other energy loss measurements can be determined. This work is a feasibility study of such a double arm spectrometer. Different designs are introduced that use position and direction measurements of the electrons to determine their deflection in strong magnetic fields and thus their momentum. Simulations using Geant4 are performed to evaluate the achievable precision and efficiency. The implementation includes the model of an ideal magnetic field approximated to be homogeneous, as well as two variants using more realistic magnetic fields. One assumes parallel cuboid magnets, whereas the other one allows for a wedge angle between the magnet surfaces. A study of uncertainties from multiple scattering and the spatial resolution of the pixel sensors is carried out with the goal to minimize them by modifying the geometry of the experimental setup. While further investigations are needed, preliminary evaluations show a momentum resolution of 14.3 keV/c and 10.4 keV/c depending on the spectrometer configuration, which matches the targeted relative momentum resolution in the order of $\sim O(2 \times 10^{-4})$ for 53 MeV electrons.

Zusammenfassung

Präzise Energiemessungen von Tracking-Detektoren basieren darauf, dass der exakte Energieverlust im Detektormaterial bekannt ist. Das Ziel des “Double Arm Spectrometers” ist die präzise Messung des Energieverlusts von energiearmen Elektronen in Silizium-Pixelsensoren. Eine derartige Energieverlustmessung kann für die Kalibrierung der Sensoren, sowie für die Bestimmung der Auflösung anderer Energieverlustmessungen, angewandt werden. Diese Arbeit untersucht die Realisierbarkeit eines solchen “Double Arm Spectrometers” Spektrometers. Verschiedene Versuchsaufbauten werden vorgestellt, die aus Positions- und Richtungsmessungen der Elektronen die Ablenkung in starken Magnetfeldern und somit deren Impuls bestimmen. Simulationen mit Geant4 werden durchgeführt, um die erreichbare Präzision und Effizienz zu untersuchen. Die Implementierung beinhaltet idealisiertes Modell eines homogonen Magnetfeldes sowie zwei Varianten realistischerer Magnetfelder. Die erste Variante nimmt paralle, quaderförmige Magnete an, während die zweite Variante einen Keilwinkel zwischen den Oberflächen der Magnete erlaubt. Eine Untersuchung der Messunsicherheiten durch Mehrfachstreuung, sowie durch die räumliche Auflösung der Pixelsensoren wird durch Anpassungen der Anordnung von Komponenten im experimentellen Aufbau durchgeführt. Wenn auch weitere Untersuchungen benötigt werden, ergibt eine vorläufige Auswertung eine Impulsauflösung von 14.3 keV/c und 10.4 keV/c abhängig von der Spektrometer-Konfiguration, welche die gezielte relative Impulsauflösung in der Größenordnung $\sim O(2 \times 10^{-4})$ für Elektronen der Energie 53 MeV erreicht.

Contents

Chapter 1

Introduction

In particle physics, the Standard Model is a very well established theory describing the elementary particles and fundamental forces of the universe [11]. A large range of phenomena is predicted by this model. In order to verify that the physical behavior is correctly explained by it and to evaluate its accuracy, observations with experiments that determine the predicted quantities with high precision are needed. Additionally, experiments are designed to examine possible deficiencies of the model. Such experiments have already found certain inconsistencies like neutrino oscillations, dark matter and dark energy and the matter-antimatter asymmetry.

The MEG experiment located at the Paul Scherrer Institute searches for the muon decay $\mu^+ \to e^+ + \gamma$ [10, 5]. Due to the violation of charged lepton flavour conservation, this process is heavily suppressed in the Standard Model with a branching ratio smaller than 10^{-53}. Thus, the detection of this process would indicate new physics beyond the Standard Model. The improvement of sensitivity to the process relies on precise energy resolution of the produced particles. An investigation of the MEG II calorimeter with quasi-monochromatic 55 MeV γ-rays shows a relative energy resolution of $1.8 - 2.0\%$ [9]. Another option to be considered, is to determine the photon energy through track reconstruction of the converted electron-positron pair $\gamma \to e^+ + e^-$ [2]. The limiting factor for the resolution of the thereby obtained photon energy is not the measurement precision of the converted pair's energy, but rather the precision of the pair's energy loss within the detector.

This motivates the investigation of a new spectrometer design for energy loss measurements of charged particles in silicon sensors, which is done in the course of this thesis. A so-called double arm spectrometer can be used for different types of charged particles and devices under test. It is intended to be a tool for the characterization of tracking detectors, which can be applied for the calibration of energy loss in the detectors and the determination of the resolution in energy loss measurements. For the feasibility evaluation of a high precision energy measurement with the presented design, simulations are performed for the energy loss of 53 MeV electrons in a silicon layer with the dimensions of the MuPix-sensor [4]. Aiming at a relative momentum resolution of $\sim O(2 \times 10^{-4})$, setup modifications for an optimal measurement are considered.

Chapter 2

Theory

2.1 Charged Particles in a Homogeneous Magnetic Field

Charged particles experience a force when moving through a magnetic field $\vec{B}$. This force, called the Lorentz force, is perpendicular to both the magnetic field and the particle's motion. Thus, the direction of the particle changes, while its absolute momentum is conserved. For a particle with charge q, mass m and momentum $\vec{p}$, the Lorentz force is given as:

$$\vec{F_L} = \frac{q}{m}\left(\vec{p} \times \vec{B}\right) \tag{2.1}$$

In a homogeneous field, this results in a helical motion with radius R (or a circular motion, if $\vec{p} \perp \vec{B}$). Let $p_\perp$ be the component of $\vec{p}$ that is perpendicular to $\vec{B}$. Then, the centripetal force describes this as:

$$F_C = \frac{p_\perp^2}{mR} \tag{2.2}$$

This implies $p_\perp$ is proportional to the product of R and the field strength B. For an electron, the following relation holds:

$$p_\perp \left[\frac{\mathrm{GeV}}{\mathrm{c}}\right] = b \cdot B[\mathrm{T}] \cdot R[\mathrm{m}] \tag{2.3}$$

with the constant $b = 0.299792458$ of proportionality.

2.2 Energy Loss of Electrons in Matter

A comprehensive view of various kinds of particles interacting with matter in different processes is given in [12]. This paper was used to gather an overview of the effects relevant for this work in the following two sections.

The energy measurement of an electron with tracking detectors is influenced by the energy loss during the measurement. This energy loss is a result of the electron's interaction with the detector material via the electromagnetic force which causes the particle to experience a retarding force. For different energy ranges and materials, the dominant interaction type varies and with it the mean rate of energy transferred from the particle to the detector material.

At very low energies electrons primarily lose energy by ionization, although other processes (Møller scattering, Bhabha scattering, e+ annihilation) contribute, as shown in fig. 2.1.

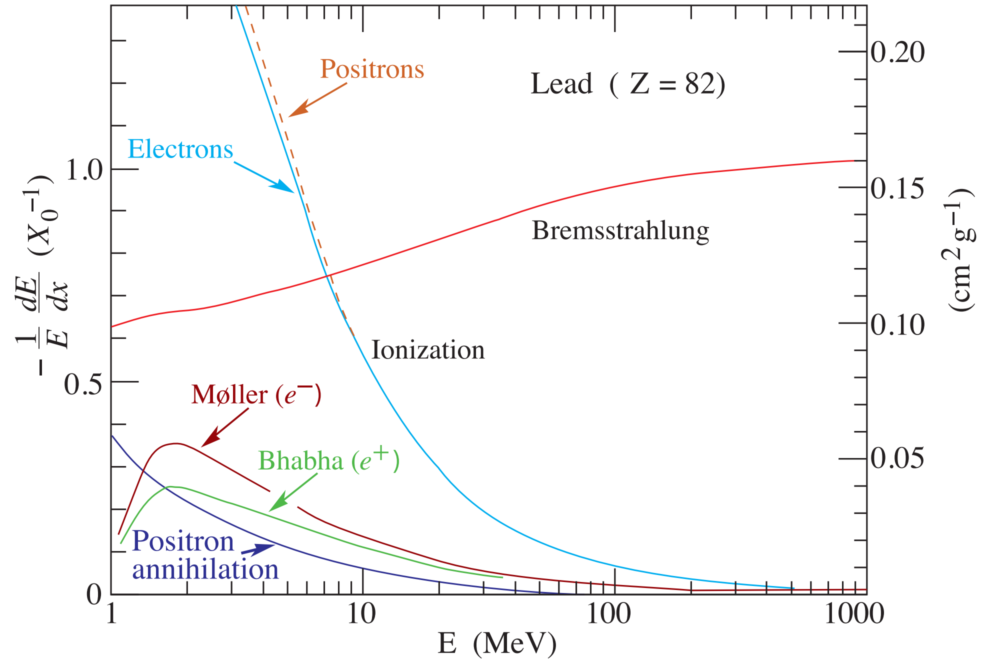

Figure 2.1: Fractional energy loss per radiation length in lead as a function of electron/positron energy [12].

Above a certain energy, the energy loss is then dominated by Bremsstrahlung. The energy loss through Bremsstrahlung increases nearly linearly with the particle's energy causing it to surpass the ionization effect, which has a logarithmic dependency, rapidly. The low mass of the electron causes it to be deflected strongly in interactions, which leads to a big kinematic energy transfer limit. The critical energy E_c of a material describes the value at which the ionization and Bremsstrahlung both have the same impact on the energy loss. It can roughly be estimated with the nuclear charge number Z by the following empirical relation.

$$E_c \approx \frac{800\,\mathrm{MeV}}{Z + 1.2} \tag{2.4}$$

2.2.1 Ionization

The mass collision stopping power describes the average energy loss per unit pathlength due to inelastic Coulomb scattering resulting in the ionization and excitation of atoms or molecules. It is derived by Berger and Seltzer [19] from Bethe's stopping-power theory as

$$\left\langle \frac{dE}{dx} \right\rangle = \rho \frac{0.153536}{\beta^2} \frac{Z}{A} B(T), \tag{2.5}$$

where T is the kinetic energy of the electron, β is its velocity in units of the velocity of light c, A is the atomic weight and ρ is the density of the medium. The stopping number $B(T)$ varies for different mediums only because of the different mean excitation energies I and different density-effect corrections δ.

$$B(T) = B_0(T) - 2 \ln \left(\frac{I}{m_e c^2} - \delta \right) \tag{2.6}$$

Here, m_e is the mass of the electron.

2.2.2 Bremsstrahlung

Figure 2.2 shows Feynman diagrams of an electron being deflected in the electric field of a nucleus. As a result of the electron coupling to the nucleus, a photon is emitted.

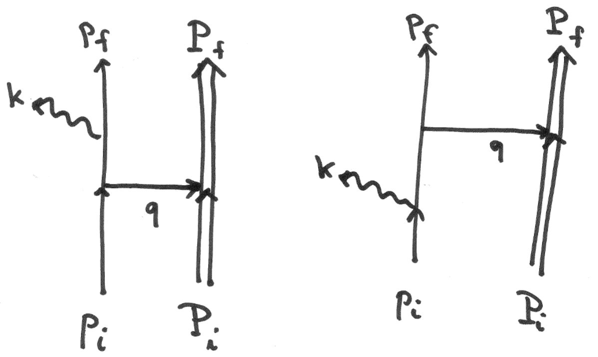

Figure 2.2: Lowest-order Feynman diagrams for electron bremsstrahlung. The nucleus is shown by a double line [14].

The energy loss by bremsstrahlung is proportional to the fraction $\frac{1}{m_e^2}$ making it especially relevant for electrons due to their low mass. As the energy loss is nearly proportional to the electron's energy the following approximation can be made for the stopping power of relativistic particles:

$$\left\langle \frac{dE}{dx} \right\rangle \approx -\frac{\rho}{X_0} E \tag{2.7}$$

The proportionality constant X_0 is the radiation length. It is characteristic for each material and defines the mean distance, after which the electron's energy is reduced to $\frac{1}{e}$ of its initial energy. It can be calculated with

$$X_0 = \frac{716.405\,\mathrm{cm}^2\mathrm{g}^{-1} A}{Z^2\left(L_{rad} - f(Z)\right) + Z L'_{rad}}, \tag{2.8}$$

where the function $f(Z)$ is determined up to the fourth order by

$$f(Z) = (\alpha Z)^2 \left((1 + (\alpha Z)^2)^{-1} + 0.20206 - 0.0369(\alpha Z)^2 + 0.0083(\alpha Z)^3 - 0.002(\alpha Z)^6 \right), \tag{2.9}$$

and the parameters L_{rad} and L'_{rad} are tabulated in [20]. Here, α is a denotation of the fine-structure constant.

For a compound of i elements with the radiation length X_i and their fraction by weight w_i, the resulting radiation length can be approximated by:

$$\frac{1}{X_0} = \sum_i \frac{w_i}{X_i}. \tag{2.10}$$

With the approximation of eq. (2.7), the energy of an electron with initial energy E_{ini} can be described as an exponential function of the covered distance x in the material.

$$E(x) = E_{ini} \cdot e^{-x\rho/X_0} \tag{2.11}$$

2.2.3 Synchrotron Radiation

When traveling in a circular orbit of radius R, a particle with charge e and energy $E = \gamma m c^2$ causes a classical energy loss δE per revolution, which is given as

$$\delta E = \frac{4\pi}{3}\frac{e^2}{R}\beta^3\gamma^4. \tag{2.12}$$

2.3 Multiple Scattering

When traversing through matter, charged particles suffer many successive collisions leading to small-angle scattering [18]. The biggest contribution results from Rutherford scattering and is distributed as a Gaussian. Additional to this Coulomb scattering from atomic nuclei following the Moliére theory [6], a smaller number of hard scatters due to strong interactions cause tails in the resulting angular distribution. The adapted Highland formula by Lynch and Dahl describes the characteristic root mean square (rms) width θ_{rms} of the angular distribution in a plane shown in fig. 2.3 as

$$\theta_{rms} = \frac{13.6\,\mathrm{MeV}}{\beta c p} z \sqrt{\frac{x}{X_0}} \left(1 + 0.038 \ln\left(\frac{x z^2}{X_0 \beta^2}\right)\right), \tag{2.13}$$

where z and p are the charge number and initial momentum of the particle and x and X_0 have to be determined for the entire composition of layers traversed by the particle [16].

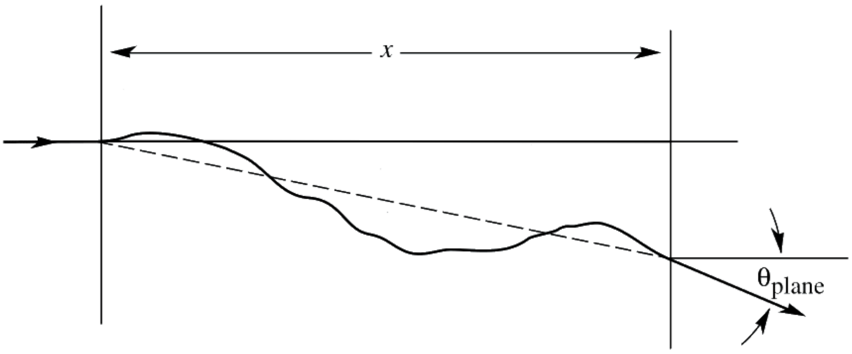

Figure 2.3: Characteristic rms width θ_{rms} of the Coulomb multiple scattering angular distribution.

2.4 Electron Optics with Magnetic Fields

A detailed description of this topic can be found in [13]. This chapter is based on the explanations given there and presents the results, which are essential for this topic.

2.4.1 Geometric Optics

In optics an image point is the position where light rays, propagating from a common origin, converge again after passing through an optical system. Geometric optics use geometric relations to construct the rays' path. In a parallel manner, the deflection of particles in magnetic fields can be described. More specifically, the matrix methods for optical lenses following from the geometric relations can be transferred to ion optics. An element in an ion-optical system can be described in linear approximation by a transfer matrix R, the system itself is then given by the multiplication of the component's matrices.

At the surface of a lens, incoming light rays are refracted and either focused (convex lens) or dispersed (concave lens). In the case of an ideal spherical thin lens, the rays' change of direction $\Delta x'$ is proportional to the spacial deviation x_0:

$$\begin{pmatrix} x \\ x' \end{pmatrix} = R_x \begin{pmatrix} x_0 \\ x_0' \end{pmatrix} = \begin{pmatrix} 1 & 0 \\ -\frac{1}{f} & 1 \end{pmatrix} \begin{pmatrix} x_0 \\ x_0' \end{pmatrix}, \tag{2.14}$$

where f is the focal length and the index 0 is used for the quantities at the initial state.

(a) convex thin lens with $f > 0$ (b) concave thin lens with $f < 0$

Figure 2.4: Schematics of optical lenses [13].

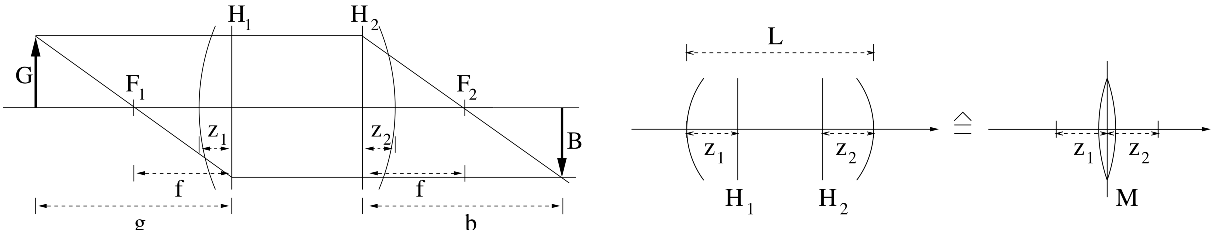

(a) thick lense imaging (b) thick lens represented as a thin lens

Figure 2.5: Geometric optics with a thick lens [13].

For the imaging of a point (G) at distance g from the thin lens to a point (B) at distance b from the lens, the following relation holds:

$$\begin{pmatrix} x \\ x' \end{pmatrix} = \begin{pmatrix} -\frac{b}{g} & 0 \\ -\frac{1}{f} & -\frac{g}{b} \end{pmatrix} \begin{pmatrix} x_0 \\ x_0' \end{pmatrix}, \tag{2.15}$$

For a thick lens, the two planes at distance f from the focal planes are defined as the principal planes H_i, which have certain distances z_i to the starting and ending point of the lens (fig. 2.5). Each focusing or defocusing element can be described as a thin lens, where the principal planes are assumed to coincide at the center of the lens and the term $L - z_1 - z_2$ is added to the length of the thin lens defining an effective length.

2.4.2 Homogeneous Deflection Magnet

The homogeneous deflection magnet produces a homogeneous magnetic field, which is oriented in the perpendicular direction to the targeted deflection plane. It has a focussing effect in radial direction of the particle. For a targeted orbit radius ρ_0, a deflection angle α and an effective length $L = \alpha\rho_0$, the following transfer matrix R can be used to describe the relative coordinates $\mathbf{x}(s)$ of the particle with initial coordinates $\mathbf{x_0}(s)$.

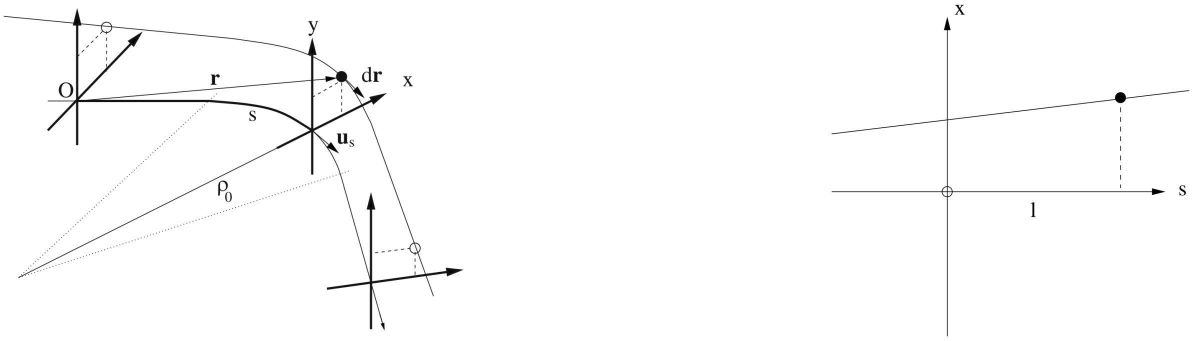

(a) relative coordinates x, x', y, y' (b) stationary coordinates l,δ

Figure 2.6: Coordinate system for $\mathbf{x}(s)$ [13].

$$\mathbf{x}(s) = R \cdot \mathbf{x_0}(s) = \begin{pmatrix} \cos\alpha & \rho_0 \sin\alpha & 0 & 0 & 0 & \rho_0(1-\cos\alpha) \\ -\frac{\sin\alpha}{\rho_0} & \cos\alpha & 0 & 0 & 0 & \sin\alpha \\ 0 & 0 & 1 & \rho_0\alpha & 0 & 0 \\ 0 & 0 & 0 & 1 & 0 & 0 \\ -\sin\alpha & -\rho_0(1-\cos\alpha) & 0 & 0 & 1 & \rho_0\frac{\alpha}{\gamma^2} - \rho_0(\alpha - \sin\alpha) \\ 0 & 0 & 0 & 0 & 0 & 1 \end{pmatrix} \begin{pmatrix} x_0 \\ x'_0 \\ y_0 \\ y'_0 \\ l_0 \\ \delta_0 \end{pmatrix} \tag{2.16}$$

The particle's position and impulse deviations after a covered distance s are given in a coordinate system that is defined by the radial position and direction displacement x and x', the axial position and direction displacement y and y', the longitudinal position displacement l and the relative impulse deviation δ. All deviations are given with respect to the corresponding desired track parameters.

According to this matrix equation the axial position displacement y is given as

$$y = y_0 + \rho_0 \alpha y'_0 = y_0 + L y'_0,$$

which is the same for a particle traversing in no magnetic field over a distance L and means that focusing in the axial direction y is not possible.

2.4.3 Focusing Deflection Magnet

Unlike the homogeneous deflection magnet, the focusing deflection magnet produces an inhomogeneous field with a field index $n \neq 0$, which is defined as

$$n = \frac{\partial B_y}{\partial x} \frac{\rho_0}{B_0}. \tag{2.17}$$

With the "sharp cut-off" approximation, which assumes the magnetic field to rise or drop instantly at the magnet edges, the radial and axial position displacements are given as

$$x = \cos\left(\sqrt{1-n}\alpha\right) x_0 + \frac{\rho_0 \sin\left(\sqrt{1-n}\right)\alpha}{\sqrt{1-n}} x_0' + \frac{\rho_0\left(1-\cos\left(\sqrt{1-n}\alpha\right)\right)}{1-n}\delta_0 \tag{2.18}$$

$$y = \cos\left(\sqrt{n}\alpha\right) y_0 + \frac{\rho_0 \sin\left(\sqrt{n}\alpha\right)}{\sqrt{n}} y_0' \tag{2.19}$$

where the field index is assumed to fulfill the condition $0 < n < 1$. With the additional condition that the field index is chosen such that both of the above equations are equal to 0, focusing in the axial and radial direction can be obtained.

2.4.4 Edge Focusing

This paragraph considers the edge focusing of a homogeneous deflection magnet. Under the condition that the targeted path of the particle outside the magnet has a certain edge angle $\varphi \neq 0$ between the radial direction x of the particle and the magnet edge, the particle experiences a field gradient at the transition point. It focuses in either the radial direction x or the axial direction y and defocuses in the other one depending on the sign of φ. For a certain radial displacement $x_0 \neq 0$, the length of the track inside the magnet varies from the one without a displacement, leading to a changed radial direction displacement x'. A change of the axial direction displacement y' is caused by the non-zero field component B_x of the magnetic field in radial direction outside the magnet. An integration over this field component along a closed curve from a point outside the magnet via a point inside the homogeneous field (as shown in fig. 2.7), allows the calculation of this change $\Delta y'$ of the axial direction displacement, using the symmetry of the field with respect to the median plane and the fact that the integral is zero as a result of $\nabla \times \mathbf{B} = 0$. With an additional correction to an efficient edge angle φ_{eff} due to the finite nature of the boundary field, the effect of the edge focusing can be described by the following equations.

$$\begin{aligned} x' &= x_0' + \frac{\tan\varphi}{\rho_0} x_0 \\ y' &= y_0' - \frac{\tan\varphi_{eff}}{\rho_0} y_0 \end{aligned} \tag{2.20}$$

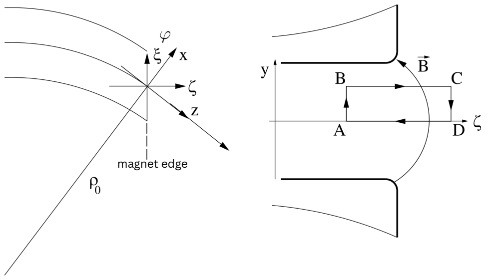

Figure 2.7: Integration path for the calculation of edge focusing [13] (edited).

2.5 Magnetic Stray Fields of Stacked Permanent Magnets

The field strength of a permanent magnet with a magnetization $\vec{M}$ oriented in the y-direction, can be calculated with the Amperian Current Model. When looking at the magnetization as microscopic dipoles that are arranged with a certain density and direction, it becomes apparent that the current, which can be assigned to these dipoles, cancels out inside the magnet. Only the current at the surface of the magnet remains and contributes to the field of the cuboid. As the resulting surface current $\vec{I}$ is perpendicular to the direction of the magnetic field, the two xz-planes of the cuboid's surface also do not contribute and the cuboid corresponds to a rectangular band of the surface current. The field produced by the cuboid can be obtained by an integration over this current.

In an equivalent approach [17], the field strength of the permanent magnet can be calculated with the Coulombian equivalent charge method through an integration of the magnetic surface charge $\sigma = \mu_0 \vec{M} \cdot \vec{n}$ over the magnet's surface area according to

$$\vec{B}(\vec{r}) = \int\int \frac{\sigma(\vec{r} - \vec{r'})}{|\vec{r} - \vec{r'}|^3} ds, \tag{2.21}$$

where $\vec{r}$ is the observation point, $\vec{r'}$ is the distance to the area ds and $\vec{n}$ is the normal vector of the area [15]. The field resulting from multiple cuboids is then obtained from the sum of the fields produced by the individual cuboids at their respective positions.

For two stacked permanent magnet cuboids arranged as shown in fig. 2.8 with a magnetization in the y-direction and a certain residual magnetic flux density B_s, which defines the amount of magnetization retained by the material after removing an external magnetic field, the field strength inside the gap depends on the distance from the center point in the gap as shown in fig. 2.9. Here, the edges of the magnets are assumed to be parallel to each other. The field inside the gap appears to be rather homogeneous. For the purpose of this work, the constancy of the y-component of the magnetic field is especially relevant. This component directly influences the bending in the xz-plane of a particle moving in the produced field. The amount of bending in the xz-plane is used for the momentum determination of the spectrometer which is introduced in section 3.5. In the context of this work, stray fields are therefore defined as deviations of the y-component of the magnetic field from the desired value.

Both of the above approaches for the calculation of the magnets' fields assume ideal magnet cuboids. The thereby given homogeneity cannot exactly be achieved in an experimental setup. Some reasons for this can be the temperature dependence of the magnetization, influences of external magnetic fields or oxidation leading to degradation of the magnet material [15].

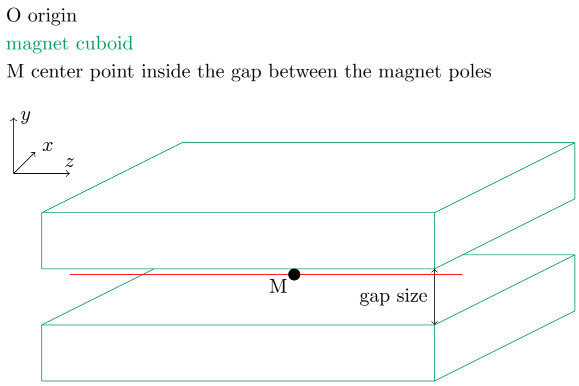

Figure 2.8: Setup of two stacked magnet cuboids with their edges parallel to each other. Point M is the center point inside the gap between the magnet poles. The *red* line depicts the path along which the field profile in fig. 2.9 is shown. The path goes through the center of the gap and is parallel to the magnet edges.

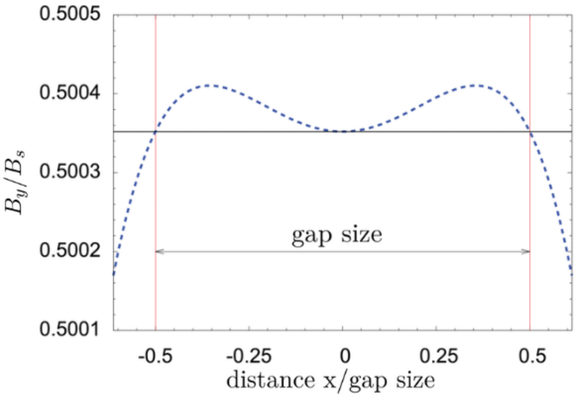

Figure 2.9: Magnetic stray field for two stacked permanent magnet cuboids inside the gap [15] (edited). The profile is taken along the path depicted in fig. 2.8. The parameter x discribes the distance from the center point M inside the gap. The two *red* lines mark the points with the same distance to the center point M and to the closest magnet edge in y-direction. At these points, the magnetic field strength is the same as the magnetic field strength at M.

Chapter 3

A Double Arm Spectrometer

The energy loss measurement is conducted using a double arm spectrometer which is described in this chapter. The device under test (DUT) is placed between the two spectrometer arms. Each arm measures the momentum of the electrons shot through the spectrometer. As the electrons are highly relativistic, the electrons' energy in the individual arms is thereby directly obtained and the energy loss in the DUT can be deduced. This procedure is described in detail in section 3.1. The spectrometer arms require magnetic fields which are crucial for their operation. An ideal magnet model as well as two more realistic magnet models are explained in section 3.2. Different arrangements of the sensors and magnets form multiple spectrometer setups which are depicted in section 3.3. To investigate the feasibility, a Monte Carlo simulation using the Geant4 toolkit is performed. The implementation details are given in section 3.4. To calculate the electron energies in the spectrometer arms, a reconstruction of the tracks is required. Section 3.5 describes how the track reconstruction is conducted and implemented.

3.1 Energy Loss Measurement

While the basic principle of the energy loss measurement is equal in all spectrometer setups, its details are different. This section aims to give a general introduction into the principle based on the Double Edge Focusing Spectrometer. It is designed to measure the energy loss in the position sensitive device under test (DUT) that is placed in between two spectrometer arms; see fig. 3.1. A Monolithic Active Pixel Sensor with a thickness of 600 µm is used as the DUT. In each detector arm, a separate energy measurement is carried out. The energy loss is deduced from the difference between the individual momentum measurements.

A low energy electron is shot with a certain inclination angle α_x from point G into the first detector arm which comprises two thin (50 µm, monolithic) pixel layers for the detection of the electron's position and direction. The initial direction of the electron is in the x,z-plane. The angle α_x specifies the deviation from the z-direction. It is defined as positive (negative) for an

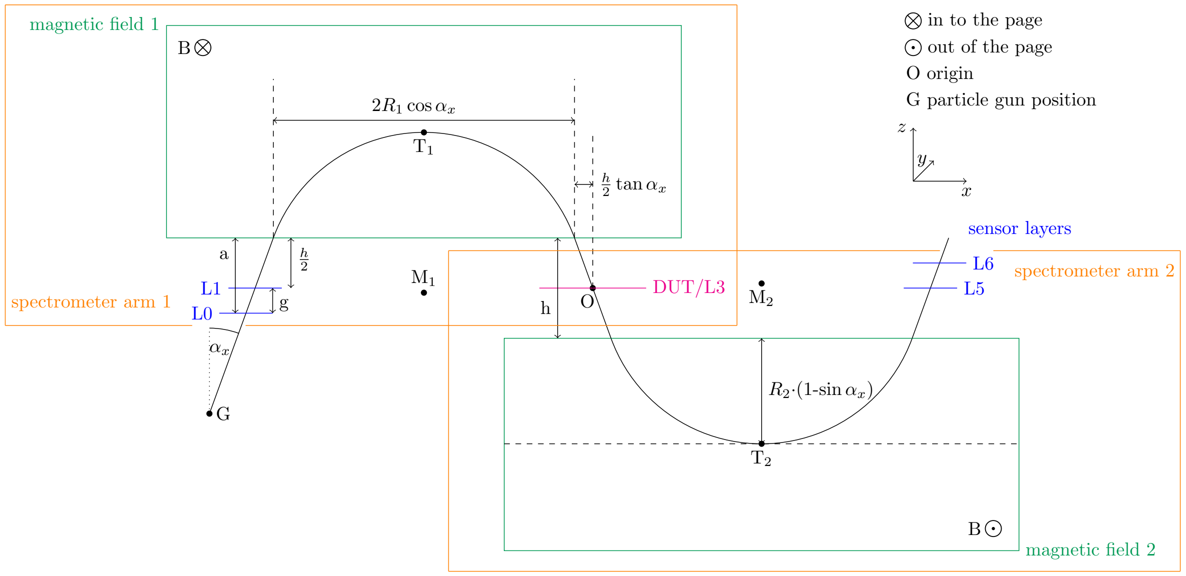

Figure 3.1: A Simple Double Arm Spectrometer with a device under test (DUT). Each spectrometer arm consists of two monolithic sensor layers Li with the distance g to each other and a magnetic field region. The field regions are of opposite polarity and positioned with their edges at distance $h/2$ to the closest sensor layers L1,L5, as well as to the DUT. The origin of the coordinate system is defined as the center position of the DUT. The electron is shot from a certain gun position G under an angle α_x with respect to the z-direction into the first spectrometer arm. After leaving a hit at the sensor layers L0 and L1, the electron enters into the first magnetic field region, which is polarized in the y-direction. Due to the Lorentz force, it is deflected in the xz-plane doing a circular turn with the radius R_1 around the circle center M_1 and leaves the field region again before reaching the position sensitive DUT. Having lost some of its energy in the DUT, the electron enters the other magnetic field region belonging to the second spectrometer arm, where it does a turn with a smaller radius R_2 around M_2 in the other direction of the previous turn. The last two position measurements are made at layers L5 and L6, when the electron is in the field free region again. T_1 and T_2 are defined as the turning points in the magnetic field region, where the electron moves closer to the plane z=0 again.

electron moving in positive (negative) x-direction. After passing through the first two silicon sensors, the electron enters a strong magnetic field, which is constant over time. Due to the deflection caused by the Lorentz force, the electron exits the field region under the same angle α_x again. Under the condition that the field strength is known along the electron's track, a second measurement of the electron's position – either with the DUT or another silicon sensor – allows the reconstruction of its deflection within the magnetic field. Along with that, the electron's transverse momentum within the bending plane is determined using the proportional dependency given by *eq.* (2.3).

The second energy measurement after the DUT is obtained analogously in the other spectrometer arm that is built symmetrically to the first one, but has a magnetic field of opposite polarity.

3.2 Magnet Models

To create the strong magnetic field regions, cuboid permanent magnets are intended to be used. As the particle's momentum is reconstructed based on its deflection in these field regions, the turn which depends on the field strength along the particle's track has to be simulated correctly. A description of the field along the trajectory is therefore necessary to obtain the correct bending of the track. In this thesis, three different models of the magnetic field have been studied and are discussed in the following sections.

3.2.1 Homogeneous Magnetic Field Approximation

For a first feasibility assessment, the field regions are approximated as homogeneous with edges where the field strength drops instantly to zero. This means that the field strength is non-zero and constant in certain defined x-, y- and z-ranges and 0 otherwise. All calculation and simulations with this model are conducted for a field strength of $B_y = 1\,\mathrm{T}$. The orientation of the field in the first spectrometer arm is defined along the $y-$direction. The field in the second arm is of opposite polarity. This sets the bending plane of the particle in both arms to the $xz-$plane. The distance between the two field regions is given as h, their edges are aligned parallelly, i.e. h does not depend on x or y.

In the following, only the deflection caused by the field of this magnet model is considered to describe the electron's movement from one sensor layer to the next. The electron is assumed to only lose energy at the DUT. Effects like multiple scattering and energy loss in the regions between the sensor layers are neglected. Under these conditions, the electron moves in a straight line outside the field regions. Inside the field regions, the projection of its track on the xz-plane can be described as a circular arc with a certain radius R as described in section 2.1. For the reconstruction, this behavior of the electron has the advantage of the possibility to obtain the trajectory by connecting the hits in the different layers with a combination of straight lines in the field free regions and circular arcs in the field regions. A determination of the radii, and therefore also of the momenta, is thus possible with simple geometric relations. Thereby, the calculations are simplified to a large extent and an easy way to get a first assessment on the results is provided.

3.2.2 Inhomogeneous Magnetic Field Configurations

To improve the simple homogeneous magnet model, the model of a magnetic field generated by magnet cuboids is used instead. Additionally, the magnets might be parallel or wedged. The following subsections describe these two configuration separately.

Parallel Magnet Configuration

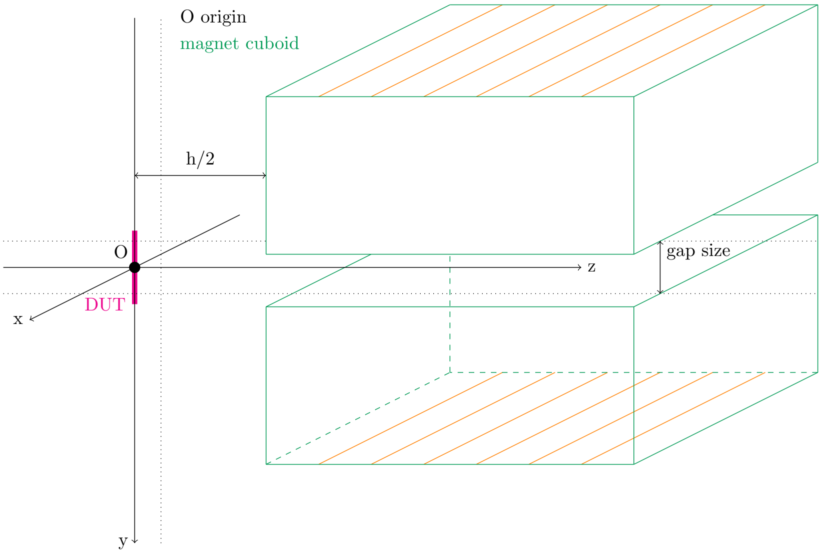

Figure 3.2: Magnets of the first spectrometer arm for the setup of two stacked magnet cuboids with their edges parallel to each other. The electron is shot into the rather homogeneous gap region between the two magnets. The DUT is positioned at the origin of the coordinate system, which implies that the z-axis does not pass through the center point in the magnet gap as can be seen in fig. 3.1. The plane $y = 0$ is chosen such that it has the same distance to both of the magnet poles. The supporting iron construction for the magnets, containing the flux and reducing the stray fields, is connected to the magnet surfaces marked *orange*. This construction is not a part of the model in the simulation. Instead, the iron magnets are chosen extremely long in the y-direction (2×10^7 mm).

In order to obtain realistic energy loss measurements, the inhomogeneity of the field has to be considered. For that, a more realistic model is used in which the magnetic field is described as a sum of the fields produced by the individual magnet cuboids at their respective positions.

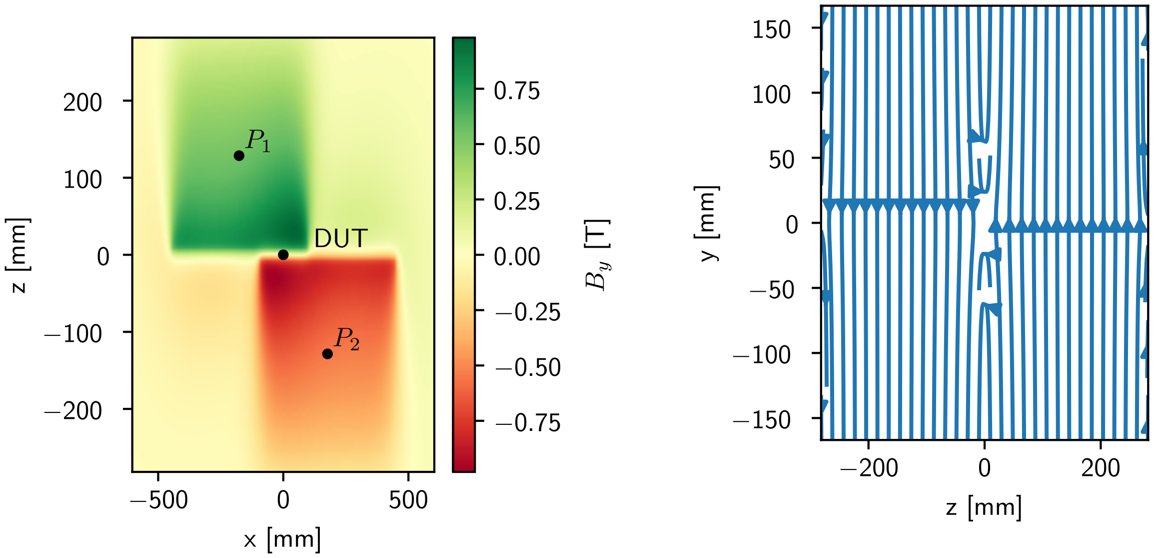

(a) Map of the B_y component in the parallel magnet configuration. The B_y component of the magnetic field is evaluated at different positions in the xz-plane $y = 5\,\mathrm{mm}$, which is inside the gap between the magnets. The *green* region describes the field in the first spectrometer arm (with the center position P_1), the *red* region is equal to the region of the second spectrometer arm (with the center position P_2 of the stacked magnets).

(b) Stream plot of the magnetic field lines in the parallel magnet configuration. The direction of the field lines is shown from the perspective of the zy-plane at the x-position of the DUT. The field in the second spectrometer arm is depicted by the range $z < -5\,\mathrm{mm}$, the range $[-5\,\mathrm{mm}, 5\,\mathrm{mm}]$ depicts the field from the edge of one arm to the other arm and $z > 5\,\mathrm{mm}$ is equivalent to the field in the first arm.

Figure 3.3: Magnetic field of the spectrometer setup for the model of stacked parallel magnet cuboids. The gap between the magnet poles is set to 17 mm. The field map and stream plot use a function that can be obtained according to either one of the methods described in section 2.5, to evaluate the magnetic stray field at different positions in the setup.

For each of the field regions, two of the magnet cuboids are stacked with their edges parallel to each other (see fig. 3.2) in a supporting structure of iron. Thereby, a certain gap between the opposite poles of the two magnets is created. This gap region, which still has a rather homogeneous field as can be seen in the field maps and profiles in fig. 3.3, fig. 3.4, as well as in fig. A.7, fig. A.8 and fig. A.9, is intended to be used to deflect the electron. To obtain the same polarity for the fields in the gaps as in the case of the homogeneous model, each magnet cuboid in the upper spectrometer arm is assumed to have a magnetization in positive y-direction, whereas the cuboids in the lower arm have the opposite magnetization direction. According to the Amperian Current Model, the field of the cuboid only depends on its size in all three dimensions and the magnetization of it. For all simulations and calculations with this model, the magnetization for each magnet cuboid is set to a value that corresponds to a magnetic field of

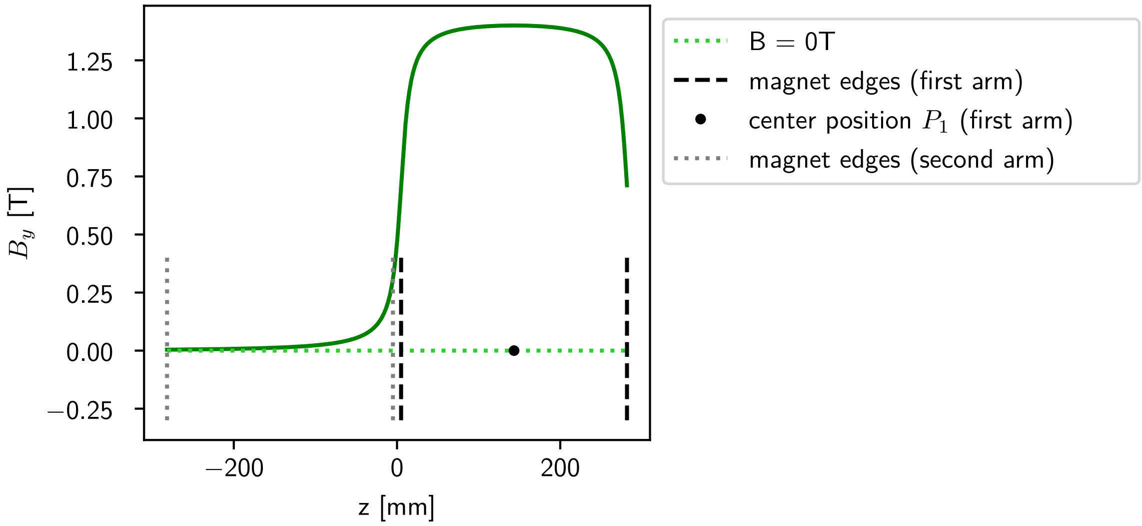

Figure 3.4: Profile of the y-component of the magnetic field along the z-direction through M_1 (illustrated in fig. 3.1) and the center position P_1 of the first spectrometer arm. The best homogeneity can be achieved around the point P_1. Especially at the edges of the magnets, where the sensor layers are positioned and the electron enters the magnetic field region, the impact of the stray field on the electron's deflection in the xz-plane has to be dealt with.

1.4 T, which is approximately the maximum value for Neodymium magnets (NdFeB) that are intended to be used. The resulting field lines and maps of the individual components for the field of one single cuboid are shown for different planes in fig. A.1, fig. A.3 and fig. A.5.

In the spectrometer setup, the magnetic field is not only influenced by the permanent magnets themselves, but also by a surrounding iron construction. In order to get a more homogeneous field in the gap between the magnets, the construction is used to redirect the field lines of the magnet faces with normal vectors pointing away from the gap (orange areas in fig. 3.2). For all four magnet cuboids of the two spectrometer arms, there are in total four such faces. Either these magnet faces of the two magnets belonging to the same spectrometer arm or of the two magnets of different spectrometer arms, but with the same y-positions, are connected with each other by the magnet construction. This ensures to connect magnet faces of different polarity such that the flux can be guided through the iron construction and thereby away from the gap, where they would influence the direction of the electron a lot more. This construction is, however, not part of the model and not implemented in the simulation. In order to take this effect into account with the model of just the four magnet cuboids, their sizes in the y-direction are set to very large values. In this case, the magnet edges facing away from the gap also do not influence the field inside the gap very much, simply because of their spacial distance in regard to the gap. The field maps for a magnet of increased y-dimension are shown in fig. A.2, fig. A.4 and fig. A.6.

Wedge Magnet Configuration

As explained in the previous section, a rather homogeneous magnetic field inside the gap region between the magnet poles can be achieved with the setup of the parallel magnet cuboids. As described in section 2.1, this results in a helical motion of the particle inside the field, if the particle does not enter the field perpendicularly to B_y. This is not wanted, because it implies that the particle moves towards a magnet pole. As the gap size between the poles is not chosen very large (3-17 mm), this might result in the particle hitting the magnet and being stopped by it before even reaching the next sensor resulting in no momentum measurement of the charged particle. This is a problem, because the multiple scattering in the sensor before the magnetic field region makes it impossible to assure that the particle enters the field exactly perpendicularly. It is therefore reasonable to consider adapting the spectrometer's design so that the stopping of the electron by one of the magnet poles is less likely to happen.

As described in section section 2.4.3, a gradient of the field component B_y in radial direction of the particle movement leads to the focusing of electrons that initially divert with respect to the y-direction due to multiple scattering in the sensor. In the spectrometer setup, a gradient $\frac{\partial B_y}{\partial z}$ in the bending plane (xz-plane) can be introduced by tilting the magnet cuboids as shown in fig. 3.5 so that the faces of the cuboids are not parallel to each other anymore.

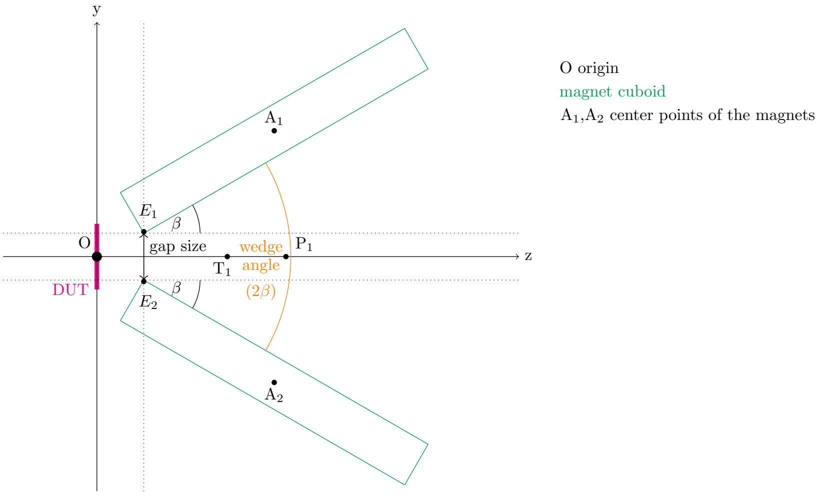

Figure 3.5: Sketch of the first spectrometer arm for the wedge magnet configuration. The gap size between the magnet poles is defined as the smallest distance between the magnets along the y-direction. A wedge angle of 2β is introduced between the magnet faces pointing towards the gap. The center positions A_1 and A_2 of the magnet cuboids (with respect to all three dimensions) are derived from geometric relations and used to calculate the resulting magnetic field, while also considering the rotation of each individual magnet cuboid by the angle $\pm\beta$ around a parallel of the x-axis, which goes through the magnet corners E_1 and E_2.

The magnetic field lines and a map of the resulting y-component of the magnetic field is illustrated in fig. 3.6.

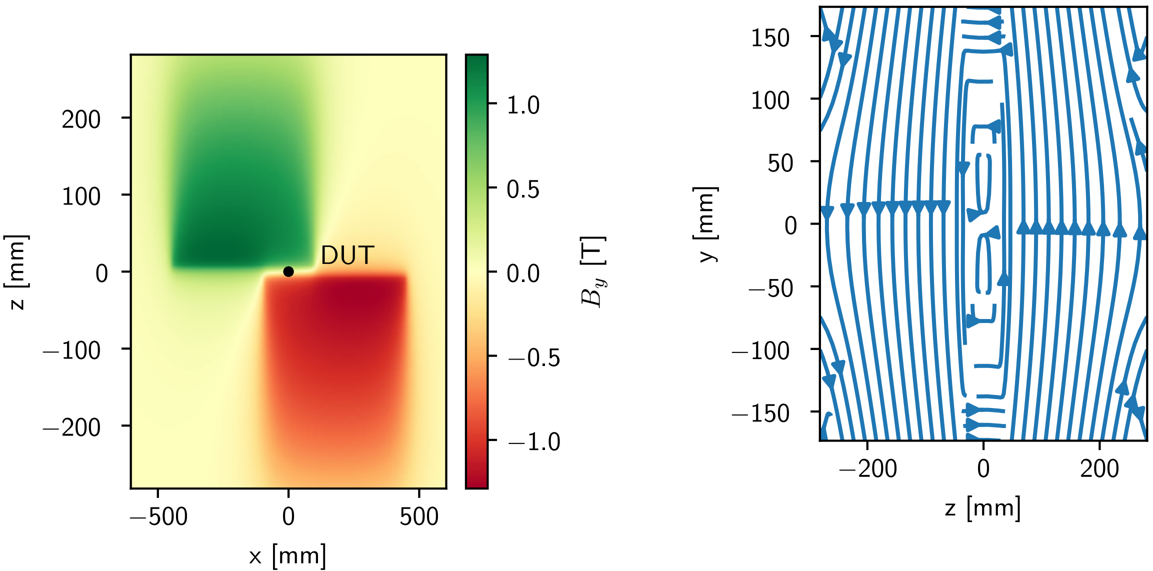

(a) Map of the B_y component in the wedge magnet configuration. The map is determined for the xz-plane with $y = 5\,\mathrm{mm}$ again. For both spectrometer arms, the gradient of the B_y component along the z-axis has a sign that results in a reduced magnetic field strength for points inside the gap between the magnet poles that are further away from the x-axis.

(b) Stream plot of the magnetic field lines in the wedge magnet configuration. The direction of the field lines is shown from the same perspective as in fig. 3.3b. As the magnet faces are not parallel to each other, the contribution of the z-component to the magnetic field becomes bigger inside the gap region between the magnet poles and the field lines in the respective regions are curved in this perspective.

Figure 3.6: Magnetic field of the spectrometer setup for the model of stacked wedged magnet cuboids. The gap between the magnet poles is set to 17 mm, the wedge angle is 0.3 rad. The field map and stream plot are obtained by modifications of the function describing the field of the parallel magnet according to the change in the positioning and the rotation of the individual magnet cubes.

In this configuration with an additional wedge angle, the distance between the magnet poles is smaller at the points where the particle enters and exits the gap between the magnet poles compared to the distance at points closer to the turning points T_i of the electron. Because the magnetization of the cuboid is constant over its entire volume, this implies that the particle is exposed to a decreasing magnetic field strength B_y during the first part of the turn and an increasing field strength during the second part. The field index n, which is described by eq. (2.17) in the local coordinate system with respect to the particle, changes along the trajectory. It describes the component of the field gradient that is perpendicular to the direction of the particle. Due to the electron's deflection, the direction of this gradient of the field index changes in the stationary coordinate system, while the direction of the gradient of the magnetic field in the spectrometer setup is constant in a stationary system. The change of the absolute value of the field index, is therefore explained by the changing angle between the direction of the particle and the direction of the gradient of the magnetic field in the spectrometer. For negative incident angles α_x, the field index even changes the sign twice. This complicates the calculation of a gradient $\frac{\partial B_y}{\partial z}$ for the spectrometer setup (in the stationary system), for which both equations (2.18) and (2.19) are equal to zero, a lot, which is why an analytical solution is not derived here. Instead, it has to be investigated with simulations whether a certain wedge angle with a focus point in the x-direction can even be found, for which the y-position of the entrance and exit point of the electron are the same. This could be given under the circumstance that the field lines are perpendicular to the momentum direction of the particle all along its trajectory in the B-field region. According to the Lorentz force given by eq. (2.1), the electron is then deflected within a certain bending plane and kept from spiraling. For a particle with a nonzero momentum in y to be perpendicular to the magnetic field, an additional z-component is therefore required. As can be seen in fig. 3.6b, the field inside the spectrometer arms does fulfill this condition. Outside the magnetic field regions, both the x- and z-components of the magnetic field are desired to be small or ideally nonexistent. The additional field maps and stream plots in fig. A.10, fig. A.11 and fig. A.12 depict the unwanted contributions of these components, which are especially high at the magnet edges.

3.3 Spectrometer Setups

In this section, specific characteristics of different spectrometer setups, that are considered, are discussed. As the energy loss measurement is gained directly and only from the energy measurements in the two spectrometer arms and because the individual spectrometer arms are symmetrical to each other, some features concerning the energy measurement are discussed only for one arm. These features can be applied analogously to the measurement in the second arm. Without further analysis, there is no obvious reason for any of the presented setups not to be compatible in combination with all magnet models. In this work, only certain combinations of spectrometer setups and magnet models are implemented in the simulation and used in the analysis.

z

3.3.1 Perfect 180 Degree Spectrometer

The Perfect 180 Degree Spectrometer shown in fig. 3.7 depicts a way to reduce influences of the magnetic stray field on the measurement. This is done by placing two sensor layers per spectrometer arm inside the gap region between the magnet poles; L1 and L2 in fig. 3.7. Thus,

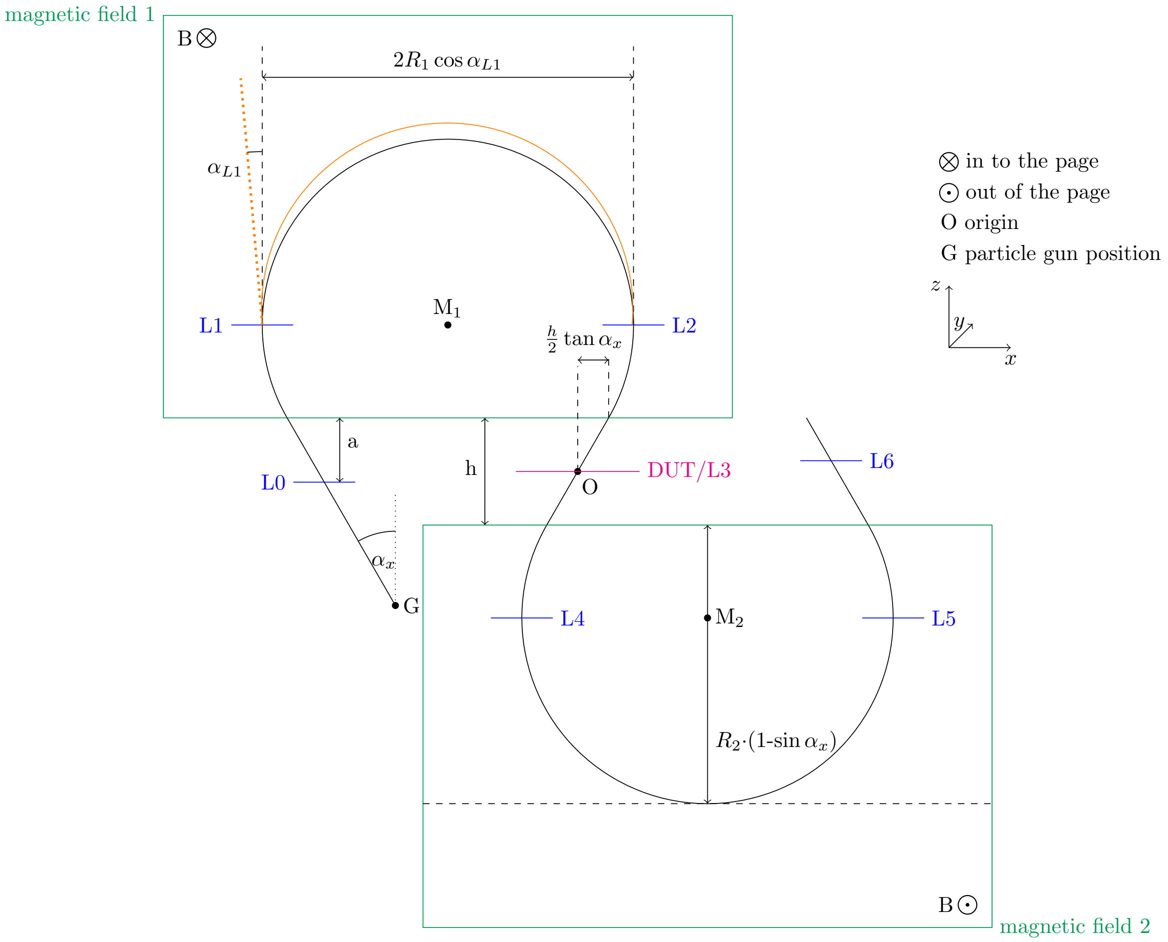

Figure 3.7: Perfect 180 Degree Spectrometer with a device under test (DUT). As a result of multiple scattering, electrons might not hit layer L1 perpendicularly as illustrated by the *orange* track of a scattered electron. The angle α_{L1} describes the deviation of the electron's direction from the perpendicular direction (z-direction) at layer L1.

the layers L1 and L2 are not placed in a region very close to the magnet edges, where stray fields become non negligible, but are rather placed in a region where the magnetic field is very homogeneous.

As the spectrometer's name suggests, the electron does an exact 180 degree turn between the measurement points at layer L1 and layer L2. Therefore, the incident angle α_x defines the exact position of these layers and the requirement $\alpha_x < 0$ must be met. For incident angles $\alpha_x \geq 0$, the electron's track forms an arc of $\leq 180°$. In that case, the layers L1 and L2 have to be positioned at the edge or outside the magnet and thus into the inhomogeneous field region. For the momentum reconstruction, only the hit positions of the two layers L1 and L2 in the rather homogeneous field region are relevant. However, the hit positions in layer L0 and layer L1 can be used to extract the angle α_{L1}, under which the particle hits the layer L1. That way, events with $\alpha_{L1} \neq 0$ due to multiple scattering in layer L0 or misalignment can be excluded, assuring that electrons of the remaining events hit layer L1 perpendicularly. Under this condition and with the approximation of homogeneous fields, layer L1 and layer L2 are in focus with respect to α_{L1}, as can be seen by the following observation.

The distance between the hits in layer L1 and layer L2 is given as:

$$\Delta x = 2R\cos(\alpha_{L1}) \tag{3.1}$$

Here, R is the bending radius of the particle's track in the magnetic field. If the particle enters layer L1 now perpendicularly (i.e. $\alpha_{L1} = 0$), this measurement is independent of the angle at first order, because the following condition is fulfilled:

$$\frac{d\Delta x}{d\alpha_{L1}} = -2R\sin(\alpha_{L1}) \overset{!}{=} 0 \tag{3.2}$$

This reduces the multiple scattering effect in layer L1, which directly affects the distance measurement.

A disadvantage of this setup is the requirement of two more sensor layers L2 and L4 compared to the other setups. This leads to additional multiple scattering, as well as additional energy loss. These effects reduce the precision of the spectrometer.

3.3.2 Single Edge Focusing Spectrometer

The Single Edge Focusing Spectrometer shown in fig. 3.8 is similar to the Perfect 180 Degree Spectrometer with the following differences. Only one layer per spectrometer arm is placed inside the gap between the magnet poles. Let L1 be the layer placed between the magnet poles in the first arm. Layer L1 is then positioned such that the focus condition along x is met at L1 and the DUT. The distance Δx between the hit position in this layer and the hit in the DUT is taken to reconstruct the deflection in the magnetic field. Let $L1_y$ be the y position of layer L1, then the homogeneous field approximation leads to the following distance:

$$\Delta x = \sqrt{R^2 - \left(L1_y - \frac{h}{2} + R\sin(\alpha_x)\right)^2} + R\cos(\alpha_x) + \frac{h}{2}\tan(\alpha_x) \tag{3.3}$$

If $L1_y$ is chosen such that the following focus condition holds, layer L1 and the DUT are in focus at first order with respect to the incident angle α_x:

$$\frac{d\Delta x}{d\alpha_x} = \frac{R\cos(\alpha_x)\left(L1_y - \frac{h}{2} + R\sin(\alpha_x)\right)}{\sqrt{R^2 - \left(L1_y - \frac{h}{2} + R\sin(\alpha_x)\right)^2}} - R\sin(\alpha_x) + \frac{h}{2\cos^2(\alpha_x)} \overset{!}{=} 0 \tag{3.4}$$

Layer L0 provides a way to check that the particle hits layer L1 perpendicularly, i.e. that the inclination angle α_x is correct.

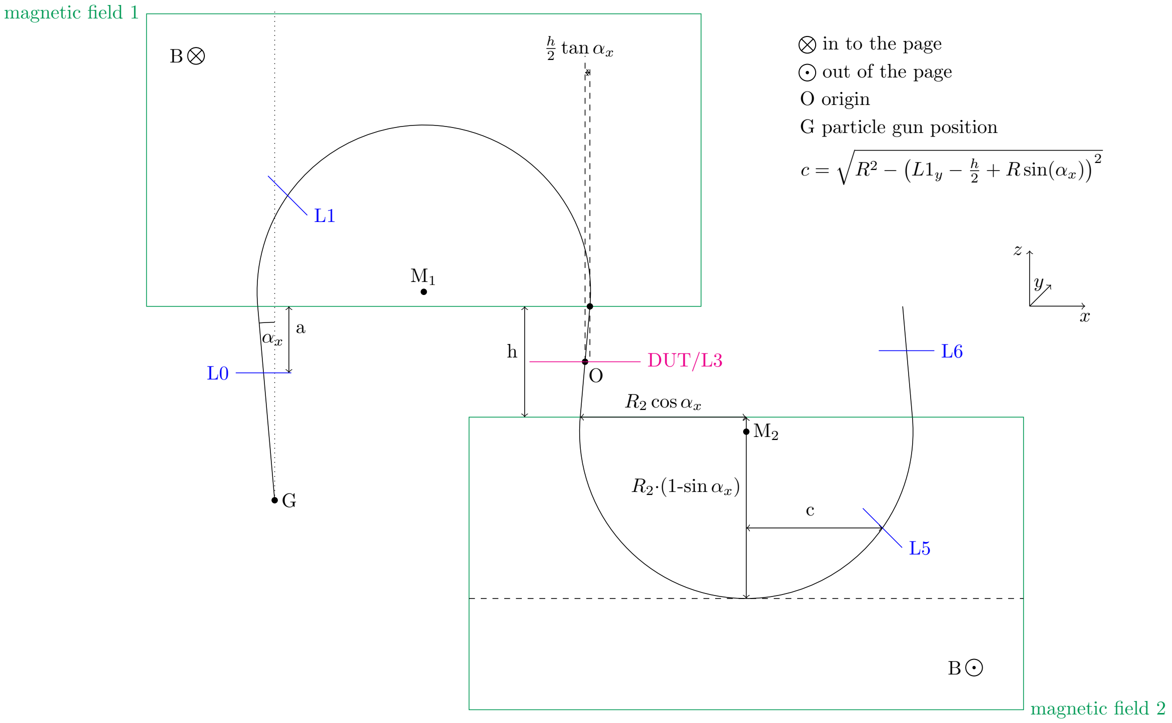

Figure 3.8: Single Edge Focusing Spectrometer with a DUT.

3.3.3 Double Edge Focusing Spectrometer

The Double Edge Focusing Spectrometer setup is shown in fig. 3.1. In addition to the DUT, which is part of both spectrometer arms, two more sensor layers are positioned outside the magnet construction per spectrometer arm, i.e. layer L0 and L1 in the first arm as well as L5 and L6 in the second spectrometer arm. No sensor layers are placed inside the gap between the magnet poles. Because the sensor layers are placed close to the magnet edges, where the inhomogeneity of the magnetic field is the biggest, the approximation with the homogeneous magnet model is not as good for this setup as it is for the other setups. Thus, it is essential to know the stray field at the magnet edges in order to correctly reconstruct the particle's track.

The layers relevant for the momentum measurement (layer L1, DUT) are in focus with respect to the incident angle α_x at first order. A calculation with the homogeneous magnetic field approximation gives the distance Δx between layer L1 and the DUT:

$$\Delta x = 2R\cos(\alpha_x) + h\tan(\alpha_x) \tag{3.5}$$

For this to be independent of α_x, the derivative needs to be zero:

$$\frac{d\Delta x}{d\alpha_x} = -2R\sin(\alpha_x) + \frac{h}{\cos^2(\alpha_x)} \overset{!}{=} 0 \tag{3.6}$$

With *eq.* (2.3), this leads to the focus condition:

$$h[mm] = \frac{2p_{\perp}[\frac{MeV}{c}]\sin(\alpha_x)\cos^2(\alpha_x)}{b \cdot B[T]} \tag{3.7}$$

Due to the correlation of the particle's momentum and the incident angle α_x according to *eq.* (3.7), the direction measurement of the particle at the entrance with the hits in layer L0 and layer L1 is necessary to check that the focus condition is fulfilled.

Because of the advantage that the sensor layers are not required to fit inside the gap between the magnet poles, the gap can be chosen much smaller for this setup. As a result of a smaller gap, the region close to the magnet edges is not affected as much by the inhomogeneity of the magnetic field as for a bigger gap. This is expected to make the correct alignment of the spectrometer components easier. For that reason, this setup was chosen for the simulation and analysis.

The focus condition for the incident angle α_x is only derived for the approximation of homogeneous magnetic fields. A calculation of the focus condition with the other magnet models is much more complex and is not conducted in the scope of this thesis. However, the setup parameters for a fulfilled focus condition correspond to the parameters with an optimum resolution in Δx. As the other magnet models are implemented in the simulation as well, a scan over these different parameters of the setup can be performed in that case. That way, the focus point can be determined experimentally. This is done as a part of the analysis in section 4.1.2.

3.3.4 Simple Spectrometer

The design of the Simple Spectrometer setup is the generalized version of the Double Edge Focusing Spectrometer setup. The components of the setup and their placements are the same with the only difference that the focus condition is not required to be fulfilled which adds more freedom in the choice of the setup parameters. Namely, the incident angle α_x and the distance h between the spectrometer arms can be chosen independently, while for the Double Edge Focusing setup eq. (3.7) must be applied to determine one parameter given the other one.

This setup is also implemented in the simulation, as it is better feasible engineering-wise and it has the same advantage of not having any layers inside the gap between the magnet poles. Additionally, it is needed for the search of the focus point in the analysis of the inhomogeneous magnet model.

3.4 Monte Carlo Simulation with Geant4

For the simulation written in C++, the object-oriented software toolkit Geant4 [1] is used to implement the spectrometer. It provides a way to perform a full Monte Carlo Simulation of various particles interacting with matter. A Monte Carlo Simulation takes random samples to find a solution for problems involving statistically distributed processes, as it iteratively simulates the problem. [12, 8]. This is a method to also efficiently solve problems that would be hard to solve analytically. The toolkit provides the framework for particle transport, geometry description, material specification and the management of events [12].

To build the simulation, the geometry of the experimental setup needs to be described. This is done by defining each component as a volume and placing it at the desired positions in space. Materials are then assigned to the volumes. If the volume is supposed to detect particles passing through, as well as to measure the energy deposit in the respective volume, the volume is marked as a so-called ‘sensitive’ volume. Additionally, the magnetic field region needs to be set. Depending on which of the magnet models described in *section* 3.2 is simulated, a corresponding function is defined that describes the magnetic field strength at each point in the specified field region.

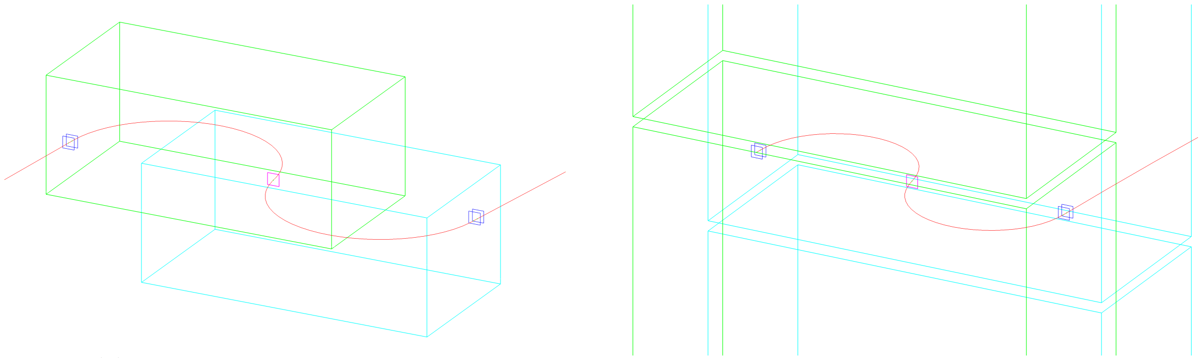

(a) homogeneous magent model

(b) model of parallel magnet cuboids

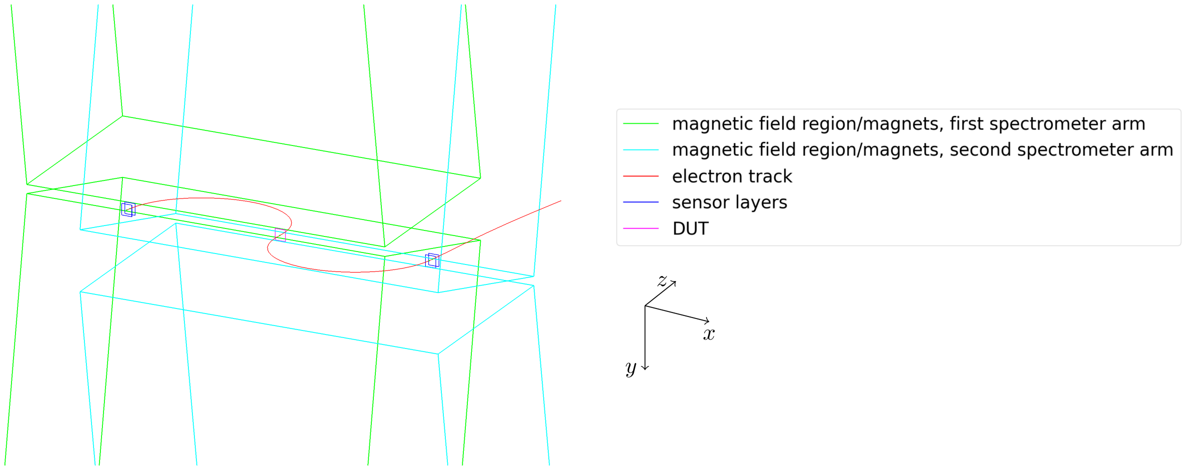

(c) model of wedged magnet cuboids

Figure 3.9: Visualization of the electron track in Geant4 for setups with different magnet models. The *green* and *blue* boxes represent the magnetic field regions for the homogeneous magnet models and otherwise the contours of the magnet cuboids. The electron track is colored red and passes the different blue sensor layers as well as the *pink* DUT.

In the simulation, the spectrometer setups of the Simple Spectrometer and of the Double Edge Focusing Spectrometer are implemented as given in fig. 3.1. The visualization of the resulting simulated geometry can be seen in fig. 3.9. Each sensor L*i*, as well as the DUT, is simulated as a $2 \times 2\,\mathrm{cm}^2$ layer of silicon. They are each 50 µm thick, except for the DUT, which is chosen to be 600 µm thick. The pixel pitch of both the DUT and the sensors is 80 µm. Only the volumes of the sensors and the DUT are set to 'sensitive'. The surrounding material in the experimental setup called the 'world material' can be chosen from vacuum, helium and air. If not stated specifically, all simulations are conducted with the surrounding material vacuum. For the magnet model of a homogeneous field depicted in fig. 3.9a, the specified field region of the first arm is visualized as a green cuboid, the field region of the second arm corresponds to the *cyan* cuboid. Here, only the field regions, but not the magnets themselves are simulated, which means that the entire field region is assigned to the surrounding material. The positions of both the field regions and the sensor layers are set to the calculated positions based on the geometric relations for the expected radius R and the initial angle α_x. For the realistic magnet models, the magnet cuboids are simulated as cuboids of iron. In the visualization, these are depicted as green cuboids for the first spectrometer arm and as *cyan* cuboids for the second arm. The center positions of the magnets, which are needed for the positioning of the magnets in the simulation and for the correct calculation of the resulting field, are defined by the magnets' dimensions and the wedge angle. The positions of the layers cannot be easily calculated for the inhomogeneous case. Therefore, the positions are determined through additional simulations. These simulations are explained at the end of the next paragraph.

In each simulated event, a single electron with the initial total momentum of 53 MeV/c is shot with a 'particle gun'. Possible misalignment is not simulated, i.e. the particle hits the first layer L0 at the center with respect to the x- and y-direction. For the realistic magnet models shown in fig. 3.9b and fig. 3.9c, this is assured by setting the starting position of the electron as the point right in front of layer L0 (along the z-direction) at this center position such that even for the magnet models with an inhomogeneous field the electron is not deflected before hitting the first layer. The initial direction of the electron lies within the x,z-plane under an angle α_x with respect to the z-direction. Angles in the range of -0.6 rad to 0.6 rad are chosen for different types of analyses. For some parts of the analysis, only the influence of the magnetic field on the particle's trajectory is to be investigated. For that purpose, virtual particles of the Geant4 toolkit called 'charged geantinos' are used instead of electrons. They do not interact with matter, but are deflected in the magnetic field in the same manner as electrons. For the realistic magnet models, these virtual particles are also used in the simulations to determine the layer positions in a given setup configuration. As the positions are initially unknown, the sensor dimensions in the x-direction are chosen big enough to assure that the particle hits each sensor even when the sensor is positioned at a wrong x-coordinate. The initial x-positions of the sensor layers are then adapted using the obtained x-positions of the simulated hits. When moving the layers closer together or further apart, the starting position of the particle changes so that it still hits the first layer L0 at its center. Because of this, the particle does not see the exact same field along its track for the next run and as a consequence the deflection of the particle changes slightly. As a result, it does not hit the sensor layers at exactly the same positions as in the previous run. Therefore, the whole process of simulating and adapting the layer positions is repeated - in total three times - to get a more exact result for the sensor positions where the geantino hits the center of the sensor layers. After this, the sensor size in the x-direction is switched back to 2 cm and the actual simulations can begin.

Geant4 provides certain physics lists where different physics processes are included. The physics models describing these processes also vary for different physics lists and energy ranges of the used particles. The particle transport is simulated in steps. For each step, the individual included processes compete with each other. The choice of process is made based on their cross-sections. The track information, e.g. the particle's energy or its position, is updated for the next step. The standard electromagnetic physics in Geant4 includes multiple scattering, the continuous energy loss by bremsstrahlung and by ionization, as well as δ-ray production, synchrotron radiation and compton scattering. More details on the implementation of the models are discussed in [1]. In the simulation, the standard physics list `FTFP_BERT` for electromagnetic physics dealing with low energies is used with the default and recommended constructor `G4EmStandardPhysics_option4`. This list uses a combination of the best models for the implemented processes [3].

The output of the simulations contains different types of information. The truth information includes values that are defined or set before the simulation is started, e.g. the initial position, direction and momentum of the particle. Additionally, Geant4 provides information like the track ID or the parent ID, which differentiate primary particles from secondaries and assign secondary particles to their parent particle. These types of quantities are generally only known in simulations, but not when carrying out the experiment in reality. Therefore, they are not to be used for the measurement or the evaluation of the data, i.e. not for the reconstruction. However, they can be used for analysis purposes, especially in order to assess the correctness and accuracy of the obtained results. When Geant4 simulates the physical processes and tracks the particle's momentum and position along its trajectory, it obtains the hit positions at the sensor layers. These exactly simulated hit positions are also stored in the output, but are still not the kind of information that is also known in an actual data set from a real world measurement. In order to get a realistic data set from the simulation, the processing of data during the readout of hits in a pixel sensor has to be taken into account. Therefore, the sensor layer is described as a grid of pixels which each have a pixel width of 80 µm in the x- and y-direction. Each individual pixel is defined by its row and column number. The simulated hit positions are assigned to the respective pixel in which they are detected and the center position of this pixel is stored. That way, the pixel resolution of the sensors is considered.

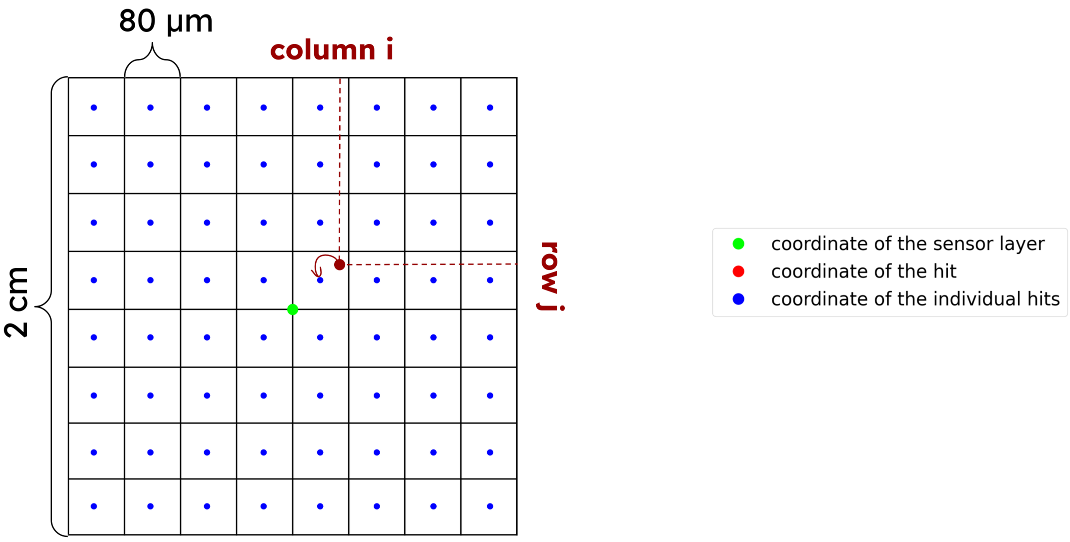

Figure 3.10: Example sketch of a $2 \times 2\,\mathrm{cm}^2$ sensor layer. The illustration shows only a portion of the pixels and is therefore not to scale. The total width, as well as the pixel width of 80 µm apply to both dimensions. A particle leaving a hit at a certain hit position (*red* point) is assigned to a row number i and a column number j based on the pixel in which it is detected. Using the coordinate of the sensor layer (*green* point), the row and column number are transformed to the respective pixel position (*blue* point).

3.5 Track Reconstruction

In this section, only the track reconstruction for the Simple Spectrometer and the Double Edge Focusing Spectrometer is discussed, as these two setups are implemented in the simulation and refered to in the analysis and evaluation. The reconstruction uses the homogeneous magnetic field model with a field strength of $B_y = 1\,\mathrm{T}$. For the other magnetic field models, a numerical track reconstruction is likely possible, but this exceeds the scope of this thesis. For that, geantinos could be used to simulate the 'ideal' trajectory of electrons, where the interaction with matter is neglected. The deflection of geantinos with the measured direction, but various different values for the particle momentum, could be simulated. A comparison of the simulated and observed hit positions would then allow a reconstruction of the momentum.

In the case of an approximated homogeneous field, however, simple geometric relations can be used for the reconstruction as explained in section 3.2.1. Here, the track of the electron inside the magnetic field region is a circular arc with the radius R according to equation eq. (2.3). The measured distance Δx in the first (second) spectrometer arm between the hit x-positions in layer L1 (L5) and the DUT is therefore given by eq. (3.5). From that the transverse momentum $p_\perp$ is derived as:

$$p_\perp \left[\frac{\mathrm{MeV}}{\mathrm{c}}\right] = b \cdot B[\mathrm{T}] \cdot \frac{\Delta x - h\tan(\alpha_x)}{2\cos(\alpha_x)}[\mathrm{mm}] \tag{3.8}$$

Thus, the reconstruction of the angle α_x, which defines the electron's direction in the field free region, is necessary. To take possible direction changes due to multiple scattering of the electron inside the first spectrometer arm into account for the momentum measurement in the second arm, the value of α_x that is measured before the electron enters the first field region is only used for the calculation of the momentum in the first arm. Another measurement of α_x is taken after the particle has exited the second magnetic field region and is used for the reconstruction of the momentum in the second arm.

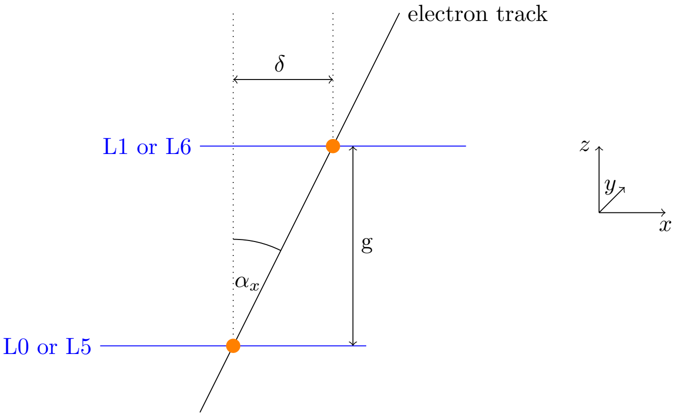

Figure 3.11: Direction measurement of the electron. The electron leaves hits in two monolithic sensor layers (*blue* lines). For the first spectrometer arm layer L0 and L1 are used, for the second arm layer L5 and L6. The angle α_x is reconstructed from the difference between the x- and z-positions of the hits (δ and g).

For each spectrometer arm, the distance δ is defined as the difference between the x-positions of the hits (*orange*) in the monolithic pair of pixel sensors, i.e. layer L0, layer L1 for the first arm and layer L5, layer L6 for the second arm (see fig. 3.11). This parameter δ is related to α_x by

$$\alpha_x = \arctan\left(\frac{\delta}{g}\right), \tag{3.9}$$

where g is the distance between the two monolithic layers.

The momentum loss p_{loss} is obtained from the reconstructed momenta p_1 and p_2 in the first and second spectrometer arm as the difference

$$p_{loss} = p_1 - p_2. \tag{3.10}$$

The track reconstruction takes the simulated hit x-positions in each event as an output from the simulation and then reconstructs the transverse momentum according to the formulas above in a C++ code [7]. As described in section 3.4, the exactly simulated hit positions, as well as the x-positions after the readout given by the pixel positions, are both included in the simulation output. The reconstruction is done for both, cases allowing the effect of the pixel resolution on the reconstructed momentum to be investigated separately from the resolution that includes all simulated effects. With the reconstruction starting from the hit in the last layer L6 of the spectrometer, only the momentum for events where the electron actually reaches the last layer of the second spectrometer arm are reconstructed.

Chapter 4

Analysis

In this chapter, the direct output of the simulation, as well as reconstructed simulation output obtained from the calculation in section 3.5 is analyzed based on the following figure of merits: the energy loss, the momentum, the distance Δx, the angle α_x, the resolution, the efficiency, the purity of the reconstructed tracks.

4.1 Resolution

To determine the resolution of the spectrometer, the simulation is run either with the Simple Spectrometer geometry or the Double Edge Focusing Spectrometer geometry where each run contains 10000 events. As pointed out in section 3.3.4, the geometry of the implemented setups is the same. The difference lies in the free choice of values for the setup parameters of the Simple Spectrometer compared to the restriction in the Double Edge Focusing Spectrometer to fulfill the focus condition of the distance measurement Δx with respect to the incident angle α_x. Since an analytical solution of the focus condition was only calculated for the homogeneous field approximation in section 3.3.3, the setup parameters in focus in the inhomogeneous magnet models first need to be found through simulations with the Simple Spectrometer Setup. Therefore, all following discussions for the homogeneous magnet model base on results from simulations with the Double Edge Focusing Spectrometer Setup, which promises a higher resolution, whereas investigations with the inhomogeneous magnet models are made in the Simple Spectrometer setup. As the momentum reconstruction is implemented only for the magnet model of homogeneous fields, but not for the other two magnet models, the resolution of the energy loss measurement is determined differently for these models. This is described in the following sections.

4.1.1 Homogeneous magnetic field model

For an approximate evaluation of the momentum resolution, the homogeneous magnetic field is simulated and the transverse momentum is directly reconstructed from the hit positions as described in section 3.5. The momentum resolution is then derived from the momentum distribution over the individual events which is shown in the histogram in fig. 4.1.

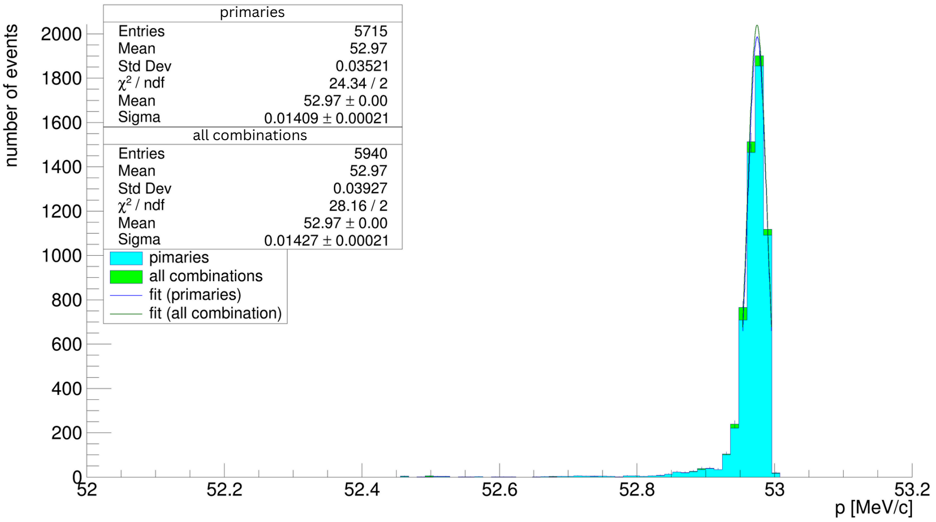

Figure 4.1: Momentum distribution in the first spectrometer arm over 10000 events for the homogeneous magnet model with a distance h of 10 mm and an incident angle of $\alpha_x = 0.1$ rad. In the histogram of primaries, the truth information of the simulation is used to differentiate hits of primaries from hits of secondary particles such that only the momenta of primary particles are reconstructed, which results in a maximum number of one reconstructed track per event. The histogram with all combinations considers the contribution of wrongly reconstructed momenta due to indistinguishable hits of secondary particles and is thus closer to the reconstructed momentum distribution for a measurement of an electron beam with the spectrometer. With additional hits of secondaries, more combinations between hits in the different sensor layers can be made leading to the possibility of more than one reconstructed track per event and thus increasing the number of entries in this histogram. The mean value and rms deviation of the distribution stated in lines two and three of the legends are obtained by all values in the respective histograms. The second mean value and the standard deviation σ are the obtained fit parameters of the Gaussian fit. The χ^2 value divided by the number of degrees of freedom ndf is a measure for the goodness of the fit.

This distribution has a peak with a certain width that corresponds to the momentum resolution of one spectrometer arm. The width of this peak is determined by a Gaussian fit. The fit range is initially chosen to include all values with a deviation of $\pm 0.2\,\mathrm{keV/c}$ and adapted in an iteration of five fits to the new range $\pm 1.5\sigma$ around the mean. A number of outliers is expected, due to multiple scattering. If the scattering happens in layer L1 or after L1, it leads to a change of the particle's direction after the measurement, which cannot be accounted for in the track reconstruction. Considering that the number of events in an actual measurement of an electron beam with the spectrometer is very high, these outliers are easily distinguishable from the peak and the respective events can be excluded so that such large outliers do not contribute to the momentum resolution.

The resolution of the momentum loss measurement can roughly be estimated by multiplying the momentum resolution with the factor $\sqrt{2}$, as the energy loss is calculated from the difference of the two measured momenta values in the two spectrometer arms. To experimentally determine it, the momentum loss can directly be calculated for each event and the resolution can be obtained from the distribution again. The width of the peak in fig. 4.3 with a value of 24.8 keV/c shows that the theoretically determined value of $\sim 20\,\mathrm{keV/c}$ from the momentum resolution of one spectrometer arm underestimates the momentum loss resolution. The reason for that is the increased multiple scattering effect on the momentum measurement in the second spectrometer arm, which leads to a bigger momentum resolution compared to the first arm (see fig. 4.2). While the electron always starts from the same exact position under the same exact angle α_x before entering the first arm, it is likely already deflected after passing through all the material of the first spectrometer arm – even before reaching the first layer (the DUT) in the second arm. What adds to that, is the increased thickness of the DUT compared to the other sensor layers which results in even more multiple scattering before the measurement in the last two layers of the arm. Taking into account this difference between the momentum resolution Δp_1 in the first arm and Δp_2 in the second arm, the obtained momentum loss resolution of 24.8 keV/c of from the simulation is even better than the theoretically estimated value of the momentum loss resolution, given by

$$\Delta p_{loss} = \sqrt{(\Delta p_1)^2 + (\Delta p_2)^2} \approx 29.0\,\mathrm{keV/c}. \tag{4.1}$$

From the determined mean value of 52.97 MeV/c in the histogram in fig. 4.1, one can derive that the measurement with the spectrometer underestimates the true initial momentum of the electron. The accuracy of the momentum measurement can, however, be improved through a calibration with a configuration where a sensor layer replaces the DUT. Thereby, an additional offset in eq. (2.3) is introduced.

4.1.2 Optimizations for the realistic magnetic field model

For the magnet models of parallel or wedged cuboids, the momentum reconstruction is not implemented as explained in section 3.5. Instead of the momentum resolution itself, the quantities influencing the resolution are investigated. These quantities are the incident angle α_x and the distance Δx that is measured between the hit x-positions in the layers L1 and the DUT.

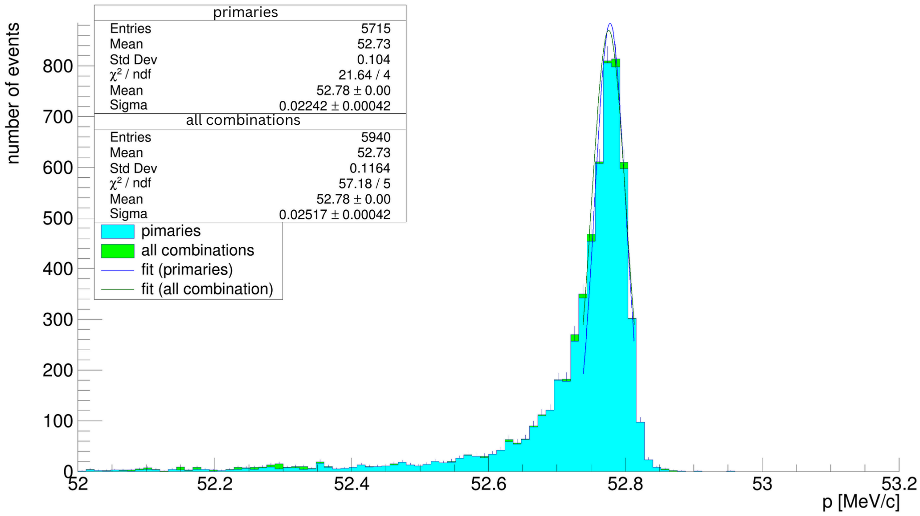

Figure 4.2: Momentum distribution in the second spectrometer arm over 10000 events for the homogeneous magnet model with a distance h of 10 mm and an incident angle of $\alpha_x = 0.1\,\text{rad}$. The histogram is obtained in the same manner as fig. 4.1 and depicts the same quantities, but for the second spectrometer arm.

Angle Measurement α_x

The resolution of the angle measurement α_x consists of two uncertainties, the angular hit uncertainty and the multiple scattering uncertainty. With the relative radiation length $\frac{x}{X_0}$ of one sensor, the multiple scattering uncertainty θ_{rms} that results from the particle traversing one sensor layer is given by eq. (2.13). For the sensors used, which are made of a 50 µm thick layer of silicon, the radiation length X_0 is approximately 9.370 cm [12]. The length x that the electron covers inside of one sensor layer is defined by the incident angle α_x, fixing the angular multiple scattering uncertainty to one fixed value for a given value of α_x. Thus, the resolution of the angular uncertainty is minimized to the best possible resolution by requiring the angular hit uncertainty to be in the same order of magnitude. The angular hit uncertainty for one sensor layer is proportional to the quantity

$$\frac{\sigma_t}{g} = \frac{\text{pixel width}}{\sqrt{12}g} \tag{4.2}$$

where σ_t is the pixel resolution of the sensor calculated from its pixel width of 80 µm and g is the distance between the sensor layers L0 and L1. This implies that the angular uncertainty is minimized for the condition

$$g \geq \frac{\sqrt{2}\sigma_t}{\theta_{rms}}. \tag{4.3}$$

The additional factor $\sqrt{2}$ is added to account for the angular hit uncertainty in both the layers L0 and L1. The parameter g was chosen as 10 mm in all simulations, which meets this condition eq. (4.3) in any configurations used.

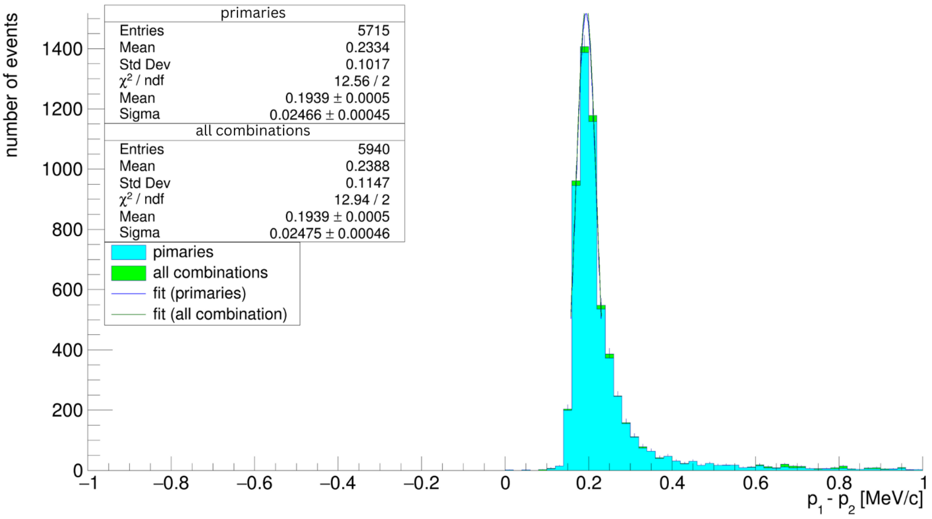

Figure 4.3: Momentum loss distribution over 10000 events for the configuration with a distance h of 10 mm and an incident angle of $\alpha_x = 0.1$ rad T. The momentum loss distribution is noticeably wider than the momentum distribution of the first spectrometer arm. Opposite to the momentum distribution, the momentum loss distribution has a tail towards bigger values. The main reason for these two observations is the difference in starting conditions before the momentum measurement in the individual spectrometer arms is carried out. Before entering the first arm, electrons of different events all start with exactly the same total momentum, position and direction. For the measurement in the second arm, multiple scattering and the slight difference in energy loss in the first arm and in the DUT causes the electrons of different events to enter the second arm from different positions, with different directions and momenta, such that the momentum distribution becomes wider and more events contribute to the tail of smaller momenta values in comparison with the measurement in the first arm. Since the momentum of the second arm with the bigger tail is subtracted from the momentum in the first arm, this results in a tail with bigger values for the energy loss distribution.

Distance measurement Δx

The resolution of the measured distance Δx can be obtained from its distribution over the events in an analogous manner to how the momentum resolution is obtained from its distribution for the homogeneous magnet models. Both the pixel resolution and the multiple scattering uncertainty contribute to the resulting Δx resolution. For different setup parameters, namely the distance h between the spectrometer arms, the gap size between the magnet poles, the wedge angle and the incident angle α_x, the pixel resolution does not vary for sensors with a fixed pixel width. Thus, optimum setup parameters are given as the ones fulfilling the focus condition with respect to the incident angle α_x, which minimizes the influence of multiple scattering on the Δx measurement. As the analytical calculation of the focus condition is beyond the scope of this thesis, the optimal setup parameters are obtained by systematically scanning them.

For each point of the scan, the simulation has to be run separately with the corresponding setup parameters. The Δx resolution of each of the spectrometer arms is expected to be minimum for the same setup parameters, so it is sufficient to analyze the Δx resolution of only one spectrometer arm. For the first spectrometer arm, the distance Δx is given as the difference between the x-position of the hit at the DUT and the x-position of the hit at layer L1. Changing any of the parameters that are to be scanned does not change the resolution for the x-positions at layer L1. Therefore, minimizing the spread of the x-positions at the DUT minimizes the Δx resolution. This reasoning cannot be applied to the Δx measurement in the second spectrometer arm, as both the spread of x positions at the DUT and at layer L5 are influenced by the parameters to be scanned. Therefore, it is easier to obtain the correct focus parameters from the Δx distribution of the first spectrometer arm by looking at the spread of x-positions at the DUT for each configuration of the focus scan and trying to minimize it in the measurement. Like the momentum resolution and the Δx resolution, the x spread is estimated again by looking at the σ parameter of the fitted gaussian function to the peak of the distribution with x-positions at the DUT.

Y range filter

As a first step to minimize this spread in any configuration, the correlation between the x- and y-position of the hit at the DUT is used to exclude further outlier events that are still in the fitted x-range but have a reconstructed momentum which is too small compared to its actual total momentum. As described in section 3.5 only the transverse momentum, not the total momentum, is reconstructed. Electrons with y-positions $\neq 0$ have gained a momentum component in y-direction, e.g. because of multiple scattering. As a result the transverse momentum decreases.

For the homogeneous case, this correlation between the x- and y-positions depicted in fig. 4.4 can be calculated from geometric relations. Assuming to have shot an electron from the center position of layer L0 and to have measured a certain hit position at layer L1, the incident angles α_x and α_y are directly given by these two hits. To calculate the expected hit positions at the DUT for a given total momentum p_{tot}, the following relation is used to obtain the transverse momentum $p_\perp$.

$$p_\perp = p_{tot} \cos(\alpha_y) \tag{4.4}$$

The corresponding Δx resulting from eq. (3.8) can be added to the measured x-position in layer L1 to determine the expected x-position in the DUT. Let $s_\perp$, illustrated in fig. 4.5, be the length of the projection of the track between layer L1 and the DUT to the xz-plane, then the y-position at the DUT can be calculated by

$$y_{DUT} = y_{L1} + s_\perp \tan(\alpha_y), \tag{4.5}$$

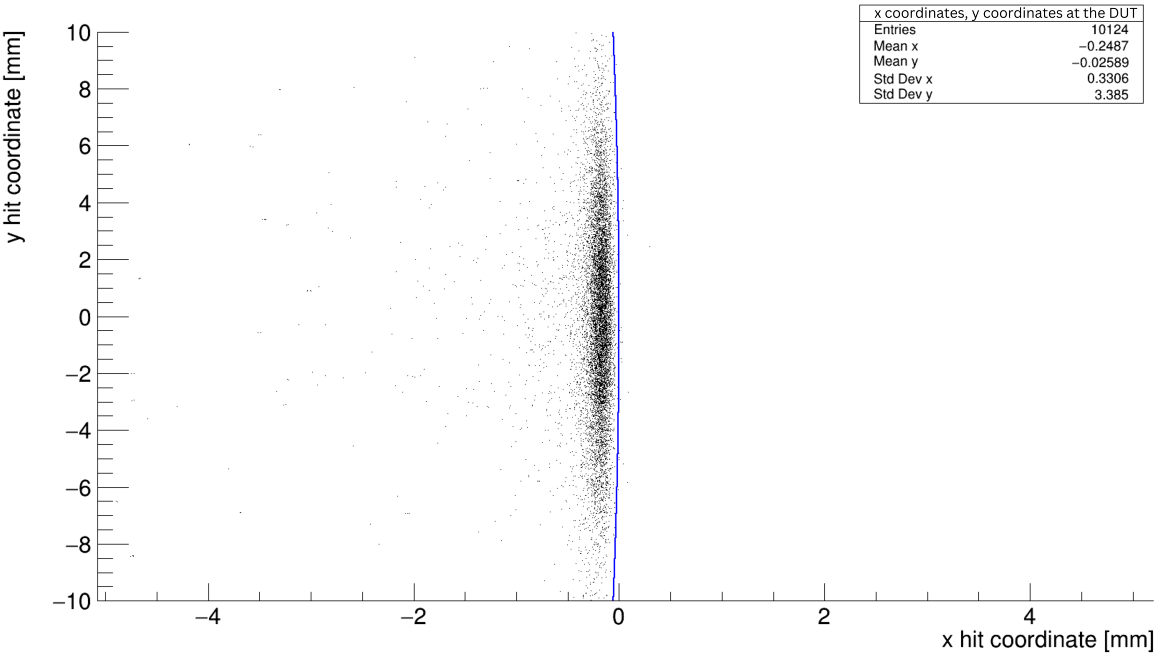

Figure 4.4: Correlation of x coordinates and y coordinates at the DUT. As the correlation can only be predicted for the homogeneous field approximation, the simulation is run for this model. For a better comparison between the actual hit positions at the DUT in the experimental setup and the expected ones based on the analytical calculation (*blue* curve), the pixel resolution is not simulated. The hits of secondaries are included.

where y_{L1} is the measured y-coordinate at layer L1.

It can then be checked, if the calculated x- and y-positions of the hits at the DUT coincide with the simulated ones. In fig. 4.4 the measured x- and y-positions at the DUT are shown along with the calculated positions that are displayed as the *blue* curve. It shows that the curve of the calculated values seems to correspond with the shape of the simulated values.

However, an offset of the x-coordinates indicates a bias of the Δx distance measurement towards smaller values. This bias appears, since both deviations towards bigger angles α_x and deviations towards smaller angles α_x lead to a smaller value for the measured distance Δx.

By limiting the accepted y range of the hit positions at the DUT to a certain range around 0, the influence of the described effect on the measurement can be reduced improving the resolution a lot. Because of this observation, the spreads of different y ranges are investigated separately. For that, the hits are assigned to one of the categories "center" y range, "outer" y range or y range of "outliers" which are defined as depicted in fig. 4.6.

To determine the respective x spreads, only the reconstructed events that have a hit with a y-coordinate in the respective range are kept and used in the distribution of x-positions as shown in fig. 4.7 for an example configuration. The decision to set the acceptance limit to these specific values was made based on an observation of the therefore decreasing efficiency, as well as the

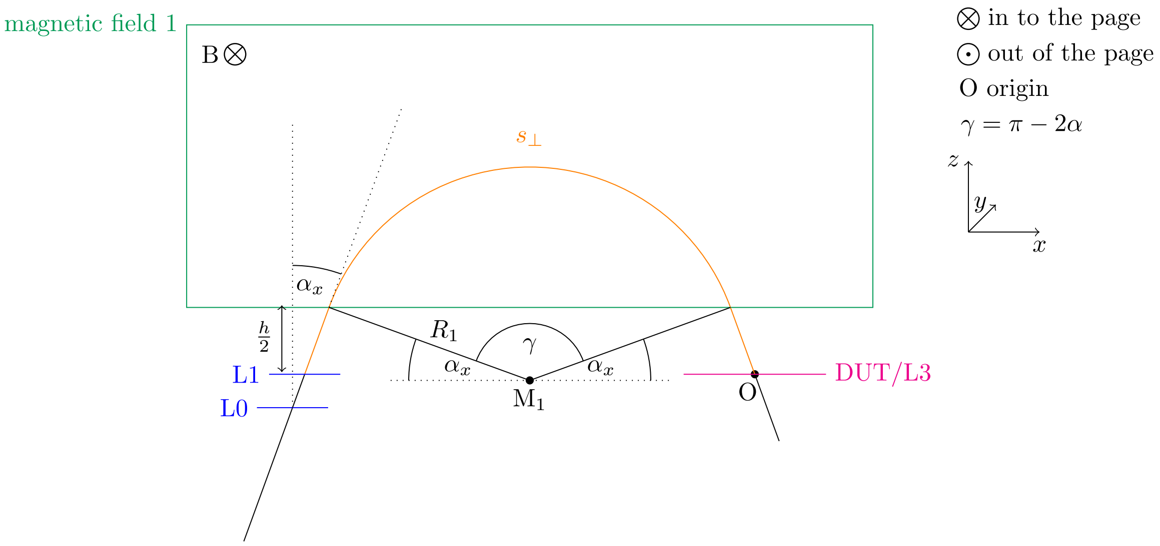

Figure 4.5: Track from layer L1 to the DUT. Using geometric relations, the length $s_\perp$ of the projection of this part of the track depicted as an *orange* path to the xy-plane can be calculated with the relation $s_\perp = R(\pi - 2\alpha) + \frac{4\cos(\alpha)}{h}$.

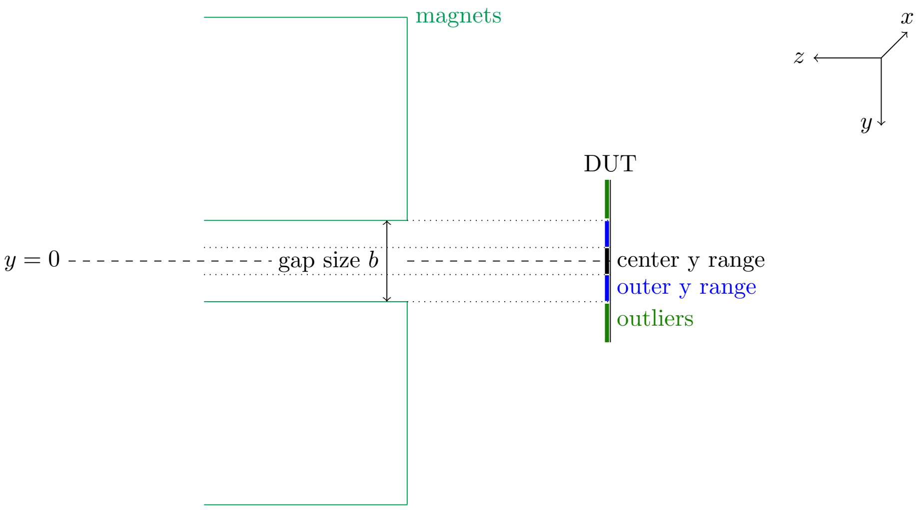

Figure 4.6: Categories for y ranges of the hits at the DUT. When the electron exits the gap between the magnets of the first spectrometer arm, which are depicted here by the *green* cuboids, its momentum component in the y-direction determines the y-position of the hit detected at the DUT. Each hit at the DUT is assigned to a certain y range category based on its y-coordinate so that the categories represent certain ranges of the corresponding momentum component in the y-direction. If b is the gap size between the magnet poles of the chosen configuration, then all hits at the DUT with a y-position of $\pm\frac{1}{3}b$ are categorized as a hit in the center y range, hits with a bigger y-position that is still within $\pm b$ are considered to be in the outer y range. All hits with a y-position $> b$ are described as outliers.

improvement of the resolution. This can, however, be further analyzed and adapted depending on how much loss in efficiency can be approved of and how much more improvement of the resolution is given for even smaller ranges.

Spread of x-positions at the DUT

For the focus scan analysis, the exactly simulated hit positions are used instead of the pixel positions, i.e. the output of the simulated readout process described at the end of section 3.4 is not used. This implies that the influence of the pixel resolution on the Δx resolution is not considered here. That way, the optimum parameters can be determined more precisely, as the pixel resolution does not add to the uncertainty of the determined optimum setup parameters.

Another more technical error on the x spread is introduced, because the spread is not determined directly from the simulated values. The quantification of the simulated values through the assignment of the values to the respective histogram bins changes the fit. Because the fit is done to the binned values, it depends on the chosen bin size and the positioning of the bin mean. To take this error into account, the fit is done multiple times. For 10 different fits, the values are put into histograms with the same bin size of 40 µm, but different positions of the bin means. The value used for the focus scan is the mean of the x spreads for the fits with the differently shifted bin means. The error of this mean x spread value is calculated from the errors of the individual spreads and the deviation of the individual spreads to this mean value. The influence of the bin mean shift on the x spread is shown in fig. 4.8.

Scan of the incident angle α_x

Scan of the incident angle The first scan parameter is the incident angle α_x. For each combination of a certain gap size between the magnet poles and a certain wedge angle, the x spread is determined for varying values of the incident angle α_x. This is done for a fixed value h. As shown in fig. 4.9 for an example configuration, a clear minimum value of the x spreads can be found. With this, the optimum incident angle α_x for a given gap size between the magnet poles and a given wedge angle, is determined as the incident angle that belongs to this minimum.

Scan of the wedge angle

In order to also chose a value for the wedge angle between the magnet poles, the dependency of the x spread on the wedge angle is investigated. For that, a scan over different wedge angles is done, where the gap size is fixed, but the incident angle is already set to the previously determined optimal incident angle for the respective configurations, i.e. the incident angle varies for the different points of the scan. This scan in fig. 4.10 shows that there is no clear minimum

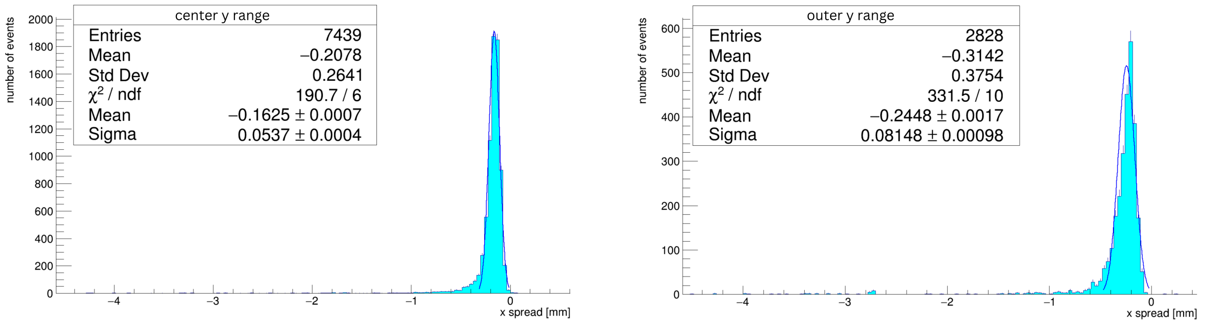

(a) center y range (b) outer y range

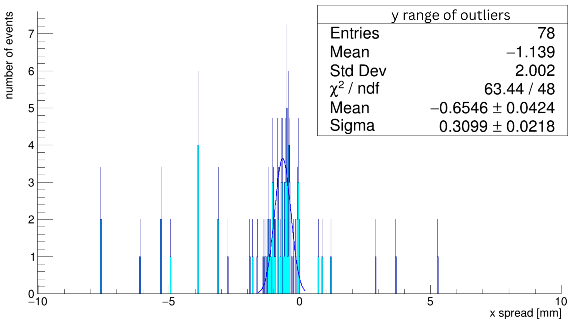

(c) y range of outliers

Figure 4.7: Distribution of x-positions at the DUT. A filter based on an accepted range of the y-positions at the DUT is applied. The chosen range differs for the individual histograms and is defined by the stated y range categories. The histograms result from simulations using a configuration with a gap size of 17 mm between the magnet poles, a distance h of 10 mm, a wedge angle of 0.3 rad and an incident angle of 0 rad. The reconstruction of tracks that include hits left by secondaries is considered, as the histograms are filled for each reconstructed track of an event. In the case of an event with a secondary leaving a hit at another sensor layer (and not at the DUT), two tracks are reconstructed using the same hit at the DUT such that the histogram with the corresponding y range of this hit, is filled twice with the same x-position at the DUT. With this filling procedure of the histograms, it is assured that the same reconstructed tracks represented in the Δx distribution are also represented in the x spread distributions, which is required in order to make correct conclusions from the resolution of the x spread to the Δx resolution. The y range closest to $y = 0$, used in histogram fig. 4.7a, has the smallest x spread with a value of 0.05 mm. The further away from $y = 0$ the accepted y-ranges become, the bigger the deviations from the mean of the distributions get. For large deviations of the hit y-positions as in fig. 4.7c, outlier x-positions with large deviations from the mean become much more probable making the rms value of the distribution more conclusive than the obtained σ value from the Gaussian fit. Regardless, the fitted σ can be taken as a measure to compare the x spreads in the focus scan, as the described behavior of the deviations in the histograms suggest to exclude such large y ranges from further investigation to improve the resolution.

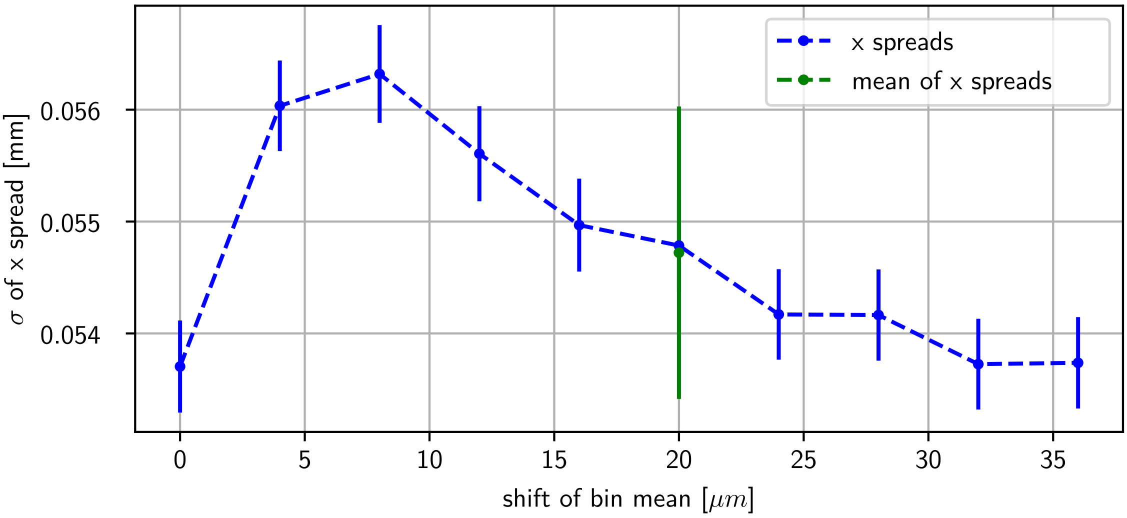

Figure 4.8: x spread at the DUT for different positions of the histogram's bin means and a configuration with a gap size of 17 mm between the magnet poles, a distance h of 10 mm, a wedge angle of 0.3 rad and an incident angle of 0 rad. The simulation is run just once in the stated configuration and the same output is taken as the data set for all shown data points. The x-positions at the DUT are fitted in a histogram with a bin width of 40 µm. The fit range is kept the same, while each center position of a bin in the histogram is shifted by the value given on the x-axis. The σ and error of the σ obtained by the fits are plotted against the shift of the bin center positions. The deviations in the obtained σ values show that the binning influences the determined σ. The sigma value is therefore determined as the mean of all determined σ values and the error is calculated from the errors of the individual σ values and their deviation to the mean.

like for the scan over the incident angles. Still, it becomes apparent that the resolution worsens for bigger wedge angles. This motivates the choice of smaller wedge angles or even the setup with a wedge angle of 0 rad, which corresponds to the magnet model of the parallel magnet cuboids.

Both of the described scans were also done for different distances h. The results showed, however, that the optimum incident angles remained the same and the x spreads for these configurations also did not remarkably change. This leaves the choice to set the parameter to a value such that the construction of the spectrometer is easier. With a value of $h = 10$ mm, the sensors are far enough from the magnets to assure they can be placed there without major problems. For all further analysis and simulations the parameter is fixed to this value.

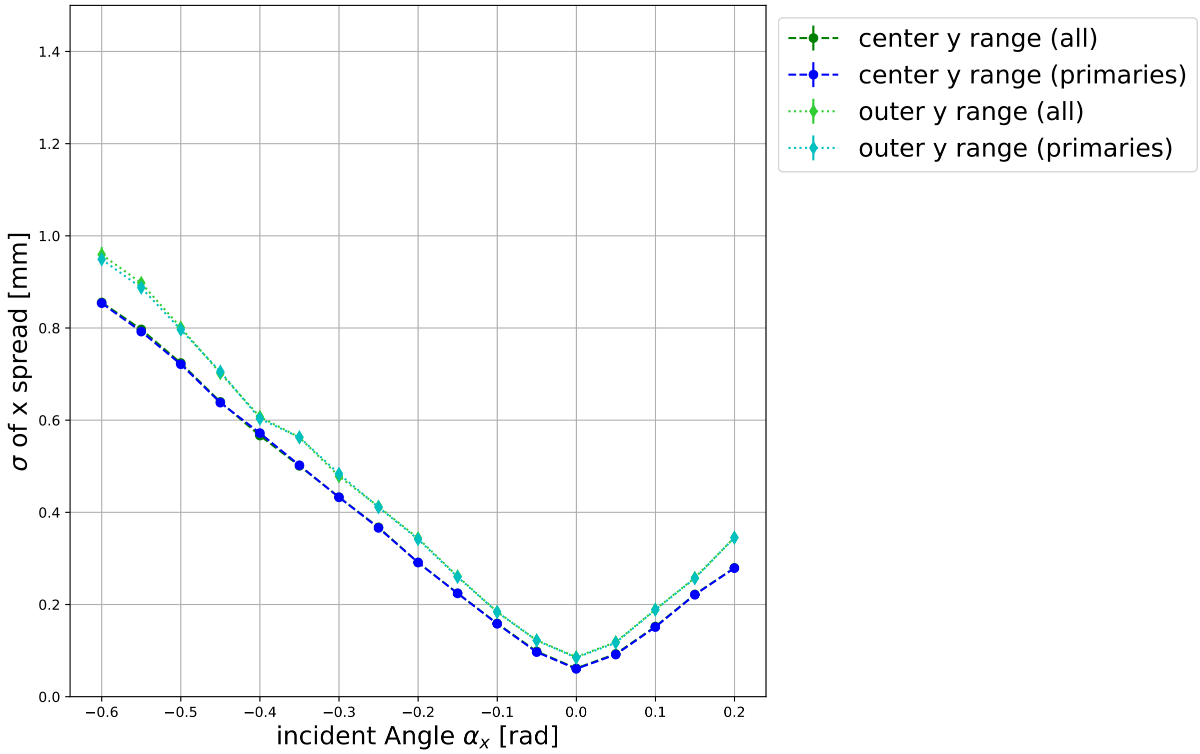

Figure 4.9: Scan of the incident angle α_x for the configuration with a distance h of 10 mm, a gap size of 17 mm between the magnet poles and a wedge angle of 0.3 rad. The x spread at the DUT is determined for the configurations with different incident angles α_x and for both the hits at the DUT in the center y range and in the outer y range. The spreads are obtained from the x-position distributions that include the contribution through secondary hits (*green* curves) and from the distribution solely over hits left by primaries (*blue* curves). The illustrated errors solely result from the errors of the fits to the simulated data. The accuracy of the illustrated x spread values and their errors is improved by the repeated fitting for shifted bin means in the histograms as shown in fig. 4.8 .

Scan of the gap size between the magnet poles

The last scan is done to decide on a gap size between the magnet poles. Within a single scan, the wedge angle is fixed again. But it is iterated for a number of different wedge angles to also see, if the gap size and the wedge angle correlate. The incident angles for the different configurations of the scan points are set to the respective optimum incident angles from the first scan again. From the results of this scan in fig. 4.11 the gap size does not seem to influence the x spread much. For all wedge angles, the curve is rather flat. For that reason, the choice of the gap size does not need to be made based on the Δx resolution. It is discussed further in section 4.3.

To analyze the dependence of the Δx resolution on the different scan parameters on a larger scale, the scan ranges were chosen rather big as can be seen in the mentioned figures 4.9, 4.10 and 4.11. Because the scans are done in discrete steps, an error for the chosen setup parameters

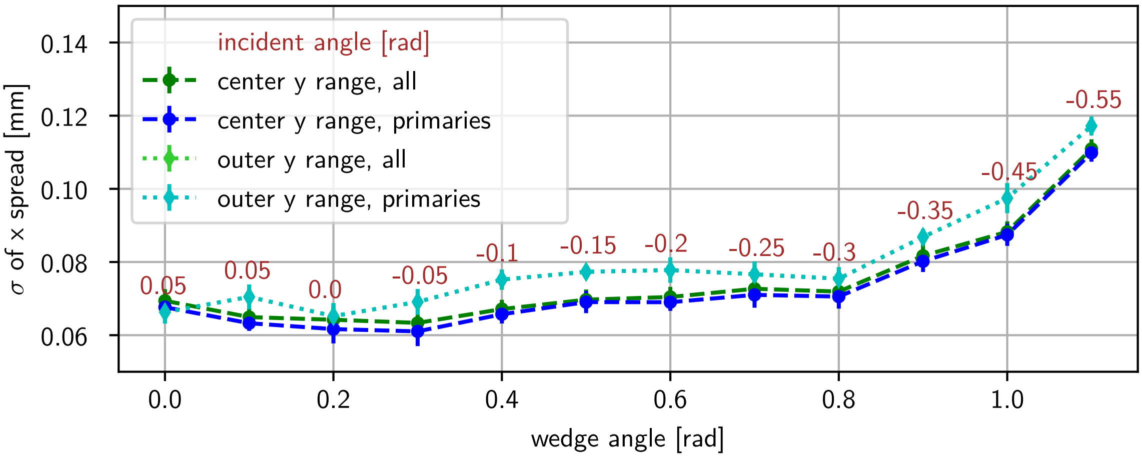

(a) gap size: 3 mm

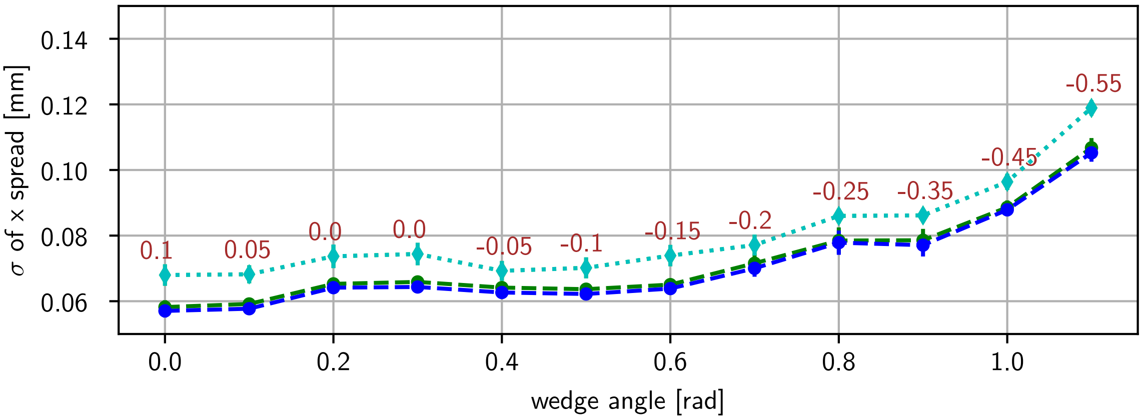

(b) gap size: 10 mm

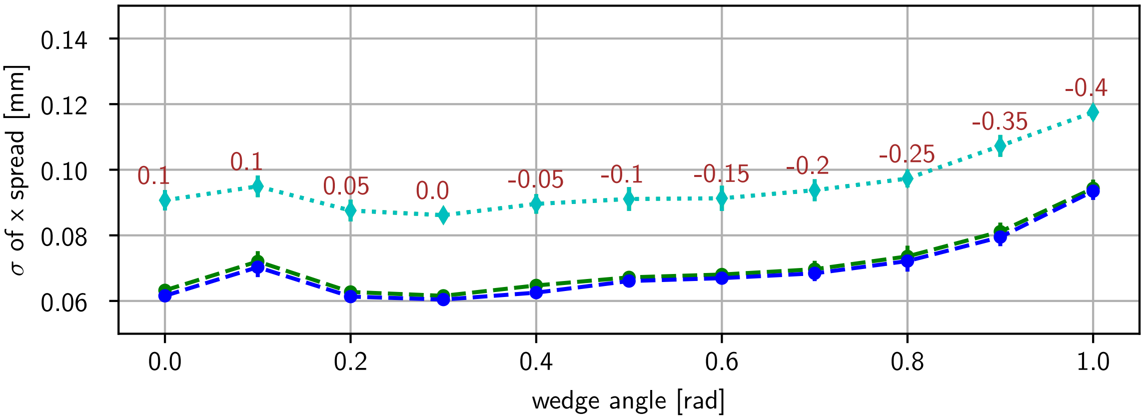

(c) gap size: 17 mm

Figure 4.10: Scan of the wedge angle for the configuration with a distance h of 10 mm, different gap sizes between the magnet poles and the respective optimal incident angles. The scan points are obtained in the same manner as for the previous scan in fig. 4.9.

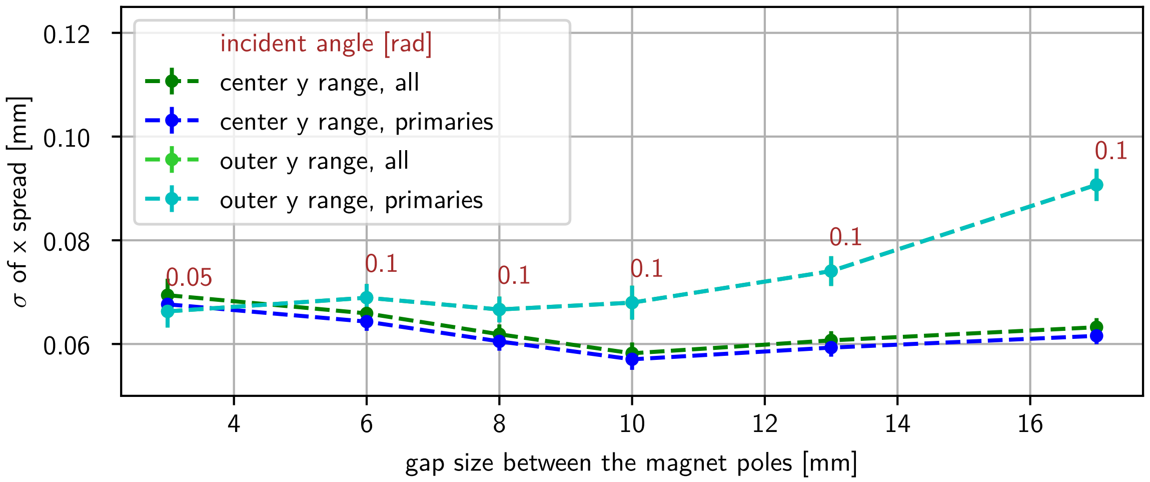

(a) wedge angle: 0 rad

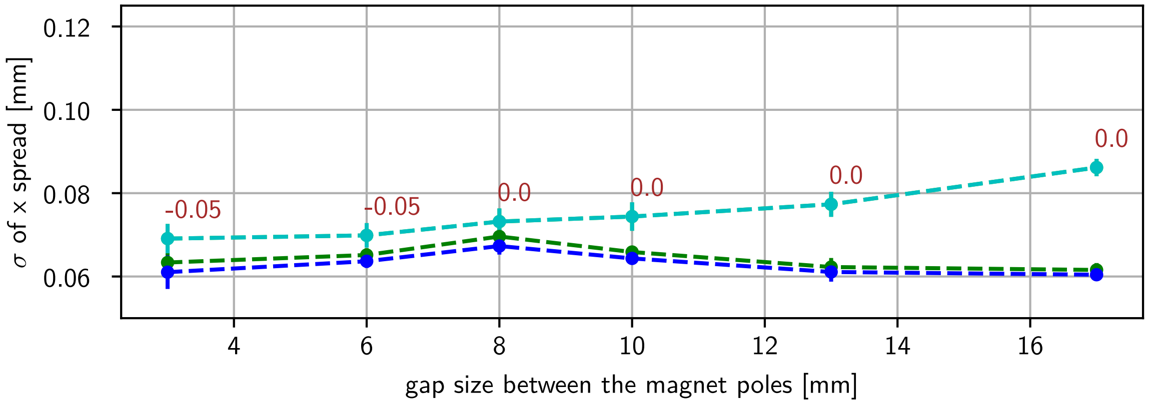

(b) wedge angle: 0.3 rad

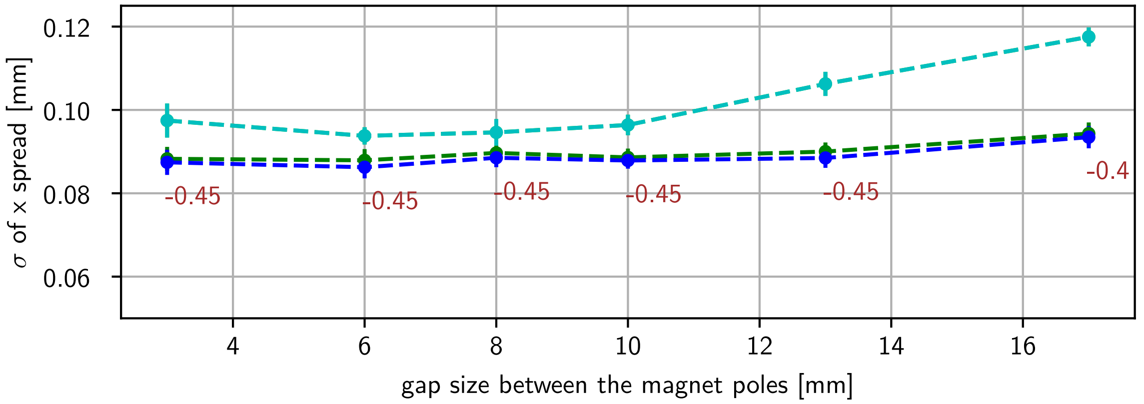

(c) wedge angle: 1.0 rad

Figure 4.11: Scan of the gap size between the magnet poles for the configuration with a distance h of 10 mm, different wedge angles and the respective optimal incident angles. The procedure to obtain the scan points is the same as in fig. 4.11 again.

– especially for the optimum incident angle α_x – based on the scan range and number of scan points is introduced. The number of scan points was chosen by considering the duration of running the simulation and keeping in mind that for each new combination of setup parameters the simulation has to be run. The total number of runs is given by multiplying the number of values of the different parameters with each other. The procedure could be optimized by clever dynamic adaption of parameters instead of linear space. With this, more scan points in the region of the optimal parameters could be taken which might reduce this error.

4.1.3 Limiting Factors

In order to find out if and how the momentum resolution can further be improved, it is investigated which factors contribute to the resolution the most. The impact of the pixel resolution of the sensors and the impact of the particle's interaction with matter in the experimental setup are considered separately. For the measurement of the incident angle α_x, the distance between the sensor layers L0 and L1 is already chosen with eq. (4.3) such that the pixel resolution does not limit the measurement. To see which effect influences the Δx measurement more, the x spreads at the DUT are investigated again.

To be able to look at the impact of the particle's interaction with matter exclusively, the x spread of the measured parameters can be obtained from the exactly simulated hit positions instead of the actual pixel positions, in which the hit is detected as done and explained in the previous section for the focus scan. The result of the focus scan shows that with optimal setup parameters a minimum x spread of $\sim 0.06\,\mathrm{mm}$ can be achieved.

The error of the x-positions at the DUT that results solely from the pixel resolution is directly given by the pixel resolution itself, which can be estimated with:

$$\sigma_t = \frac{\text{pixel width}}{\sqrt{12}} \tag{4.6}$$

With a pixel width of $80\,\mu\mathrm{m}$ for the used sensors, this results in an x spread of $\sim 0.023\,\mu\mathrm{m}$. As the multiple scattering error of the Δx measurement and the error from the pixel resolution are independent of each other, this shows that the Δx measurement is also not limited by the pixel resolution.

Since both the α_x and the Δx measurement are limited by the multiple scattering, the limiting factor of the momentum resolution is the multiple scattering, as well. In order to improve the momentum resolution, new ways to reduce the multiple scattering effect have to be found.

4.1.4 Impact of different Materials

All simulations discussed so far were done with the experimental setup in vacuum. The setup was examined via simulations for two other mediums, namely, helium and air. Helium has a radiation length of 5.671×10^5 cm [12], whereas air has a radiation length of 3.039×10^4 cm [12].

For these radiation lengths, the electrons are scattered more along their track compared two the case of the experimental setup being in vacuum, so that the influence of the multiple scattering on the momentum resolution increases. To see how much the momentum resolution is influenced, separate runs of the simulation with the world material set to helium and then to air are done. The x spreads that are obtained from these runs in the same manner as before, are compared to the previously determined x spread with the setup in vacuum in fig. 4.12. This is done for an example configuration. For other configurations, the measurements are impaired similarly by a different material choice. All conclusions drawn below apply for other configurations, as well.

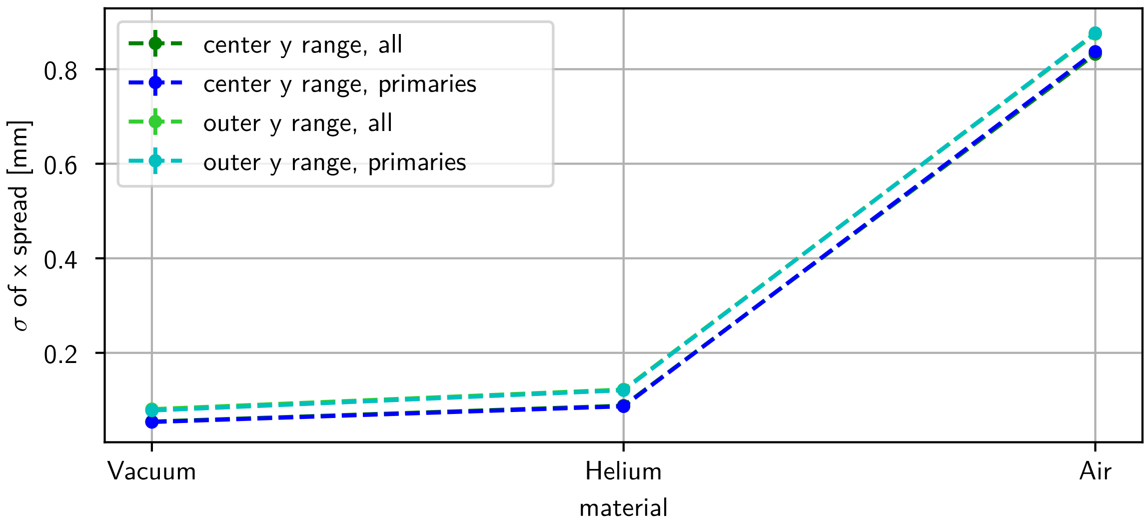

Figure 4.12: x spread at the DUT for different materials and for the configuration with a distance h of 10 mm, a gap size of 17 mm between the magnet poles, a wedge angle of 0.3 rad and an incident angle of 0 rad.

It can be seen that the use of helium instead of vacuum has little impact on the Δx measurement. It is not out of question to use helium, if the construction of the spectrometer is considerably easier in that case, which is to be expected. For air, however, the x spread increases by an entire order of magnitude. Therefore, air should not be chosen as the surrounding material in the setup.

4.1.5 Results

To estimate the achievable resolution of the spectrometer, the momentum resolution and the energy resolution is determined for the simulated data set with the homogeneous magnetic field model and the respective reconstruction as described in section 4.1.1. From the width of the peak in the momentum distribution of a single spectrometer arm shown in fig. 4.1, the momentum resolution Δp_i is expected to be $\sim 14.8\,\mathrm{keV/c}$. In theory, the energy loss resolution is therefore estimated as

$$\Delta p_{loss} = \sqrt{2} \cdot \Delta p_i = 20.2\,\mathrm{keV/c}.$$

The simulation showed, however, that the momentum resolution of the second spectrometer arm is worse than the mentioned one for the first arm. This is explained with more multiple scattering in the second arm. In addition to that, the actual momentum loss along the track until the second momentum measurement can vary a bit for particles of different events, such that the true momentum of the particles in the second spectrometer arm can already differ a bit more than the true momentum in the first spectrometer arm. That means that the individual momentum measurements for the different events are not necessarily much less precise, but the momentum distribution over all events is still wider. This is also reflected in the energy loss distribution in fig. 4.3, with which the energy loss resolution is estimated as $\sim 24.8\,\mathrm{keV/c}$.

A more accurate estimate of the spectrometer's resolution can be achieved when the inhomogeneity of the magnetic field is considered in the simulation and in the reconstruction. Because the respective track reconstruction is not implemented in the project, it is not known which exact resolution can be achieved with it. However, the truth information of the simulation can be used to obtain a momentum distribution of the simulated measurement and thus also an estimate of the momentum resolution. It is to be noted, that the accuracy and precision of the reconstruction with geantinos in the simulation as described in section 3.5 might differ from the accuracy of the obtained momentum distribution that is described in the following paragraph.

The momentum is assumed to have a contribution with linear dependency on the measured distance Δx_i, which is then corrected by a term c_i that depends on the measured inclination angle α_x.

$$p_i = A\left(\Delta x_i\left(1 + c_i\right)\right) \tag{4.7}$$

To determine the necessary corrections, the dependency of the Δx_i values on the α_x values is investigated. For that purpose the means of all Δx_i values that belong to a specific α_x value are plotted against these α_x values in fig. 4.13a. The true initial angle α_x in the used configuration is 0 rad. The measured values of the inclination angle are expected to be centered around this value, which is not the case. This might be a result from the reconstruction of α_x via the homogeneous field approximation. As the stray field reaches into the region where the sensor layers are positioned, the electron's track already bends instead of following a straight line in these regions. This causes the electron to hit layer L1 at bigger x-coordinates and layer L6 at smaller ones such that an offset of the reconstructed α_x values in comparison to the true initial α_x values can be seen. For the purpose of the following momentum reconstruction, this issue can be overlooked. That is, because the reconstruction only requires reconstructed incident angles of the same value to have the same true initial inclination angle regardless of it being the correct value or not.

Like for the focus scan, only the Δx_i values of events that are accepted by the in section 4.1.2 described event filter based on the range of the y-positions of the hits at the DUT are used. Here, only the center y range is accepted. Additionally, obvious outliers with much smaller Δx_i values than the rest are excluded again as done for the fit range in the momentum distribution for the homogeneous case. Due to the readout of hits with the pixel sensors, the measured α_x values are disrcretised already. With the pixel size of 80 µm, the obtained α_x range, which results from the multiple scattering, and a total number of 10000 events, there are multiple data points for most of the α_x values. To get more reliable values for the Δx_i means, the requirement was made that at least ten measurement points for a certain incident angle α_x exist to use the respective Δx_i mean in the plot in fig. 4.13a.

The proportionality constant A for the linear contribution of the Δx_i is obtained from the true initial momentum $p_{true} = 53\,\mathrm{keV/c}$ and the maximum Δx value, which is used as the reference value Δx_{ref}.

$$A = \frac{p_{true}}{\Delta x_{ref}} \tag{4.8}$$

The correction has to transform the measured value Δx_i to this reference value Δx_{ref} such that the momentum can be calculated by simply multiplying the result with the proportionality constant A. Therefore, c_i is defined in the following way.

$$c_i = \frac{\Delta x_{ref}}{\overline{\Delta x_i}} - 1, \tag{4.9}$$

where $\overline{\Delta x_i}$ is the mean of all Δx_i values belonging to the same α_x value. Ideally, the fraction $\frac{\Delta x_i}{\overline{\Delta x_i}}$ is close to one so that $\Delta x_i\,(1 + c_i) \approx \Delta x_{ref}$ is given. Using this correction, the reconstructed momentum becomes rather independent of the measured angle as can be seen in fig. 4.13b. The momentum loss is calculated the same way as for the homogeneous case, i.e. using eq. (3.10). The resulting momentum distribution and the momentum loss distribution are depicted in fig. 4.14. The resolutions are obtained from these distributions in the same manner as for the homogeneous case. The estimated values are $\sim 10.6\,\mathrm{keV/c}$ for the momentum resolution in the first spectrometer arm and $\sim 47.9\,\mathrm{keV/c}$ for the momentum loss resolution.

4.2 Purity

The purity of the spectrometer is defined as the number of reconstructed primaries divided by the total number of reconstructed tracks. With the setup of the double arm spectrometer, secondary particles do not hit all layers. Most of the produced secondaries are electrons. Other than that,

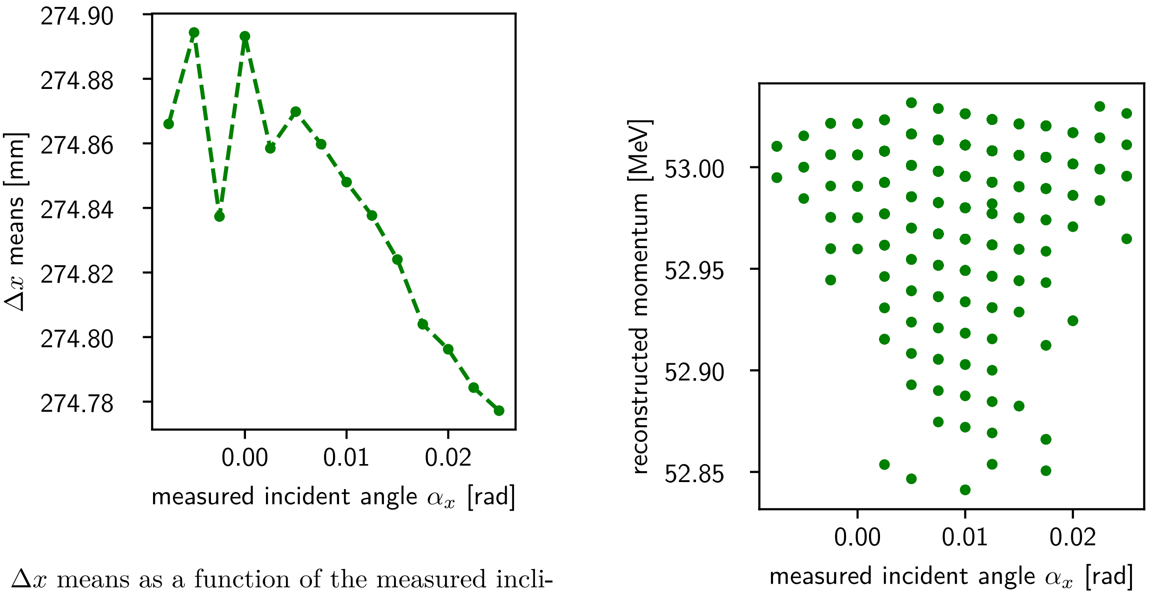

(a) Δx means as a function of the measured inclination angles α_x. For each event, Δx_i and α_x is determined for all tracks, including the ones with hits of secondaries, using the hit pixel positions. The y range filter is applied to only accept tracks of the center y range and Δx_i outliers are excluded by requiring the Δx_i values to lie in the range ± 0.8 mm around the mean of all reconstructed Δx_i. Δx_i values passing these filters, are assigned to the corresponding α_x of the respective track. If at least 10 measured Δx_i belong to the same α_x, the mean $\overline{\Delta x_i}$ of these Δx_i is calculated and added to the plot as the data point $(\alpha_x, \overline{\Delta x_i})$.

(b) reconstructed momentum as a function of the measured inclination angles α_x. The proportionality constant A is determined with the maximum of all measured Δx_i and the true momentum by eq. (4.8). With the mean values $\overline{\Delta x_i}$ for given α_x value depicted in fig. 4.13a, the momentum is reconstructed using eq. (4.7) and plotted against the measured α_x.

Figure 4.13: Dependencies on the incident angle for the configuration with a distance h of 10 mm, a gap size of 17 mm between the magnet poles, a wedge angle of 0.3 rad and an incident angle of 0 rad.

photons and very few positrons are produced. Photons are not detected by the sensors, so they do not leave traces. For both the secondary electron and the positron, the trajectory is very different from the trajectory of a primary electron without secondaries, as they only take a part of the primary electron's momentum and are therefore not deflected as much in the magnetic field. Also, the positron is deflected in the opposite direction of an electron. For these reasons, secondary particles are not reconstructed. It is, however, possible for a secondary particle to hit a single layer. In the track reconstruction, hits from secondaries are only differentiated from hits of primaries by the truth information from the simulation. Thus, such a hit of a secondary leads to an additional false combination of the hits in the other layers with this hit so that the purity decreases. The results of simulations with the inhomogeneous magnet model show that the purity is in the range above 0.8 for any configuration. As illustrated in fig. 4.15, it is rather

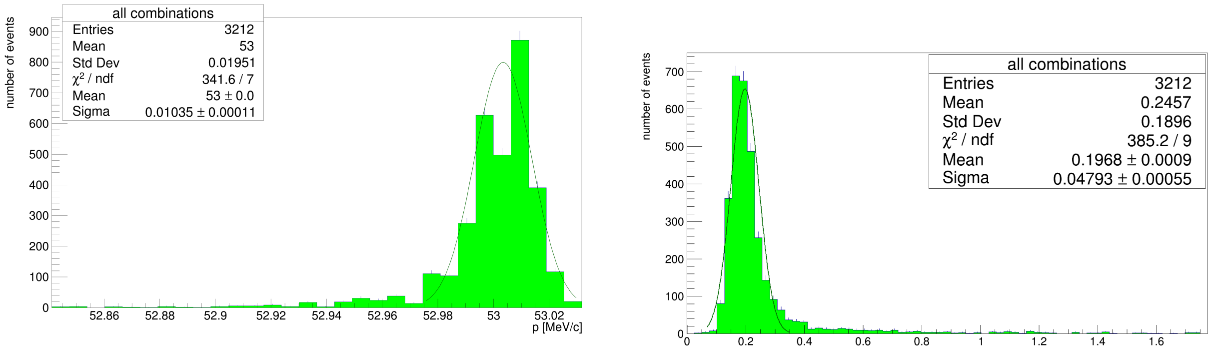

(a) Momentum distribution in the first spectrometer arm over 10000 events. The momentum is calculated with the preliminary momentum reconstruction for the inhomogeneous magnet model. The contribution of tracks obtained by a wrong combination of hits due to secondary hits is included. Only tracks with a center y range are accepted.

(b) Momentum loss distribution over 10000 events. The momentum loss is calculated as the difference between the values depicted in fig. 4.14a and the corresponding reconstructed momentum values of the second spectrometer arm.

Figure 4.14: Resolution for the configuration with a gap size of 17 mm between the magnet poles, a distance h of 10 mm, a wedge angle of 0.3 rad and an incident angle of 0 rad.

constant for different incident angles α_x, but increases for big gap sizes and for big wedge angles. With the event filter based on the y-position of the hits as described in section 4.1.1, the purity improves even to a value of 1.0 for all configurations. An improvement is expected, since the momentum of the primary is distributed to the produced particles, which is very likely to cause the secondary to have a different momentum direction and also gain some momentum in the y-direction. Because this filter impacts the purity this much, the purity should also be taken into account, if the limit for the accepted y range is reconsidered. For the choice of the setup parameters, however, it is more important to optimize the resolution and efficiency, as the purity is already in an acceptable range and can be improved with this filter for the y range.

4.3 Efficiency

The efficiency of the spectrometer is defined as the number of reconstructed primaries divided by the total number of generated primaries, i.e. the number of events. Only primaries leaving a hit in every sensor layer of the spectrometer are considered a "reconstructed" primary, as the energy loss can only be determined in this case. Instead of determining the energy loss in a device under test, which is the focus of this work, it is also possible to use the spectrometer as a tool for the energy measurement of a charged particle by exchanging the DUT with another 50 µm thick sensor layer. For this purpose, both of the momentum measurements in the individual spectrometer arms could be used for a more precise momentum measurement instead of subtracting the obtained

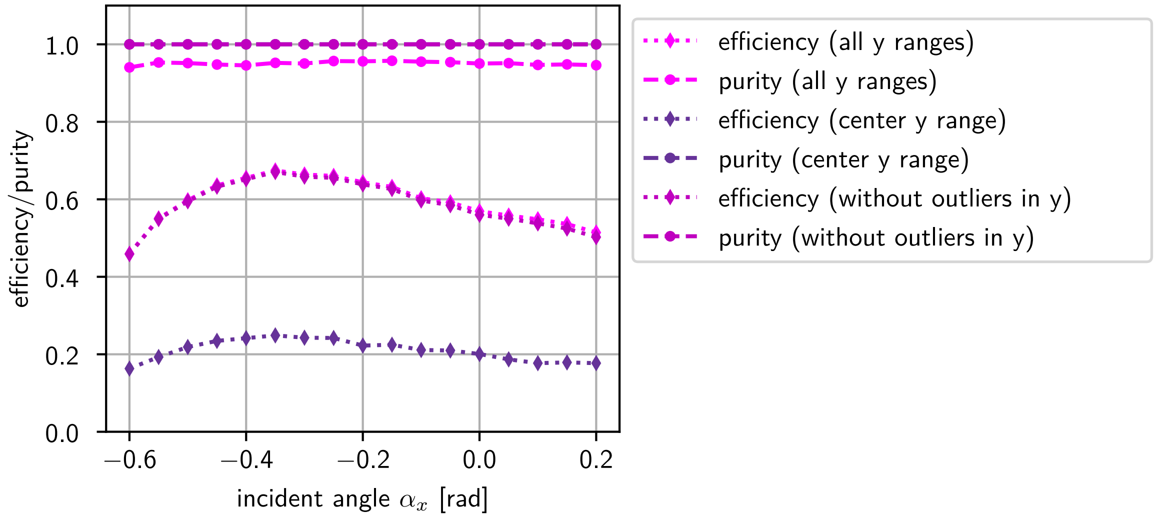

(a) gap size: 17 mm, wedge angle: 0 rad, different incident angles

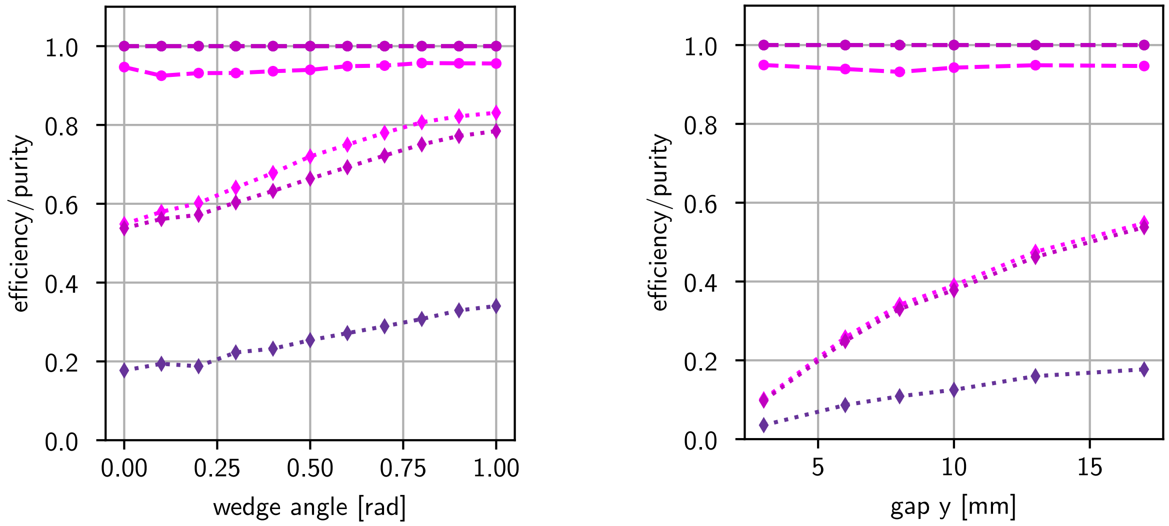

(b) gap size: 17 mm, optimal incident angles, different wedge angles

(c) wedge angle: 0 rad, optimal incident angles, different gap sizes

Figure 4.15: Efficiency and purity for different combinations of incident angles, wedge angles and gap sizes between the magnet poles. The distance h is fixed to 10 mm.

momenta values from each other. In this context, it would also be reasonable to analyze the efficiency of the two spectrometer arms separately, since the momentum measurement in the second arm is not strictly required then.

The main reason for a loss in efficiency is that the electrons gain a momentum component in the y-direction as a result of multiple scattering. As discussed in section 3.2.2, the problem with this is that the electrons then move towards the magnet poles. If they are not focused with respect to the angle α_y like in the setup with the wedged magnets or if the focusing in this setup is not strong enough, the electrons even reach the magnet poles and hit them. Due to the quite short radiation length of iron with a value of 1.757 cm [12], they are then stopped in most cases and do not reach the next sensor. This effect is reflected in the efficiency. For some setup configurations with the wedged magnet model (especially for big wedge angles), the simulation shows that most electrons hitting the magnet poles reach the poles just before they are supposed to exit the spectrometer arm, where the gap between the poles becomes smaller again. In these cases, there is not much material that the electron has to traverse before exiting the spectrometer arm and reaching the next sensor after all. Even with the small radiation length of iron, it could be observed that most of these electrons manage to traverse the magnet corner and hit the sensor at a big y-coordinate. For these configurations, the event filter for an accepted y range reduces the efficiency a lot, as less or none of such events are accepted. It is to note, that even though excluding these events reduces the efficiency, it also improves the resolution as the reconstructed momentum of most of these electrons deviates a lot from the true initial momentum. In fig. 4.15 the efficiency is plotted for different combinations of wedge angles and gap sizes between the magnet poles with the respective optimum incident angle α_x. The dependency of the efficiency on the incident angle is depicted in fig. 4.15a. The efficiency is shown for all reconstructed tracks, as well as for two different accepted y ranges of the event filter. One filter only keeps events with hits in the center y range, the other one keeps both the events with hits in the center y range and the outer y range. The curves indicate that both bigger wedge angles and bigger gap sizes improve the efficiency. For the choice of the setup parameters the efficiency is not the priority, because the electron beam in a measurement with the spectrometer has a high intensity and would produce enough events even for a small efficiency of the spectrometer. The disadvantage of wedged magnets compared to parallel magnets for the difficulty of the spectrometer's construction, especially for bigger wedge angles, outweighs the slight improvement of the efficiency. Still, it is reasonable to argue with the efficiency for the choice of a bigger gap size, as neither the resolution, nor the purity, is influenced a lot by the gap size.

Chapter 5

Conclusion

5.1 Conclusion and Summary

In this thesis, the energy loss measurement of charged particles with a possible design for a double arm spectrometer was investigated. The spectrometer is intended to be used for the characterization of tracking sensors. They can be calibrated with the measured energy loss and the resolution in energy loss measurements can be determined. For that, the spectrometer is required to do a very precise energy loss measurement. The energy loss is obtained from two momentum measurements, one in each of the spectrometer arms. The aim is to measure the momentum with a relative resolution of $\sim O(2 \times 10^{-4})$, which corresponds to $\sim 10\,\mathrm{keV/c}$ for electrons with an energy of $53\,\mathrm{MeV}$.

The spectrometer utilizes the correlation between the deflection of charged particles in magnetic fields with their momentum. Position and direction measurements with pixel sensors allow the reconstruction of the particle's track and momentum. Different designs of the spectrometer with small setup modifications were presented and their specific characteristics were discussed. Setups with a smaller number of sensor layers are preferred, as additional sensor material increases the energy loss and multiple scattering in the setup. The setup parameters specifying the layer positions, are required to fulfill different conditions for the distance and angle measurement to be in focus. These conditions, under which the focus is achieved, were calculated for an approximation with homogeneous magnetic field regions. Some designs have sensor layers inside the magnetic field region. This has the advantage that the momentum measurement is not directly impacted by the stray fields, as they are in a rather homogeneous field region. The placement of the sensor layers between the permanent magnets creates challenges for the spectrometer's construction and for the alignment of the individual components. It requires the gap between the magnet poles to have a minimum size of at least $2\,\mathrm{cm}$. In order not to have these challenges and restrictions, the other setups – the Double Edge Focusing Spectrometer Setup and the Simple Spectrometer Setup – were chosen for a more detailed analysis.

The analysis was done with different models for the description of the magnetic fields. For a first approximation, the field regions were assumed to be homogeneous. A more realistic model describes the magnetic field as a sum of fields produced by four individual magnet cuboids. The surrounding iron construction is not included in the model. The dimensions of the magnets in the model are adapted to take the redirection of some field lines by this iron construction partly into account. The wedge angle between the magnet edges of the magnet cuboids belonging to the same spectrometer arm was introduced as a new setup parameter. A wedge angle > 0 creates a field gradient along the defined z-direction in the setup which influences the focusing of the particles in the y-direction.

For the analysis, each event consisted of a single low energy electron entering the spectrometer setup with an initial total momentum of $53\,\mathrm{MeV/c}$. The sensors were assumed to be $50\,\mu\mathrm{m}$ thick silicon layers of the dimensions $2 \times 2\,\mathrm{cm}^2$. The Device Under Test (DUT) differs from the other sensors only in thickness and is chosen to be a $600\,\mu\mathrm{m}$ thick monolithic pixel sensor (as an example) in this thesis. A Monte Carlo simulation of the energy loss measurement with a double arm spectrometer was built as a C++ implementation using the software toolkit Geant4. The included features, e.g. the usage of physics models in Geant4, the readout of hits and the form of the output, were explained. A data set of 10000 events was produced for different setup configurations of the spectrometer and the described magnet models. The track reconstruction was implemented for the homogeneous magnet model where geometric relations for the setup parameters can be used.

A first estimate for the momentum resolution of $\sim 14.3\,\mathrm{keV/c}$ was made with the standard deviation of the momentum distribution in the first spectrometer arm obtained from the data set with the simulated homogeneous magnetic fields. The respective momentum loss resolution was therefore expected to be $\sim 20.1\,\mathrm{keV/c}$, but a derivation from the momentum loss distribution showed that the influences of increased multiple scattering in the second arm result in a new estimate of $\sim 24.8\,\mathrm{keV/c}$. An analysis for the minimization of the resolution was done for the realistic magnet models. An event filter for the accepted y range of hit positions at the DUT appeared to be beneficial. A scan over the setup parameters showed that the wedge angle does not have a big influence on the resolution unless chosen too big. For the incident angle α_x, there is a clear optimum value, if all other setup parameters are fixed. A comparison of the configurations with these optimum angles α_x for different distances h or different gap sizes between the magnet poles, suggested that the resolution is rather independent of both the parameter h and the gap size, as well. For further improvement of the resolution ways to reduce the multiple scattering effect need to be found, as this is the limiting factor for the resolution. As expected, the best resolution is given, if the experimental setup is surrounded by vacuum. The choice of helium instead of vacuum can be considered, if this simplifies the construction of the spectrometer crucially. Using air instead is not recommended, since the respective resolution of the position measurement at the DUT is worse by approximately an order of magnitude. For a configuration in vacuum that follows all the suggestions for the setup parameters given above, the momentum resolution of the first spectrometer arm was estimated to be $\sim 10.6\,\mathrm{keV/c}$ and the momentum loss resolution $\sim 47.9\,\mathrm{keV/c}$. The accuracy of these values is to be further investigated, as it does not use the same procedure for the track reconstruction which is intended to be used for the inhomogeneous magnet model.

Another part of the analysis concerns the achievable purity and efficiency of the spectrometer. A very good purity of $> 80\%$ was obtained for any configuration. The chosen limits for the accepted y range of the discussed filter for the y-positions at the DUT influences the purity a lot. For a small enough y range, it can even be improved to a value of 1.0 for all configurations. However, the smaller the accepted y range is, the smaller is the efficiency of the spectrometer. The efficiency was investigated with respect to the fully transported and reconstructed electrons. While not being a priority for the choice of setup parameters due to the high intensity of an electron beam for the spectrometer, the efficiency does improve for bigger wedge angles and gap sizes between the magnet poles.

5.2 Outlook

The aim of this thesis was to assess the feasibility of a high precision energy loss measurement with the setup of a double arm spectrometer. In this context, an estimate for the momentum loss resolution was given and the influences of different parameters on it were investigated. This estimate can still be improved by further analysis. The precision of the simulated data set can be increased by including the consideration of misalignment in the setup. Additionally, the initial momentum of the particle was assumed to be exactly the same in each event. It is more realistic to introduce an initial energy range of the particle which follows a Gaussian distribution. Some more details in the description of the experimental setup such as the inactive material of the sensors could be implemented. Also, the cuboids of the realistic magnet model were assumed to be very large in the y-direction to account for the surrounding iron construction. It could be considered to implement the iron construction itself in the simulation instead. The track reconstruction for the inhomogeneous magnet model is intended to be done with a numerical solution for the particle's momentum using an implementation with geantinos in the simulation, which might change the resulting resolution. So far the correlation between the x- and y-coordinates of the hit positions was used for an event filter. It could be investigated, if this information can instead be used for a correction of the reconstructed momentum. This might improve both the accuracy of the reconstructed momentum for accepted events and the efficiency, since the event filter can then likely be removed or at least the accepted range can be increased.

APPENDIX **A**

Appendix

Magnetic field of a cuboid

xz-plane

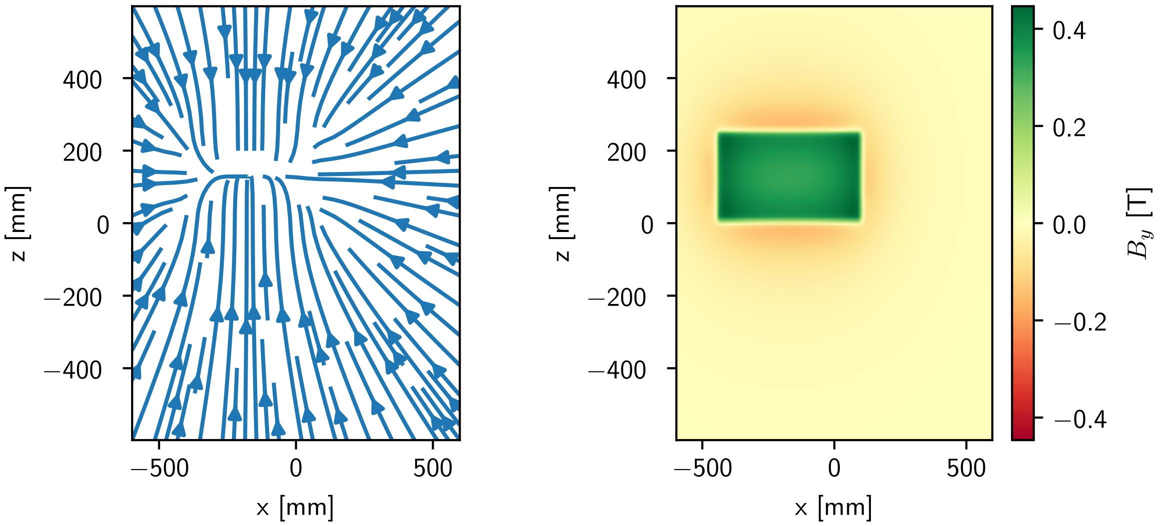

(a) magnetic field lines (b) map of the B_y component

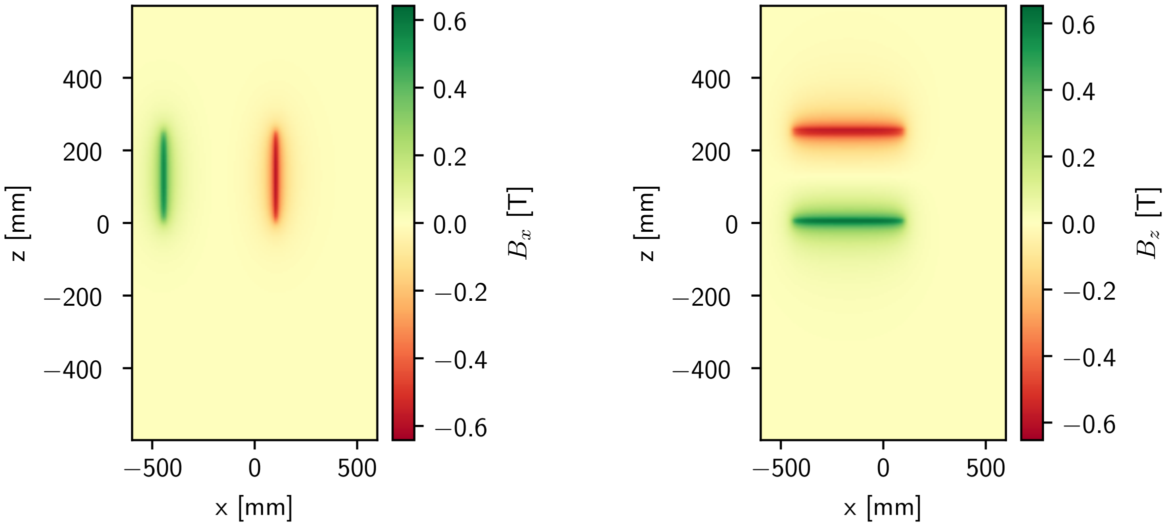

(c) map of the B_x component (d) map of the B_z component

Figure A.1: xz-plane of the field of a permanent magnet cuboid with a magnetic field in the y-direction. The magnetization of the cuboid corresponds to a magnetic field of 1.4 T. The cuboids dimensions are chosen to be 550 mm in the x-direction, 100 mm in the y-direction and 250 mm in the z-direction. As the gap between the two magnet cuboids in the spectrometer arm is small (a range of $3 - 17$ mm was investigated), the electron experiences the field in the gap at a small distance from the magnet cuboids. Therefore, the depicted planes are chosen to illustrate the field at a distance of 5 mm from the magnet face with regard to the y-direction.

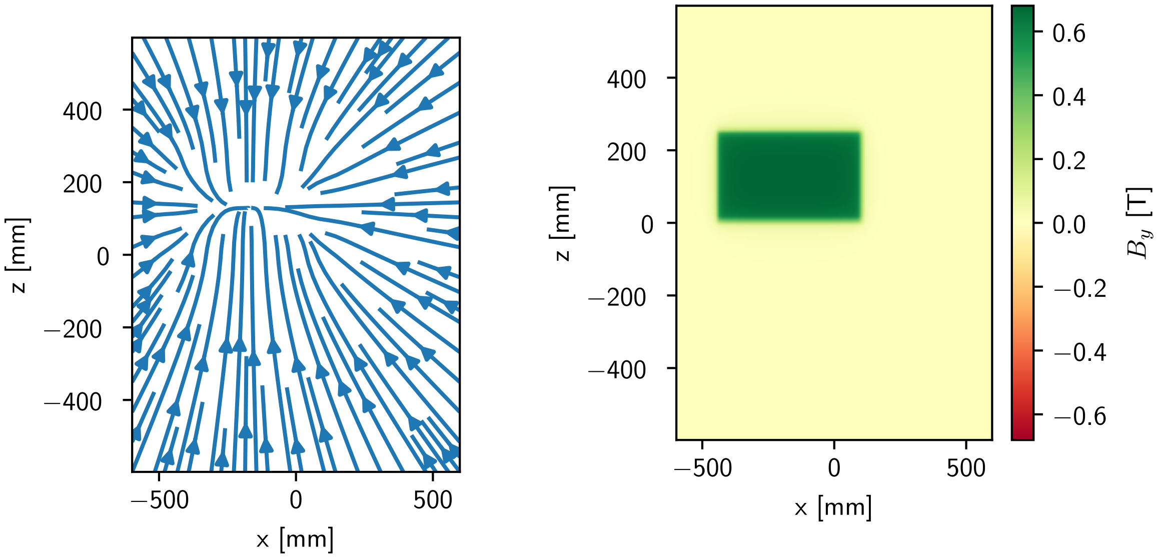

(a) magnetic field lines

(b) map of the B_y component. It can be seen that the choice of a large y-dimension of the cuboid reduces the stray fields compared to fig. A.1b.

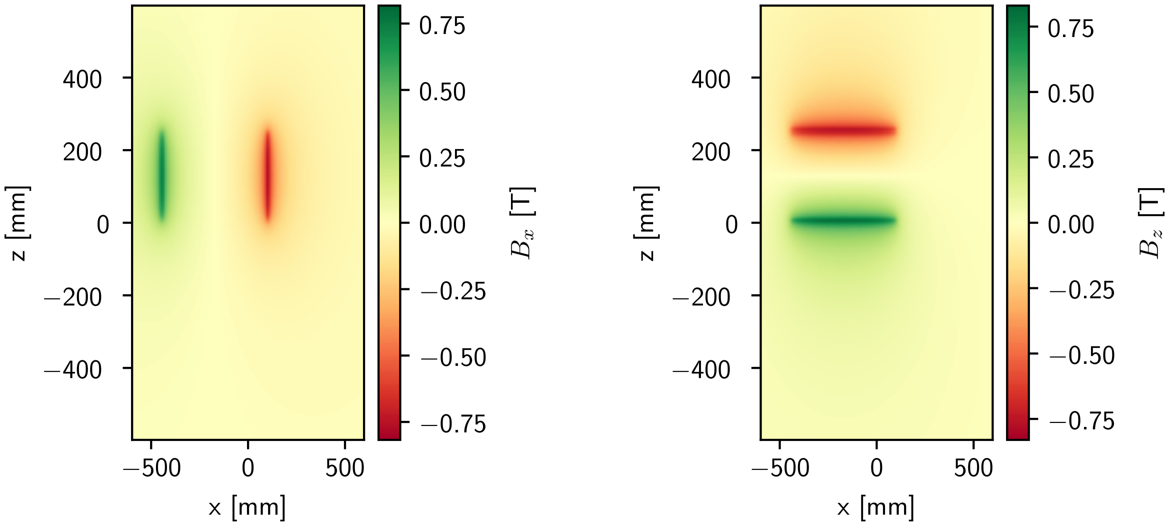

(c) map of the B_x component

(d) map of the B_z component

Figure A.2: xz-plane of the field of a permanent magnet cuboid with a magnetic field in the y-direction. The perspectives and all properties of the magnetic cuboid are chosen the same as in fig. A.1 except for the y-dimension of the cuboid, which is set to 2×10^{-7} mm, like it is done for the inhomogeneous magnet models of the spectrometer.

xy-plane

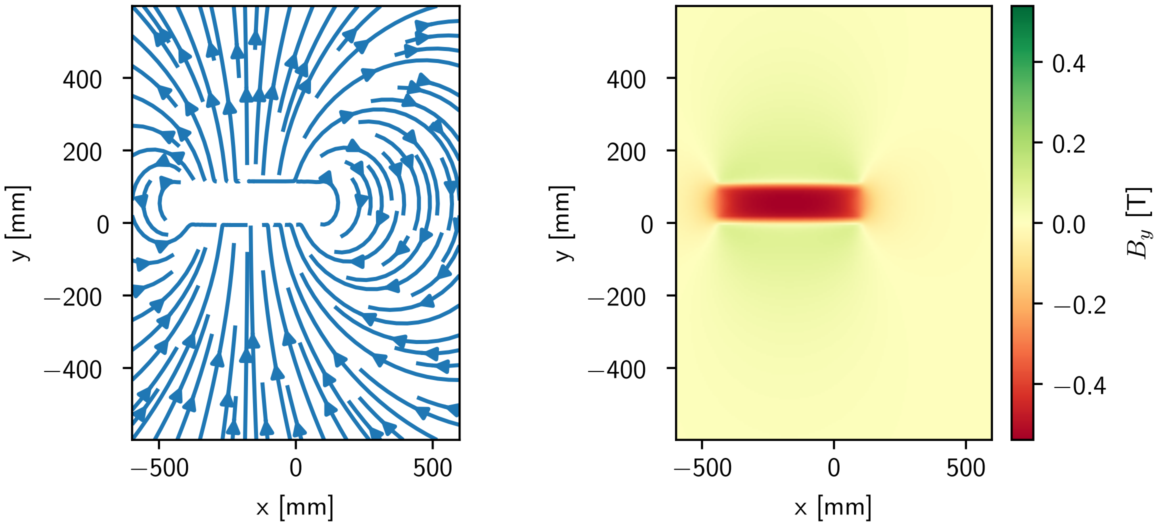

(a) magnetic field lines

(b) map of the B_y component

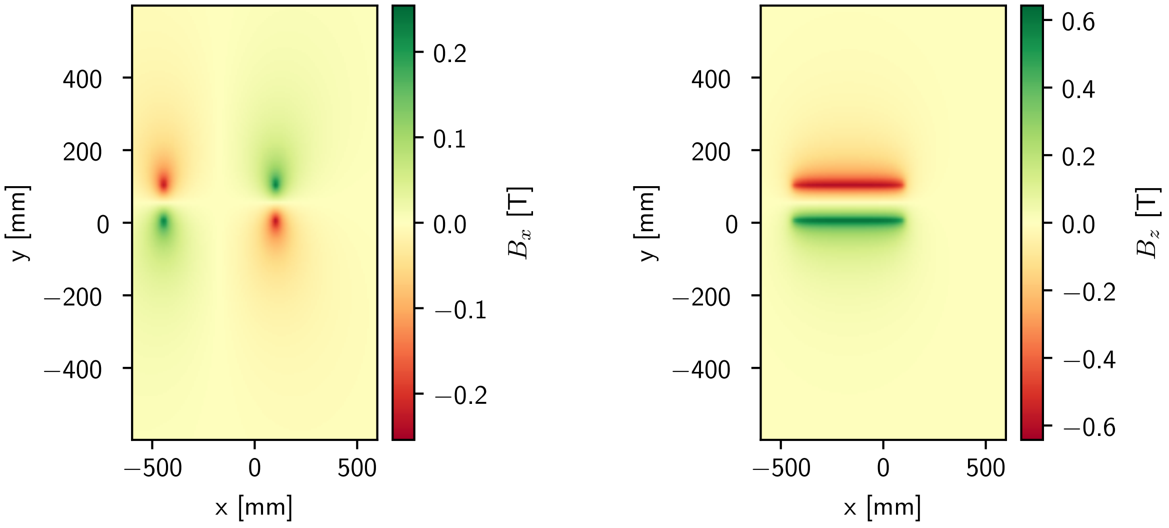

(c) map of the B_x component

(d) map of the B_z component

Figure A.3: xy-plane of the field of a permanent magnet cuboid with a magnetic field in the y-direction. The magnetization of the cuboid corresponds to a magnetic field of 1.4 T. The cuboids dimensions are chosen to be 550 mm in the x-direction, 100 mm in the y-direction and 250 mm in the z-direction. The depicted planes are chosen to illustrate the field at a distance of 5 mm from the magnet face with regard to the z-direction. In the spectrometer setup the sensor layers L1,L5 and the DUT are positioned at the same distance from the magnet construction.

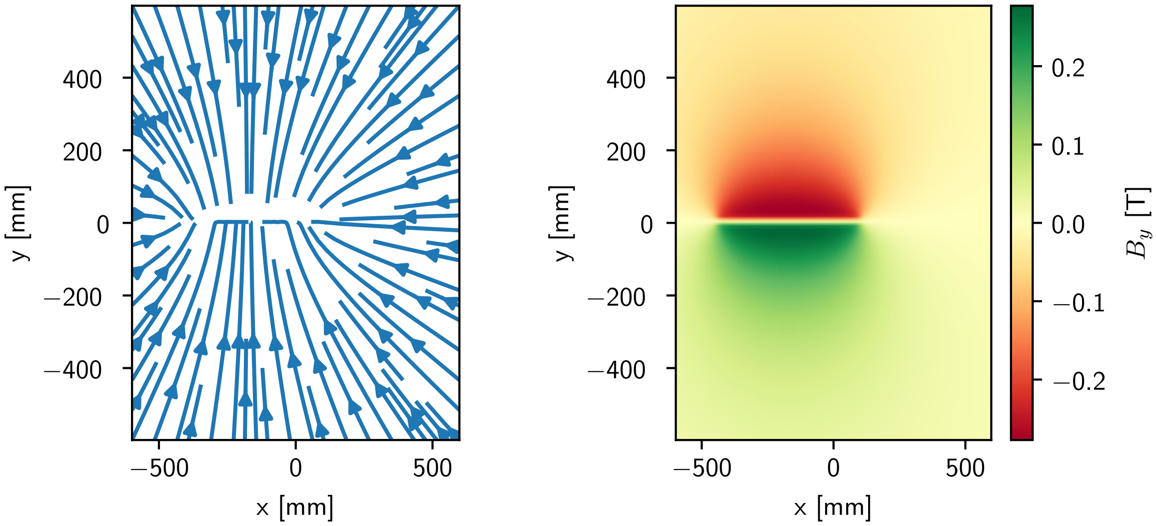

(a) magnetic field lines

(b) map of the B_y component

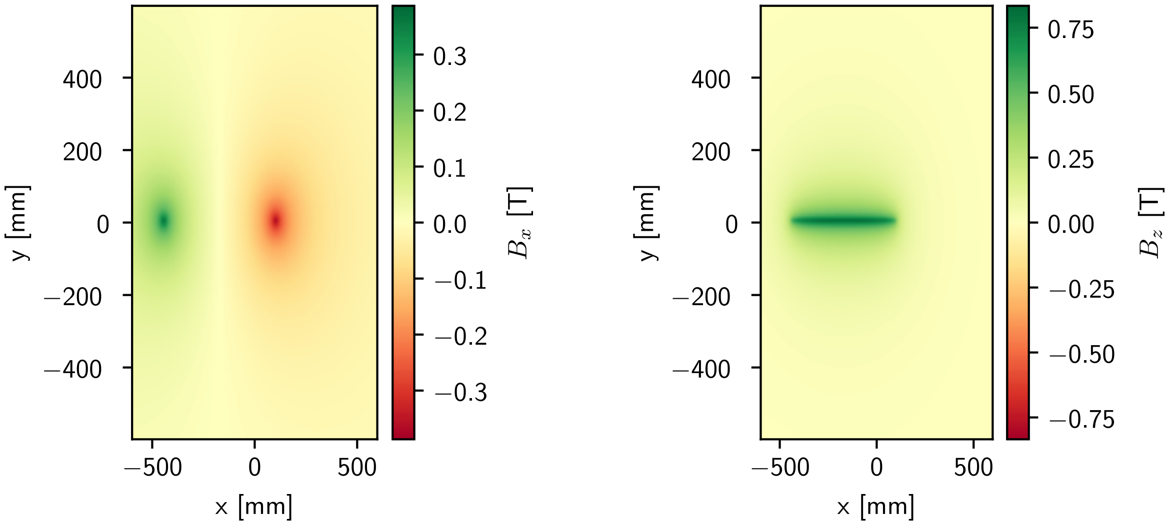

(c) map of the B_x component

(d) map of the B_z component

Figure A.4: xy-plane of the field of a permanent magnet cuboid with a magnetic field in the y-direction. The perspectives and all properties of the magnetic cuboid are chosen the same as in fig. A.3 except for the y-dimension of the cuboid, which is set to 2×10^{-7} mm, like it is done for the inhomogeneous magnet models of the spectrometer. A comparison, to the field maps in fig. A.5 shows that the field in the depicted region is not influenced by the magnet edges outside the shown region as much.

zy-plane

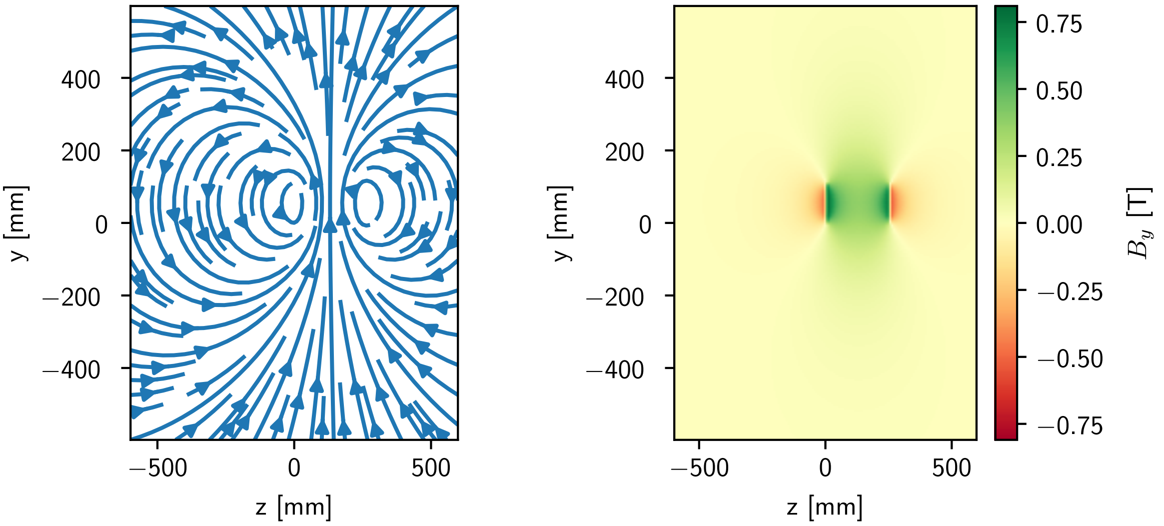

(a) magnetic field lines

(b) map of the B_y component

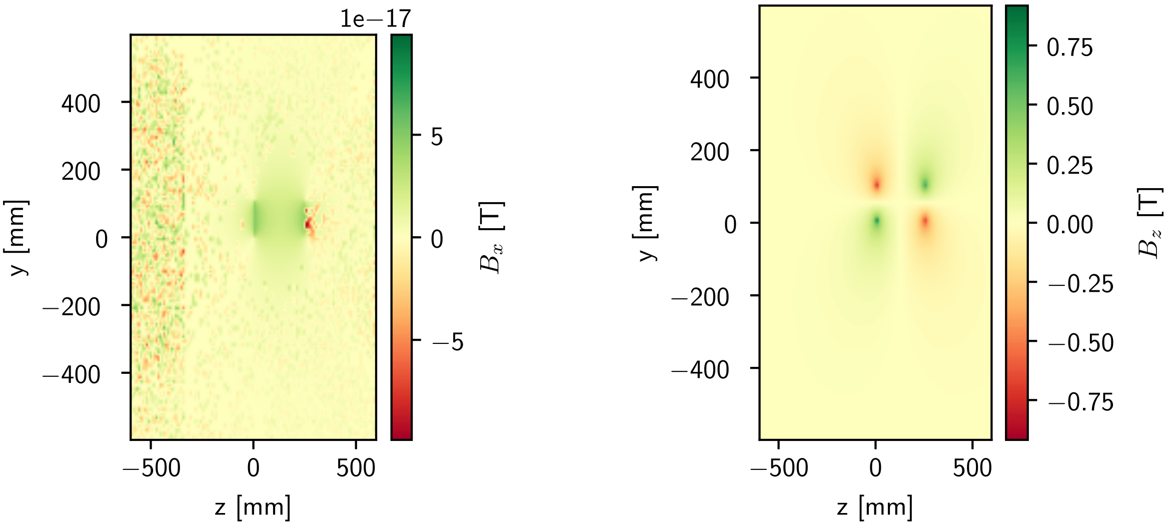

(c) map of the B_x component

(d) map of the B_z component

Figure A.5: zy-plane of the field of a permanent magnet cuboid with a magnetic field in the y-direction. The magnetization of the cuboid corresponds to a magnetic field of 1.4 T. The cuboids dimensions are chosen to be 550 mm in the x-direction, 100 mm in the y-direction and 250 mm in the z-direction. In the spectrometer setup, the strong magnetic field regions where the electron is desired to be deflected to do a turn, are at the same y-positions as the magnet cuboids of the respective spectrometer arm. Therefore, the depicted planes are chosen to go through the magnets. The x-position of the planes is chosen equal to the x-position of the cuboid's center.

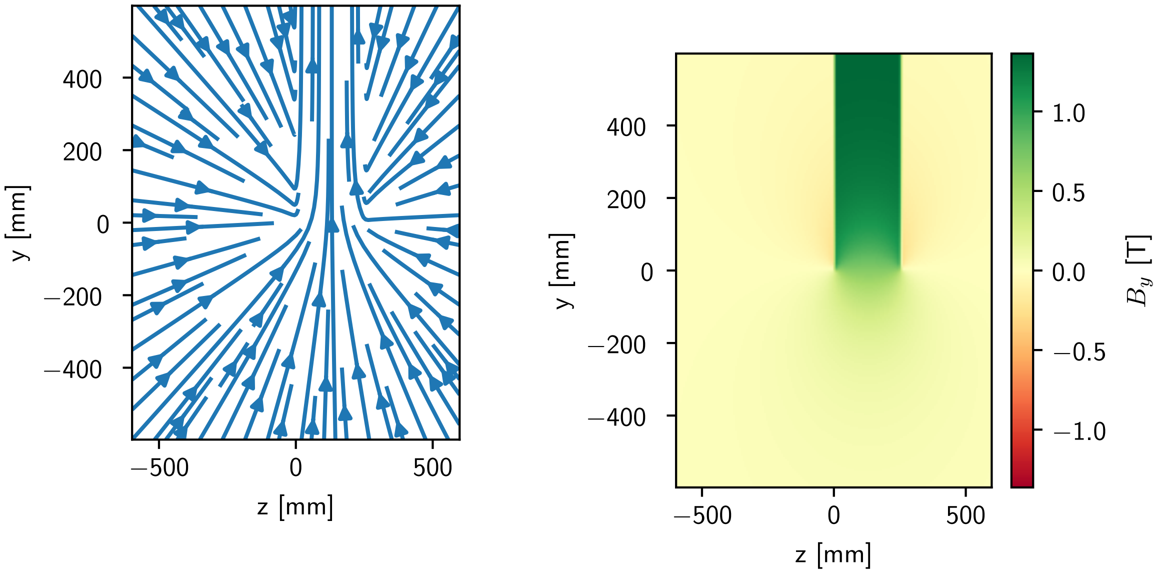

(a) magnetic field lines. The field lines in the depicted regions are not curved as much towards the upper edge of the magnet as for a magnet of smaller y-dimension.

(b) map of the B_y component

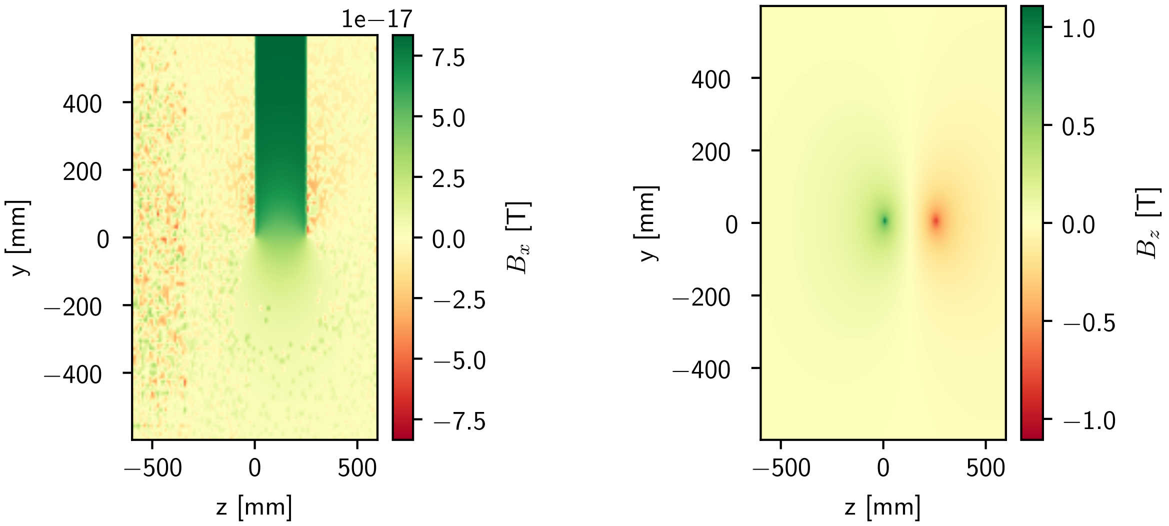

(c) map of the B_x component

(d) map of the B_z component

Figure A.6: zy-plane of the field of a permanent magnet cuboid with a magnetic field in the y-direction. The perspective and all properties of the magnetic cuboid are chosen the same as in fig. A.5 except for the y-dimension of the cuboid, which is set to 2×10^{-7} mm, like it is done for the inhomogeneous magnet models of the spectrometer.

Magnetic Field of a Double Arm Spectrometer in the Parallel Magnet Configuration

xz-plane

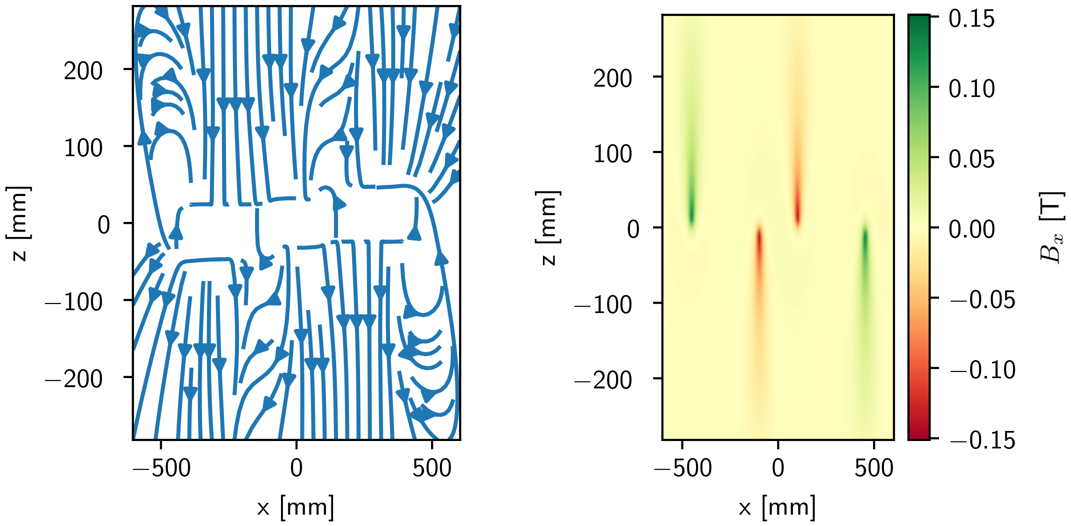

(a) magnetic field lines

(b) map of the B_x component

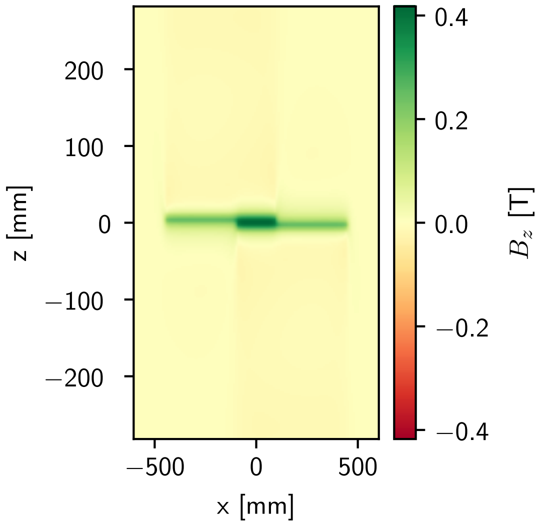

(c) map of the B_z component

Figure A.7: xz-plane of the magnetic field in the setup with parallel magnet cuboids and a gap size of 17 mm between the magnet poles. The planes are chosen to be inside the gap at y = 5 mm.

xy-plane

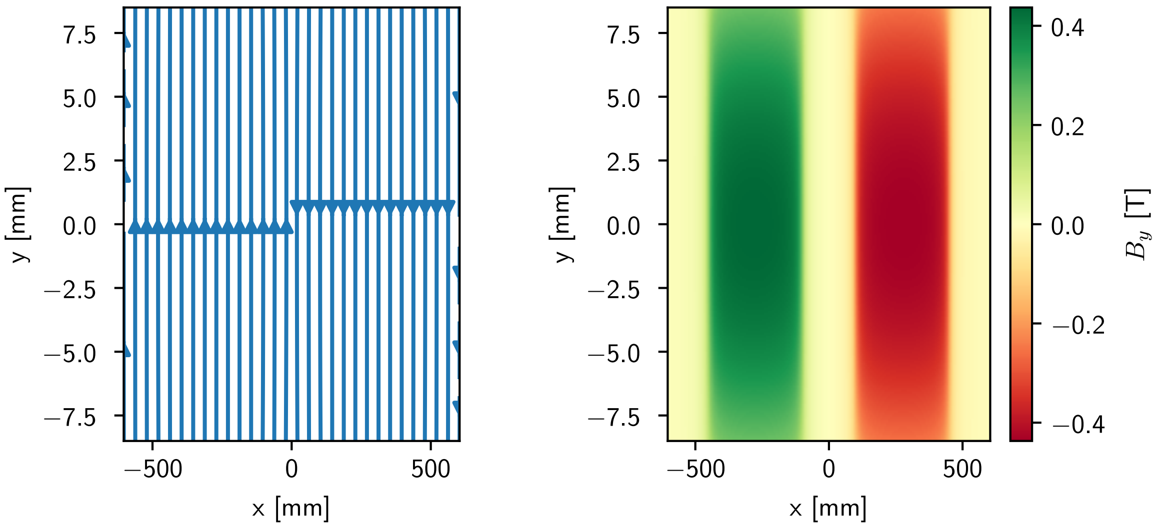

(a) magnetic field lines

(b) map of the B_y component

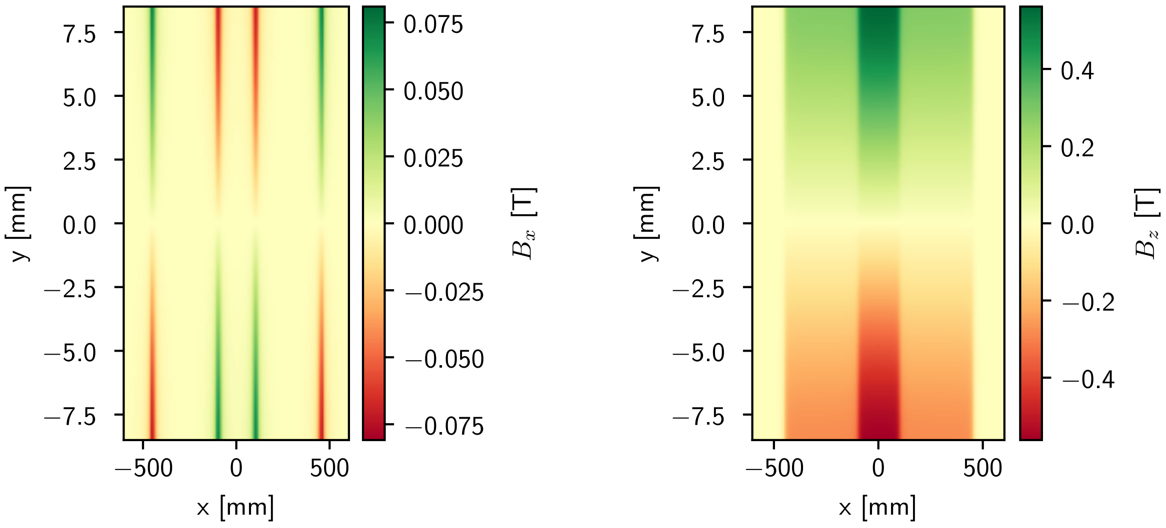

(c) map of the B_x component

(d) map of the B_z component

Figure A.8: xy-plane of the magnetic field in the setup with parallel magnet cuboids and a gap size of 17 mm between the magnet poles. The planes are chosen to depict the field at the z-position of the sensor layers L1, L5 and the DUT.

zy-plane

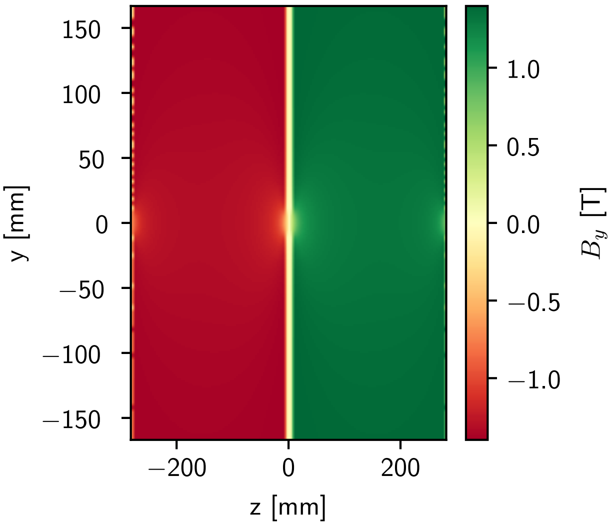

(a) map of the B_y component

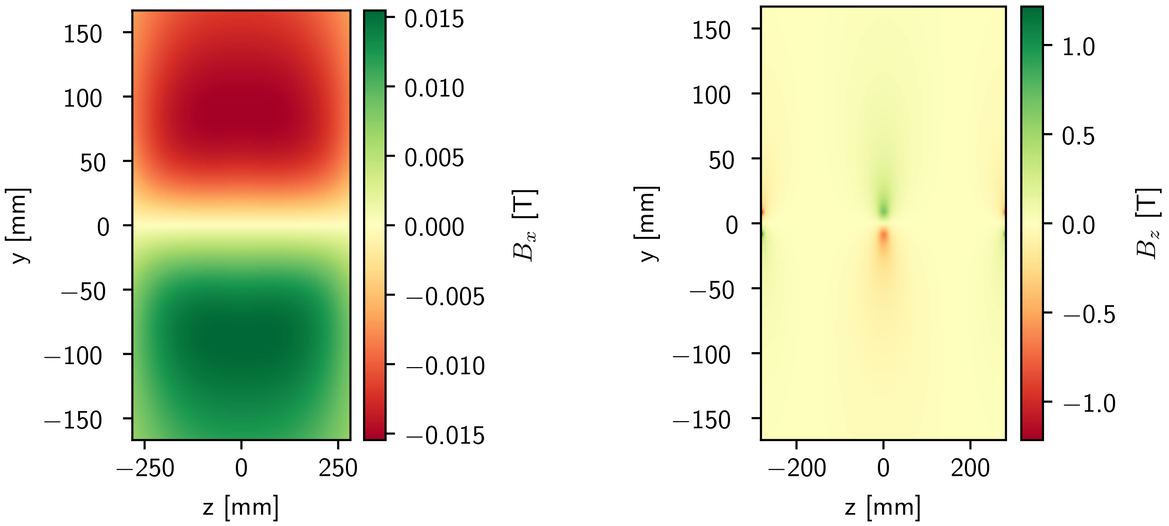

(b) map of the B_x component

(c) map of the B_z component

Figure A.9: zy-plane of the magnetic field in the setup with parallel magnet cuboids and a gap size of 17 mm between the magnet poles. The planes are chosen to go through the center of the DUT such that the field of both spectrometer arms is shown.

Magnetic Field of a Double Arm Spectrometer in the Wedge Magnet Configuration

xz-plane

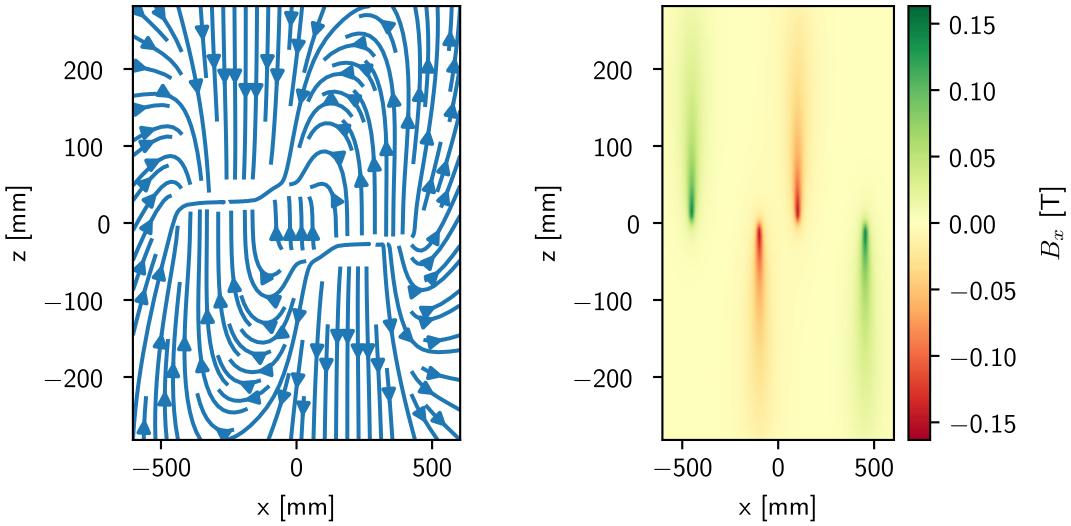

(a) magnetic field lines (b) map of the B_x component

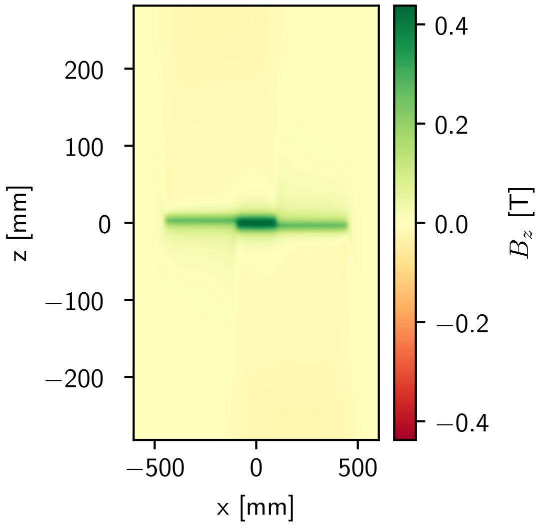

(c) map of the B_z component

Figure A.10: xz-plane of the magnetic field in the setup with wedged magnet cuboids with the gap size 17 mm between the magnet poles and a wedge angle of 0.3 rad inside the gap at y = 5 mm.

xy-plane

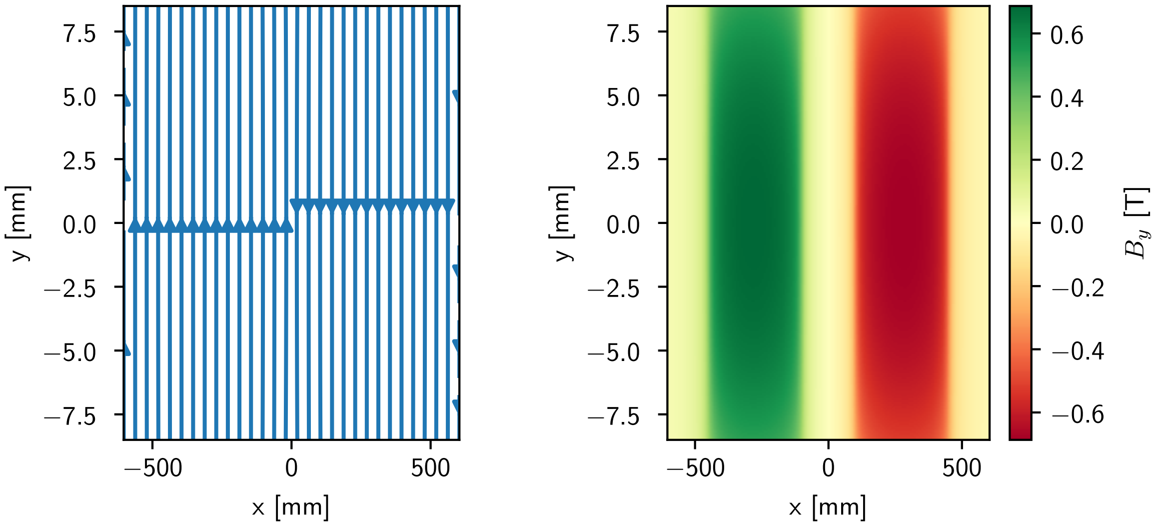

(a) magnetic field lines

(b) map of the B_y component

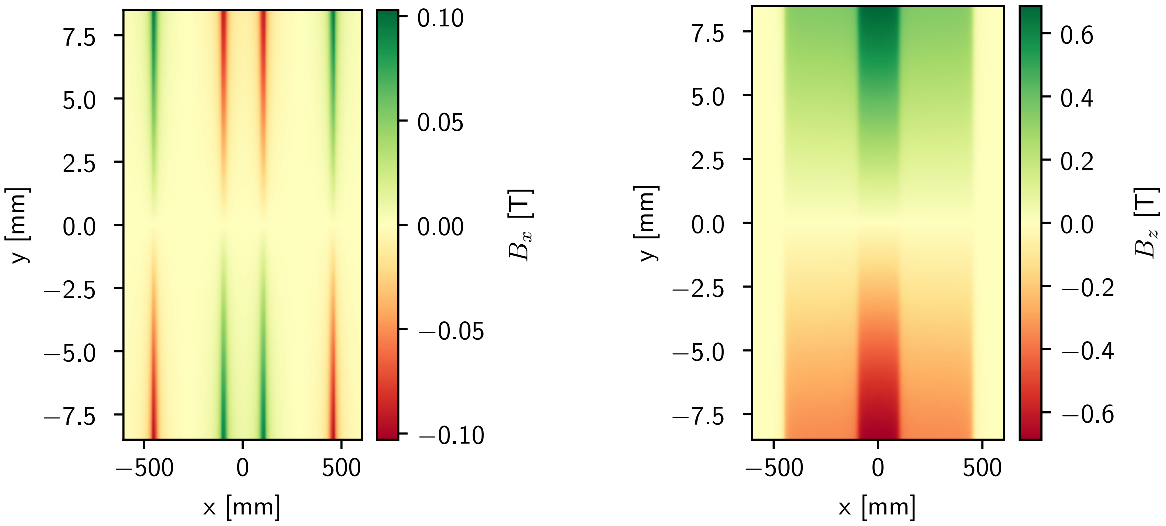

(c) map of the B_x component

(d) map of the B_z component

Figure A.11: xy-plane of the magnetic field in the setup with wedged magnet cuboids with the gap size 17 mm between the magnet poles and a wedge angle of 0.3 rad at the z-position of the sensor layers L1, L5 and the DUT.

zy-plane

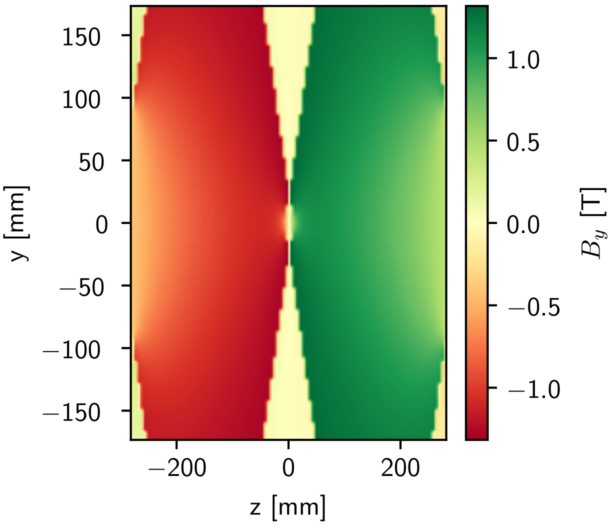

(a) map of the B_y component

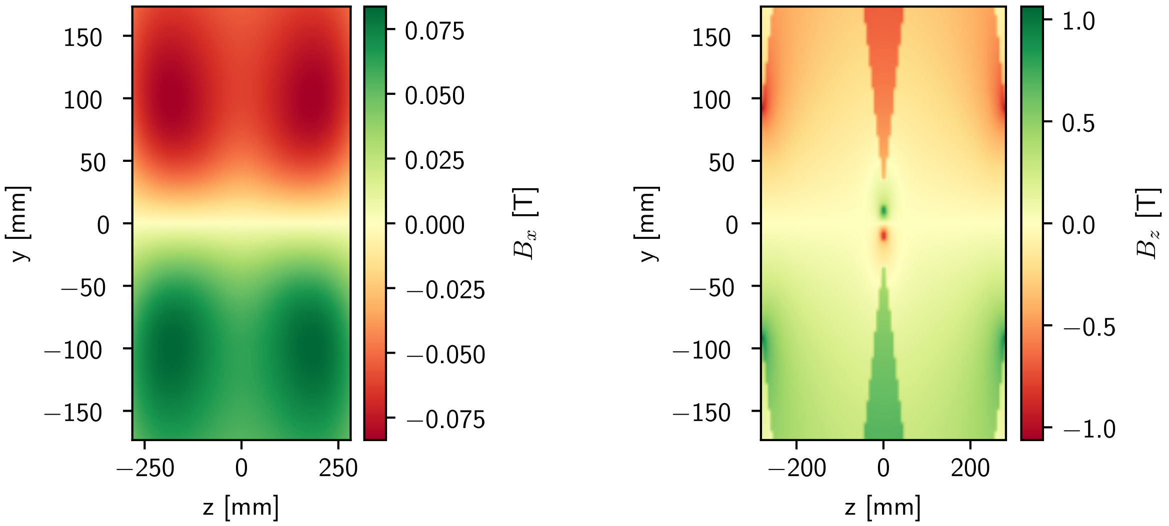

(b) map of the B_x component

(c) map of the B_z component

Figure A.12: zy-plane of the magnetic field in the setup with wedged magnet cuboids with the gap size 17 mm between the magnet poles and a wedge angle of 0.3 rad at the x-position of the DUT.

Bibliography

[1] S. Agostinelli et al. "Geant4—a simulation toolkit". In: *Nuclear Instruments and Methods in Physics Research Section A: Accelerators, Spectrometers, Detectors and Associated Equipment* 506.3 (2003), pp. 250–303. ISSN: 0168-9002. DOI: `https://doi.org/10.1016/S0168-9002(03)01368-8`. URL: `https://www.sciencedirect.com/science/article/pii/S0168900203013688`.

[2] M. Aiba et al. *Science Case for the new High-Intensity Muon Beams HIMB at PSI.* 2021. arXiv: `2111.05788 [hep-ex]`. URL: `https://arxiv.org/abs/2111.05788`.

[3] J. Allison et al. "Recent developments in Geant4". In: *Nuclear Instruments and Methods in Physics Research Section A: Accelerators, Spectrometers, Detectors and Associated Equipment* 835 (2016), pp. 186–225. ISSN: 0168-9002. DOI: `https://doi.org/10.1016/j.nima.2016.06.125`. URL: `https://www.sciencedirect.com/science/article/pii/S0168900216306957`.

[4] Heiko Augustin et al. "The MuPix sensor for the Mu3e experiment". In: *Nuclear Instruments and Methods in Physics Research Section A: Accelerators, Spectrometers, Detectors and Associated Equipment* 979 (2020), p. 164441. ISSN: 0168-9002. DOI: `https://doi.org/10.1016/j.nima.2020.164441`. URL: `https://www.sciencedirect.com/science/article/pii/S016890022030838X`.

[5] A. M. Baldini et al. "The design of the MEG II experiment: MEG II Collaboration". In: *The European Physical Journal C* 78.5 (May 2018). ISSN: 1434-6052. DOI: `10.1140/epjc/s10052-018-5845-6`. URL: `http://dx.doi.org/10.1140/epjc/s10052-018-5845-6`.

[6] H. A. Bethe. "Molière's Theory of Multiple Scattering". In: *Phys. Rev.* 89 (6 Mar. 1953), pp. 1256–1266. DOI: `10.1103/PhysRev.89.1256`. URL: `https://link.aps.org/doi/10.1103/PhysRev.89.1256`.

[7] *C++ Implementation of the Track Reconstruction for the Homogeneous Magnet Model.* URL: `https://gitlab.com/tamasigithub/compact_spectro/-/blob/Laura/spectroRec/src/Track.cc?ref_type=heads` (visited on 07/05/2024).

[8] L L Carter and E D Cashwell. "Particle-transport simulation with the Monte Carlo method". In: (Jan. 1975). DOI: `10.2172/4167844`. URL: `https://www.osti.gov/biblio/4167844`.

[9] MEG II Collaboration et al. *Operation and performance of MEG II detector.* 2024. arXiv: `2310.11902 [physics.ins-det]`. URL: `https://arxiv.org/abs/2310.11902`.

[10] "Final results of the MEG experiment". In: *Il Nuovo Cimento C* 39.4 (Dec. 2016), pp. 1–8. ISSN: 03905551, 03905551. DOI: `10.1393/ncc/i2016-16325-7`. URL: `https://doi.org/10.1393/ncc/i2016-16325-7`.

[11] Mary K. Gaillard, Paul D. Grannis, and Frank J. Sciulli. "The standard model of particle physics". In: *Rev. Mod. Phys.* 71 (2 Mar. 1999), S96–S111. DOI: `10.1103/RevModPhys.71.S96`. URL: `https://link.aps.org/doi/10.1103/RevModPhys.71.S96`.

[12] Particle Data Group et al. "Review of Particle Physics". In: *Progress of Theoretical and Experimental Physics* 2022.8 (Aug. 2022), p. 083C01. ISSN: 2050-3911. DOI: `10.1093/ptep/ptac097`. eprint: `https://academic.oup.com/ptep/article-pdf/2022/8/083C01/49175539/ptac097.pdf`. URL: `https://doi.org/10.1093/ptep/ptac097`.

[13] Frank Hinterberger. *Physik der Teilchenbeschleuniger und Ionenoptik.* Heidelberg: Springer Berlin, 2008. URL: `https://doi.org/10.1007/978-3-540-75282-0`.

[14] D. H. Jakubassa-Amundsen. *Advances in bremsstrahlung: a review.* 2021. arXiv: `2103.06034 [physics.atom-ph]`. URL: `https://arxiv.org/abs/2103.06034`.

[15] Yannick Klein, Leon Abelmann, and Han Gardeniers. *Influence of the distribution of the properties of permanent magnets on the field homogeneity of magnet assemblies for mobile NMR.* 2021. arXiv: `2103.13691 [physics.app-ph]`. URL: `https://arxiv.org/abs/2103.13691`.

[16] Gerald R. Lynch and Orin I. Dahl. "Approximations to multiple Coulomb scattering". In: *Nuclear Instruments and Methods in Physics Research Section B: Beam Interactions with Materials and Atoms* 58.1 (1991), pp. 6–10. ISSN: 0168-583X. DOI: `https://doi.org/10.1016/0168-583X(91)95671-Y`. URL: `https://www.sciencedirect.com/science/article/pii/0168583X9195671Y`.

[17] Romain Ravaud and Guy Lemarquand. "Comparison of the coulombian and amperian current models for calculating the magnetic field produced by radially magnetized arc-shaped permanent magnets". In: *Progress in Electromagnetics Research* 95 (July 2009). DOI: `10.2528/PIER09042105`.

[18] Bruno Benedetto Rossi. *High-energy particles.* Prentice-Hall physics series. New York, NY: Prentice-Hall, 1952. URL: `https://cds.cern.ch/record/99081`.

[19] Stephen M. Seltzer and Martin J. Berger. “Improved procedure for calculating the collision stopping power of elements and compounds for electrons and positrons”. In: *The International Journal of Applied Radiation and Isotopes* 35.7 (1984), pp. 665–676. ISSN: 0020-708X. DOI: `https://doi.org/10.1016/0020-708X(84)90113-3`. URL: `https://www.sciencedirect.com/science/article/pii/0020708X84901133`.

[20] Yung-Su Tsai. “Pair production and bremsstrahlung of charged leptons”. In: *Rev. Mod. Phys.* 46 (4 Oct. 1974), pp. 815–851. DOI: `10.1103/RevModPhys.46.815`. URL: `https://link.aps.org/doi/10.1103/RevModPhys.46.815`.

Acknowledgement

With the completion of this thesis, I want to express my gratitude to everyone who played a role in its realization. Firstly, I want to thank Prof. André Schöning for giving me the opportunity of working on this project, making me feel welcomed in his working group and guiding me throughout this journey. Also, I want to show my appreciation to Prof. Ulrich Schmidt, who immediately agreed to be my second examiner. I am especially greatful to my supervisor Tamasi Kar, who wholeheartedly supported me during the entire process and shared her expertise in many discussions at the office. Furthermore, I would like to thank Christoph Sauer, who answered any coding-related questions, Sebastian Dittmeier and Heiko Augustin, who gave in-depth feedback about my work at many stages and were available for any type of question that could also get a bit more technical. In addition to Tamasi, Christoph, Sebastian and Heiko, I want to acknowledge David Fritz and Ruben Kolb, who took the time to proof read my thesis. I enjoyed the motivating environment in the working group and I am thankful to everyone else of the group. Finally, I thank all of my family and friends for the support during my studies.

Erklärung

Ich versichere, dass ich diese Arbeit selbstständig verfasst und keine anderen als die angegebenen Quellen und Hilfsmittel benutzt habe.